

Supersonic Combustion of Solid Fuels

Ethan J. Schlussel, 2d Lt, USAF

Thesis submitted to the Faculty of the
Virginia Polytechnic Institute and State University
in partial fulfillment of the requirements for the degree of

Master of Science
in
Aerospace Engineering

Gregory Young, Chair

Joseph A. Schetz

Luca Massa

November 8, 2023

Blacksburg, Virginia

Keywords: Solid Fuel, High Speed Propulsion, Supersonic Combustion

Supersonic Combustion of Solid Fuels

Ethan J. Schlussel, 2d Lt, USAF

(ABSTRACT)

A direct connect, supersonic solid fuel combustor with a cavity is explored in the context of understanding characteristics related to ignition, regression rate, combustion, and flow fields for application in advancing solid fuel scramjet research. 3D printed, polymethylmethacrylate fuel grains are loaded into both fully enclosed and optically accessible combustors. The ignition characteristics are investigated by systematically varying the internal geometry of the fuel grain to develop a flammability map with respect to non-dimensional geometric parameters. Results reveal that a longer and larger flameholding cavity creates favorable conditions for ignition and sustained combustion. The inlet temperature is also systematically varied to extend the available literature on the supersonic combustion of solid fuels to lower temperature operating conditions and show that a higher inlet temperature is conducive to sustained combustion and higher regression rates. The regression rates of the fuel grains are measured to determine a concentration of regression in the flameholding cavity along the angle of the downstream side of the cavity. Ignition and sustained combustion rely heavily on the fuel in the flameholding cavity. A decreasing regression rate is observed as the fuel regresses by measuring the regression rate at discrete time intervals during a firing of the optical combustor. The optical combustor is also subject to various high-frequency imaging techniques. Shadowgraph imaging shows the changes in density of the flow field and finds a normal shock in the constant area section. CH^* chemiluminescence imaging provides novel observations of the concentrated areas of combustion along the fuel grain wall by highlighting the heat release from combustion. A high intensity of CH^* radicals

is in the upstream section of the flameholding cavity. When considered in the context of the concentration of regression, this indicates that the recirculation zone pulls fuel from the downstream section of the cavity, combusts it in the upstream section of the flameholding cavity, then expels the higher enthalpy gas into the core flow. Additionally, observing the flow provides insight into the flow dynamics of opposing cavities in a supersonic flow field. The symmetry of the flow field is found to be reliant on the stability of the flameholding cavity length to depth ratio.

Supersonic Combustion of Solid Fuels

Ethan J. Schlussel, 2d Lt, USAF

(GENERAL AUDIENCE ABSTRACT)

A solid fuel scramjet has the potential to be the simplest and most cost effective method of achieving hypersonic flight. A liquid fuel scramjet has been demonstrated in free flight, but liquid fuels present many issues involving safety and storage that can be eliminated by introducing solid fuels. Supersonic combustion, or burning fuel in an air flow moving faster than the speed of sound, is a complicated subject due to the irregularity of flow fields and the requirement of combustion to occur at a high rate. The research within this thesis presents many novel technologies that have never been presented in published literature in the context of the supersonic combustion of solid fuels. By conducting ground testing of a solid fuel scramjet, characteristics of the combustion can be studied to expand the available literature in the field to new fuel geometries and inlet conditions. The ignition and sustained combustion of a solid fuel scramjet is extremely reliant on the initial geometry of the fuel and the initial temperature of the flow. This research advances the field of supersonic combustion of solid fuels by developing an optically accessible combustor using quartz windows. These characteristics of supersonic combustion are investigated using high-speed video recording. The results of these techniques provide insight into favorable fuel geometries and inlet conditions. Additionally, patterns observed in the flow field explain concentrations of combustion and fuel consumption.

Dedication

To my friends and family.

Acknowledgments

Thank you to my advisor, Dr. Gregory Young, for guiding me through the research and giving me the opportunity to learn about solid fuels and propulsion. His guidance is never-ending, and always appreciated. Thank you Dr. Joe Schetz and Dr. Luca Massa for their additional support and discussion that shaped the direction of this research. The bi-weekly solid fuel scramjet group meetings with my committee and research colleagues have given insightful feedback every step of the way. I am appreciative of the questions and discussion provided by many research colleagues and friends. Thank you to the SFSJ research group and PropEL research group who have donated their time in helping me experiment and analyze data. I was able to conduct this research due to the Air Force Institute of Technology Graduate Scholars Program. Thank you to the small cohort of Air Force Officers living in Blacksburg who have helped me have some connection to the Air Force despite our geographical separation from the nearest Air Force base. The research conducted in this thesis is possible due to the support of the Office of Naval Research and Program Officer Dr. Eric Marineau under Grant No. N00014-21-1-2299. Additional support came from the staff and facility at the Virginia Tech Advanced Propulsion and Power Laboratory.

Contents

List of Figures	x
List of Tables	xv
1 Introduction	1
1.1 Air-Breathing Propulsion	1
1.2 Solid Fuels	6
1.2.1 Solid vs Liquid Fuels	7
1.3 Research Motivation and Scope	9
2 Review of Literature	10
2.1 Solid Fuel Combustion	10
2.2 Flameholding and Supersonic Combustion	15
2.3 Solid Fuel Ramjet	17
2.4 Solid Fuel Scramjet	20
3 Methods and Experimental Apparatus	25
3.1 Experimental Facility	25
3.1.1 Combustor Design	27

3.1.2	Controls and Data Acquisition	28
3.2	Fuel Grain Sample Preparation	30
3.3	Experimental Procedures	33
4	Enclosed, Rectangular Cross-section SFSJ Experiments	34
4.1	Experimental Procedure and Data Collection	34
4.2	Results	39
4.2.1	Varying Geometry Experiment	39
4.2.2	Varying Temperature Experiments	50
5	Optically Accessible SFSJ Experiments	54
5.1	Experimental Procedure and Data Collection	54
5.2	Results	57
5.2.1	Ignition Experiments	57
6	Conclusions	73
	Bibliography	76
A	Uncertainty Analysis	87
B	Matlab Codes	89
B.1	Edge Detecting Codes for Enclosed, Rectangular Cross-Section SFSJ	89

B.1.1	Fuel Grain Length Edge Detection	89
B.1.2	Constant Area Section Edge Detection	96
B.2	Regression Rate Code for Optically Accessible SFSJ	106

List of Figures

1.1	Performance of hydrogen fueled aircraft propulsion at varying Mach number [1].	2
1.2	Two dimensional schematics of ram compression propulsion devices detailing different components of the combustion process [2]. The top schematic depicts a ramjet, the bottom schematic depicts a scramjet.	3
1.3	Two dimensional schematic of a turbo ramjet combined cycle [1].	6
2.1	Adding a downstream angle to reduce pressure oscillations [3].	16
2.2	Flow field for a traditional SFRJ [4].	18
2.3	SFSJ fuel grain cross-section as used by Angus [5].	21
2.4	SFSJ fuel grain cross-section as used by Ben-Yakar et al. [6].	22
3.1	Full SFSJ system schematic at APPL.	26
3.2	Cross-section of the SFSJ combustor at APPL. The pressure ports are numbered 1-7.	27
3.3	25.4mm wide combustor with no optical access (left). 50.8mm wide combustor with optical access (right). Many of the key components are labeled, and are the same between both configurations.	29

3.4	3D printing fuel grains in preparation for experiments. PMMA fuel grain prints on a Raise 3D Pro2 Plus 3D printer for the 50.8mm wide optical combustor (left). A series of completed fuel grains for the 50.8mm wide optical combustor (top right). A 25.4mm wide enclosed fuel grain printed without one wall to show the internal geometry (middle right). The top of a 25.4mm enclosed fuel grain with pressure ports spaced at 38.1mm, and threaded inserts for mounting the fuel grain to the combustor body (bottom right).	31
3.5	Aluminized HTPB-AP propellant curing in 3D printed molds. The propellant cures overnight and settles to be about 5mm thick (left). The propellant strips are secured to the top and bottom of the flameholding cavity with two-part epoxy (right).	32
4.1	Schematic showing the geometric dimensions which can be varied in a SFSJ.	36
4.2	Flammability map from the enclosed, rectangular cross-section SFSJ. The dashed line shows the estimated flammability limit based on geometry.	37
4.3	The process for cutting and analyzing the enclosed fuel grain for time-averaged regression analysis. The fuel grain is cut with a bandsaw along the cutting plane (top left) to produce two halves of a fuel grain (top right). The surface is painted black, and the edges are highlighted with white paint to increase contrast (bottom left). MATLAB's Image Processing Toolbox returns the fuel grain edge (bottom right).	38
4.4	Representative image taken in the direction of the flow to measure the regression in the constant area section of the enclosed fuel grain.	39

4.5	An exhaust plume from an enclosed SFSJ firing showing the shock diamonds. Flow from left to right.	40
4.6	Wall pressure measurements of a typical enclosed fuel grain SFSJ combustion experiment, test 16. The numerical labels correspond to the pressure ports labeled on Fig. 3.2. Pressure-time measurements (left) and pressure-distance measurements (right) are plotted.	41
4.7	Wall pressure measurements from test 19, demonstrating the effects of a larger H_{const} on the pressure during combustion. The numerical labels correspond to the pressure ports labeled on Fig. 3.2. Pressure-time measurements (left) and pressure-distance measurements (right) are plotted.	43
4.8	Representative plot showing pre- and post-fired fuel grains, as well as time- averaged regression rate, test 1.	44
4.9	Representative plots showing average regression rate of the bottom of select fuel grains.	45
4.10	Representative plots showing time-averaged regression in the constant area section for selected tests.	46
4.11	Average constant area section wall regression rates plotted with respect to geometric parameters.	48
4.12	Cut and 3D scanned fuel grain, flow from left to right, test 1 (top) and test 10 with larger initial H_{const} (bottom).	49

4.13	Time-averaged constant area section regression rates plotted with respect to varying temperature of air (left). Time-averaged top/bottom regression rates across the length of the fuel grain compared to a regression rate correlation from Cohen-Zur & Natan [7] (right).	51
4.14	Regression profiles and regression rates of varying fuel grain experiments, tests 1-4.	53
5.1	Schematic of shadowgraph setup.	55
5.2	Typical Scanivalve pressure measurements for optical SFSJ. Fuel grain geometry A, test 1 (left). Fuel grain geometry B, test 2 (right).	58
5.3	Combusting samples of the optical SFSJ, demonstrating a biasing phenomena. Flow from left to right. Symmetric core flow during optical SFSJ firing of geometry A, test 1 (top). Upward biased core flow during optical SFSJ firing of geometry B, test 2 (bottom).	59
5.4	Visualization of a vortex attached to the front edge of a cavity that deflects the shear layer into the free stream [8].	59
5.5	Cold flow shadowgraph of multiple fuel grain geometries and flow directly from the C/D nozzle. Flow from left to right.	60
5.6	Flammability map from the optically accessible SFSJ. Due to the limited geometries examined, no flammability limit has been explicitly determined.	62
5.7	Snapshots of high speed video of combustion on geometry A, flow from left to right. Non-uniformed time increments are chosen to show each time the flow bias changes direction, test 15. Scaling is the same for all snapshots.	63

5.8	Snapshots of combusting shadowgraph video on geometry A, flow from left to right, test 13. Scaling is the same for all snapshots.	64
5.9	Snapshots of combusting shadowgraph video on geometry B, flow from left to right, test 14. Scaling is the same for all snapshots.	65
5.10	Geometry A, test 11 (top), and geometry B, test 17 (bottom) time-averaged CH* chemiluminescence from full length of fuel grain, flow from left to right.	66
5.11	Geometry A, test 15 (top), and geometry B, test 16 (bottom) time-averaged CH* chemiluminescence from flameholding cavity, flow from left to right.	67
5.12	Regression Profiles and time averaged regression rates for fuel grain geometry A, test 3 (top), and geometry B, test 2 (bottom). The error bars represent the experimental uncertainty from data collection methods.	68
5.13	Statistically averaged regression rates for geometry A.	70
5.14	Statistically averaged regression rates for geometry B.	70
5.15	Summarized process of combusting fuel in a SFSJ with a small L/D flameholding cavity.	71
5.16	Summarized process of combusting fuel in a SFSJ with a large L/D flameholding cavity.	72

List of Tables

4.1	Tested Enclosed Fuel Grain Geometries	35
4.2	Comparison of Varying Test Duration	48
4.3	Tested Enclosed Fuel Grain Varying Temperature	50
5.1	Tested Optical Fuel Grain Geometries	56

List of Abbreviations

α	Angle of the converging slope from the flameholding cavity to the constant area section
ΔH	Effective heat of gasification
\dot{m}	Mass flow rate
\dot{Q}	Heat flux
\dot{r}	Regression rate
ρ	Density
a	Empirical constant
A_{const}	Cross-sectional area of the constant area section in a solid fuel scramjet fuel grain
A_{fh}	Cross-sectional area of the flameholding cavity in a solid fuel scramjet fuel grain
A_{in}	Cross-sectional area of the inlet to the flameholding cavity in a solid fuel scramjet fuel grain
AP	Ammonium Perchlorate
CL	Chemiluminescence
d_{cyl}	Diameter of the cylindrical (constant area) section in an axisymmetric solid fuel scramjet fuel grain
d_{fh}	Diameter of the flameholding cavity in an axisymmetric solid fuel scramjet fuel grain

d_{in}	Diameter of the inlet to the flameholding cavity in an axisymmetric solid fuel scramjet fuel grain
G	Mass flux
H_{const}	Height of the constant area section in a rectangular cross-section solid fuel scramjet fuel grain
H_{fh}	Height of the flameholding cavity in a rectangular cross-section solid fuel scramjet fuel grain
H_{in}	Height of the inlet to the flameholding cavity in a rectangular cross-section solid fuel scramjet fuel grain
HTPB	Hydroxyl Terminated Polybutadiene
IDP	Isodecyl pelargonate
L_{const}	Length of the constant area section in a solid fuel scramjet fuel grain
L_{fh}	Length of the flameholding cavity in a solid fuel scramjet fuel grain
MDI	Methylene dyphenyl diisocyanate
P	Pressure
PMMA	Polymethyl-Methacrylate
SFRJ	Solid Fuel Ramjet
SFSJ	Solid Fuel Scramjet
T	Temperature
TMD	Theoretical maximum density

Chapter 1

Introduction

1.1 Air-Breathing Propulsion

An air-breathing engine is a method of air vehicle propulsion in which atmospheric air is used as the working fluid in a thermodynamic system to produce thrust. This is done through a process based on the Brayton Cycle, in which air is compressed then heated to increase the enthalpy. The high enthalpy flow is expanded to expel the air at a higher velocity [9, 10]. This process varies from rocket propulsion in that the oxidizer is gathered from the atmosphere, rather than being carried on-board the aircraft. By utilizing the atmospheric air, the system can be made lighter and more efficient.

The invention of air-breathing propulsion for aircraft led to radically extended possibilities on the limits of aircraft speed and efficiency. The first air-breathing propulsion engine is the turbojet, a type of gas turbine engine that uses a compressor and a turbine to generate thrust. Although investigated mathematically and theoretically as early as the 18th century, the gas turbine engine was created simultaneously in the 1930s by Sir Frank Whittle in the United Kingdom and Dr. Hans von Ohain in Germany. Although turbojets are common today, their work revolutionized the landscape of flight propulsion [11]. By 1935, the idea of high speed and supersonic propulsion prompted the topic of the fifth Volta conference in Italy. This conference is often marked as the beginning of the supersonic age. In 1937, Whittle with diesel oil as fuel, and von Ohain with hydrogen, each separately powered the

first tested turbojets [12].

The turbojet uses the basics of the Brayton Cycle for a low compression, continuous flow thermodynamic process. Since then, various versions of the gas turbine engine have been developed as the basis for modern turboprops, turbofans, and turbojets. Each of these methods provides different operational altitudes and air speeds, with a maximum operating envelope at around Mach 3 as in Fig. 1.1[1, 13]. Generally, each of these engines intake air into a compressor, burn liquid fuel in the compressed air, then use the high enthalpy product to power a turbine. Turbine based air-breathing propulsion has many applications from high-speed military aircraft, from the afterburning turbofan engines on military jets, to turboprops on small commercially available and privately owned aircraft.

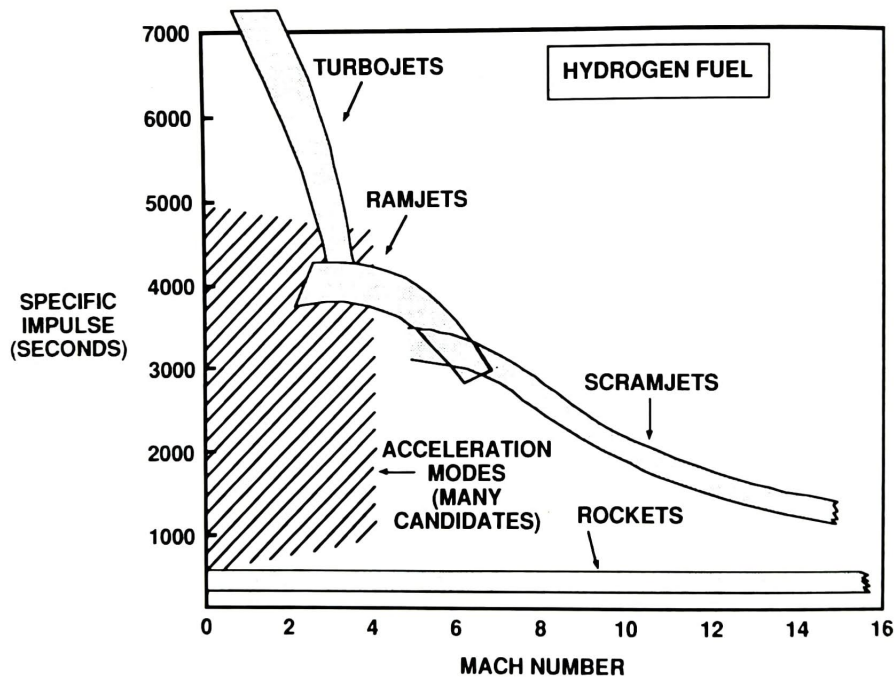


Figure 1.1: Performance of hydrogen fueled aircraft propulsion at varying Mach number [1].

Higher flight speeds, particularly greater than Mach 3, greatly challenge the effectiveness of using turbine propulsion. At these upper limits of turbine-based propulsion, the air entering

the compressor must be slowed so much that the effects of the compressor and turbine make the process less efficient at generating thrust. Removing the turbomachinery creates a simple process by which air enters through a diffuser, generating high pressure, subsonic air. Fuel is then injected and combusted in the flow, increasing its enthalpy before being re-accelerated through a nozzle to generate thrust [2, 13]. This process, depicted in Fig. 1.2, is called ram compression, and is the namesake for the ramjet [9].

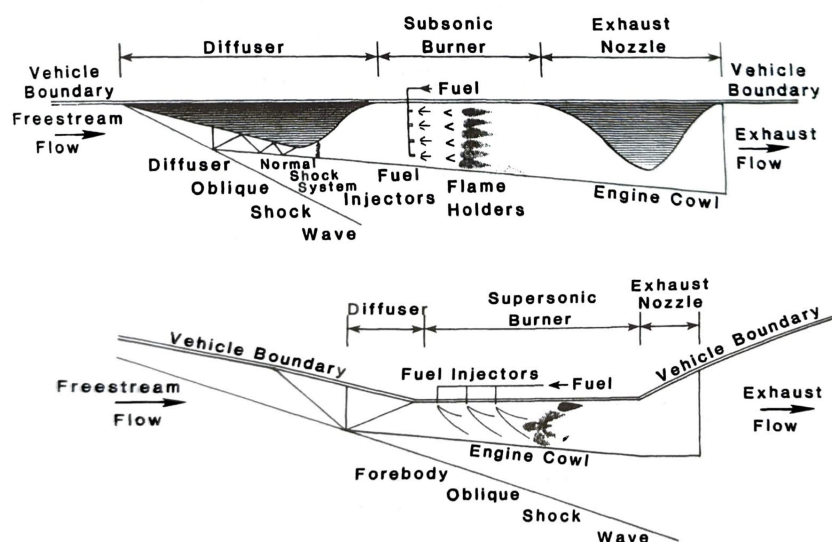


Figure 1.2: Two dimensional schematics of ram compression propulsion devices detailing different components of the combustion process [2]. The top schematic depicts a ramjet, the bottom schematic depicts a scramjet.

The ramjet concept was first realized by Rene Lorin in France in 1913. However, by only considering subsonic speeds, he determined that the ramjet would have a non-viable thermal efficiency. The earliest patent recognizable as a modern ramjet was made in 1928 by Albert Fono in Budapest. It was not until 1935 that another Frenchman, Rene Leduc, ground tested a small ramjet engine at supersonic speeds, catching the attention of other nations during World War II [14, 15]. His work was delayed because of Germany's invasion of France, but his ideas prompted other nations to begin their own ramjet research programs. The United States eventually demonstrated a heptane burning, 6-inch diameter model ramjet in flight

during the Bumblebee flight program in 1945. Then, in 1947, an 18-inch diameter model burning kerosene increased flight velocity to greater than Mach 2 and clearly demonstrated the vast potential of ram compression propulsion. Shortly after World War II, Leduc resumed his work and completed the construction of an airplane using his ramjet called the Leduc-010. It was successfully tested in 1949 as the first manned flight powered by a ramjet [15, 16]. Additional experimental flight testing in the 1950s and 1960s led to the development of ramjet powered, anti-aircraft missiles such as the United States Air Force's Bomarc and the Royal Air Force Bloodhound [16].

As conveyed through Fig. 1.1, the ramjet is limited to speeds less than about Mach 6. Decreasing efficiency and extremely high temperatures in the combustor limit chemical reactions and create high thermal stresses on the aircraft's structure [9]. The supersonic combustion ramjet, or scramjet, maintains supersonic air flow through the combustor to prevent extremely high temperatures while providing high speed thrust. Fig. 1.2 displays the process of combustion for a scramjet differing from a ramjet primarily in the effect of the diffuser on the flow. The scramjet diffuser does not decelerate the flow to subsonic speeds, and therefore only requires a diverging exit nozzle. Of course, supersonic combustion comes with its own set of challenges, such as a shorter residence time for mixing and combustion. Richard J. Weber and John B. MacKay, researchers at the Lewis Flight Propulsion Laboratory, published a theoretical analysis of a scramjet in 1958. They determined that supersonic combustion would extend the flight speed capabilities to unknown limits while reducing the effect of internal heating. Specifically, they also noted that the scramjet becomes more efficient than the ramjet above Mach 7, but, with optimal inlet designs, could overtake the ramjet efficiency at flight speeds as low as Mach 5 [17]. Later that same year, Fred Billig and G. L. Dugger at Johns Hopkins University's Applied Physics Laboratory built and ground tested a small scramjet model which sustained combustion in a Mach 5 flow. [18].

Antonio Ferri significantly contributed to the understanding of supersonic combustion in investigations through the 1960s [17].

Following the direct connect ground testing in the 1960s, NASA began the Hypersonic Research Engine program. This program investigated many critical technologies of supersonic flow, including inlet nozzle design, subsonic and supersonic combustion, and boundary layer transitions [17]. Despite decades of research in the program, and continuous political pressures to achieve scramjet flight, the program was riddled with funding issues. Limited funding, coupled with unwarranted overconfidence of the understanding of supersonic combustion, caused nearly a half a century of research before the first successful scramjet flight demonstration. In 2004, NASA's X-43a launched from the bottom of a B-52 Stratofortress to become the first free flight of a scramjet, achieving velocities of Mach 10 [18].

Ram compression propulsion methods work great in supersonic applications, but they cannot produce thrust unless air is already flowing through the engine. It is also limited in its capabilities at sub-sonic flight conditions where compressibility effects do not create the required pressures within the combustor. Since the ramjet cannot produce static thrust, the practical uses of a ram compression must be launched from moving vehicles, like the Leduc-010 being lifted by Languedoc aircraft [17] or have a first stage of a rocket motor, like the X-43 being dropped from a B-52B and accelerated with a first stage Pegasus Rocket [18]. Alternatively, aircraft like the SR-71 Blackbird utilize combined cycles similar to Fig. 1.3, where an aircraft actuates its inlet from a turbine engine to a ramjet engine at supersonic flight regimes [19].

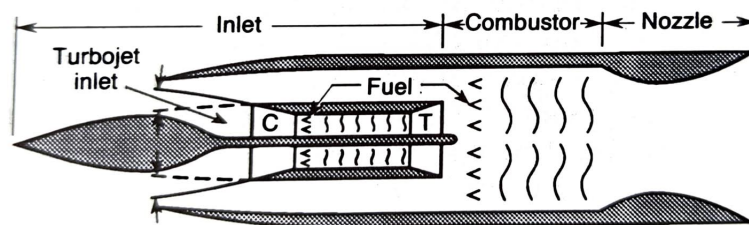


Figure 1.3: Two dimensional schematic of a turbo ramjet combined cycle [1].

1.2 Solid Fuels

Solid fuels are not commonly used for air-breathing aircraft propulsion. Most of the practical flights of ramjets and all of scramjets have used primarily liquid or gaseous fuels [20]. Rockets, however, have used solid propellants for nearly 2000 years stemming from Chinese alchemists studying a mixture of saltpeter, sulfur, and charcoal to promote longevity, and even immortality. Despite their hopes of immortality, they discovered they could ignite the mixture packed into a bamboo cane, resulting in a loud bang known as fireworks [21]. In this mixture, the charcoal and sulfur act as fuels, and the saltpeter acts as an oxidizer [22]. The primary qualifier for rocket propulsion is for the vehicle to carry both the oxidizer and fuel. The fuel is a material that expels energy when it is combusted in the presence of an oxidizer.

Solid rockets developed thousands of years ago, but in the 1930s, there was concern for the potential dangers of solid rockets due to their explosive hazard. In 1933, Sergei P. Korolev and Mikhail K. Tikhonravov separated gelled gasoline fuel and the liquid oxygen oxidizer to create the first hybrid rocket [23]. Various additives and new formulations quickly refined the development of hybrid rockets to require a stronger fuel that can withstand the high pressures of chemical propulsion. This led to the development of Hydroxyl Terminated Polybutadiene (HTPB) in 1961 by Aerojet. HTPB still stands today as widely used and investigated cast fuel, with applications in solid rockets, hybrid rockets, and solid fuel air breathing propulsion

[21]. More details on how a solid fuel is used to create thrust is discussed in Chapter 2.1.

The concept of a solid fuel ramjet (SFRJ) was examined by H. Bartel and W. Rannie in 1946, and further developed by Holzman in 1962, by using atmospheric air instead of a stored liquid or gaseous oxidizer [23]. Compared to the majority of research of liquid and gaseous fueled ramjets, the SFRJ presented an opportunity for a simple and energy dense source of thrust. Most of the limited published studies all investigate SFRJ properties in direct connected testing systems [24]. Despite these attractive qualities, pure SFRJs have seen limited practical application until recently. A modern implementation of a SFRJ has manifested through the United States' partnership with Norway in developing the Tactical High-speed Offensive Ramjet for Extended Range (THOR-ER) [25].

The solid fuel scramjet (SFSJ) has significantly less available research. It was first demonstrated by Witt et al. in 1989 at the Naval Postgraduate School, though ignition was only achieved by burning hydrogen directly into the flow [26]. Investigations at the Technion in Israel by Ben Yakar et al. eventually achieved a self-igniting and sustaining SFSJ [6]. More information on pertinent SFRJ and SFSJ investigations and the mechanisms explaining how they work are discussed in Chapters 2.3 and 2.4.

1.2.1 Solid vs Liquid Fuels

There are many reasons to choose both liquid and solid fuels in various applications. The advantages and disadvantages are shared between fuels in air-breathing and hybrid rocket systems, and solid versus liquid propellants in rocket systems. The fundamental differences are:

1. Safety: Solid fuels are generally inert while in storage. In fact, one of the most researched solid fuels, polymethyl methacrylate (PMMA), is more commonly known as

acrylic or plexiglas and has many non-combustion related applications. This allows many solid fuels to be safely stored and transported without any specialized equipment or regulations, compared to liquid fuels which require specific treatment and storage containers to prevent unintended combustion [23, 27].

2. **Throttleability:** Solid fuels are not capable of being throttled as simply as liquid or gaseous fuels. Once the solid fuel is burning, its energy output is entirely dependent on the properties of the designed system, and it will not shut off until the fuel is fully consumed or the source of the oxidizer is removed. There are some methods of varying the oxidizer supply by changing the amount of air entering the combustor with air-division valves, but this makes the system more complicated, when its simplicity is one of its attractive attributes [28, 29]. Liquid fuels are easily throttled by using valves which control the flow rate of the fuel to the combustion chamber. This makes solid fuel systems more applicable in single use scenarios where refueling and speed control is not necessary [23, 27].
3. **Simplicity:** Systems which utilize solid fuels do not require the extensive plumbing and complexity required for effective use of liquid fuels. Particularly with air breathing solid fuel systems, there is no plumbing required to generate thrust. Compared to liquid fuels, which require tanks, pumps, valves, and pipes, this greatly reduces the cost and timeline required to build a system which burns solid fuels [23, 27].
4. **Efficiency and Thrust:** Solid fuel systems generally produce lower thrust at reduced efficiency. There are many potential explanations for the reduced efficiency. The primary reason results from low-regression rates of solid fuels requiring more fuel surface area to achieve the same thrust produced by a liquid or gas powered system. Additionally, the effects of incomplete heating can cause significant amounts of solid fuel to be stripped and ejected from an engine before it is combusted [23, 27]

1.3 Research Motivation and Scope

The SFSJ has the potential to be a cost effective and simple means of achieving sustained hypersonic flight, but it is still rarely seen in published literature. Compared to ramjets and solid fuel ramjets, the supersonic combustion in a scramjet maintains relatively low static temperatures and pressures while being capable of achieving higher flight speeds [9].

This research focuses on developing a two-dimensional, optically accessible, solid fuel scramjet to allow direct observations of the combustling flow field. To do this, a rectangular cross-section, but fully enclosed, SFSJ is examined and compared to previous literature of axisymmetric SFSJ combustors. This combustor determines the differences which occur from using a rectangular cross-section that could pose as a variance from accepted correlations and results. The rectangular cross-section SFSJ is investigated in the context of a varying fuel grain geometry, as well as inlet conditions. A second combustor is used to create a two-dimensional, optically accessible flow field. Two sides of the fuel grain have quartz windows which create an environment suitable for analysis with imaging techniques such as shadowgraph and chemiluminescence. These imaging techniques are suitable for collecting previously unknown information describing the combustion and consumption of a solid fuel in a supersonic flow.

Chapter 2

Review of Literature

This chapter details research and literature on previous discoveries which guide current studies in the topics of supersonic solid fuel combustion and solid fuel air breathing propulsion. It ranges from fundamental solid fuel pyrolysis studies to the most recent developments that characterize modern understanding of using solid fuels in propulsion.

2.1 Solid Fuel Combustion

There is currently limited practical applications of purely air-breathing, solid fuel propulsion systems, such as ramjets and scramjets. However, the high-speed combustion of solid fuels has been studied since the early development of hybrid rocket systems in the 1930s [30]. Most of the available modern literature on solid fuel combustion is for applications in hybrid rocket systems using hydroxy-terminated polybutadiene (HTPB), paraffin wax, and polymethylmethacrylate (PMMA), with various particle additives and modifications.

PMMA $[(C_5O_2H_8)_n]$ is a commonly used polymer for solid fuel combustion in high-speed propulsion applications. It has a low temperature of decomposition and a relatively high heat of combustion which is favorable for ignition and sustained combustion. It has a higher glass transition point compared to other commonly investigated solid fuels, like HTPB, which makes it stronger but also makes it more brittle [31, 32]. PMMA is also naturally transparent when cast and machined, which has led to it being used for partially optical investigations of

combustion processes in hybrid rockets without sacrificing the standard center-perforated, axisymmetric, fuel grain design [33]. It can also be extruded into a filament suitable for 3D printing; however, this causes it to lose its transparency preventing optically accessible investigations through the fuel grain [34, 35]. Commercially available PMMA is found to have some variability, which could result in some experimental inconsistencies [32].

Polymeric solid fuels used in propulsion applications are consumed in combustion by pyrolysis, or a phase change directly from solid to gas by polymer chain breaking and reorganization. Lengelle [36] summarizes the process as “depolymerization initiated at chain ends, at random points along the chain, or at isolated ‘weak-links.’” The specific mechanism is not consistent in terms of initiation and magnitude between different polymers, but the process remains broadly the same. Most polymers degrade at randomized splits of Carbon-Carbon bonds within the chain and yield various molecular fragments. Depolymerization of PMMA creates free radicals which create an “unzipping” effect, continuing to propagate until the free radicals are stabilized. Typically it is stabilized by the heat transfer from the air to the polymer surface going below the required minimum threshold for pyrolysis. PMMA unzips in a stepwise manner to yield almost entirely complete monomers [37].

The pyrolysis of PMMA contributes to the most important parameter in characterizing solid fuel propulsion motors: regression rate. The regression rate is measured as a velocity to describe the rate at which the solid fuel is converted into gas to undergo a combustion reaction [23]. In 1963, Houser conducted experiments investigating the instantaneous regression rates of axisymmetric hybrid rocket systems [38]. They primarily burned Plexiglas (PMMA), but also investigated polystyrene, polyethylene, and additive mixtures with aluminum, titanium hydride, and carbon. The fuel grains were burned for incrementally specific durations. Then, the fuel grains were weighed to measure the fuel loss to determine the time-averaged regression rate over varying durations of combustion. They explain through this study

that the regression rate of a polymer in a high-speed flow relies on many factors beyond oxidative degradation and pyrolysis of the fuel. For example, depending on the material, fuel can be blown off the surface as polymers soften in higher temperatures. They note that this is unlikely for the PMMA but it is more significant for polymers that soften at lower temperatures, like polystyrene. Finally, they found that regression rate initially starts high, then decreases until achieving a relatively constant rate at about half of the initial rate [38].

Marxman and Gilbert [39] theorized the effects of the heated flow over a fuel grain surface in hybrid rocket combustion and compared the theoretical analysis from their investigation to the data from Houser [38]. By assuming the combustion process occurs entirely within a turbulent boundary layer, two factors are determined for a regression rate equation: the position of the flame in a boundary layer and the effective heat of gasification. They assume the combustion reactions are within a ‘flame sheet’ of negligible thickness at a distance well above the fuel surface and greater than the laminar sublayer. This allows the fuel concentration profiles, and therefore the heat transferred to the surface, to be related to linear functions of the velocity profile above the ‘flame sheet’. The heat of gasification is the energy required for the solid fuel to decompose into a gas phase. This process first consists of the solid polymer decomposing to a liquid monomer + the heat of decomposition, then immediately the liquid monomer decomposes to a gaseous monomer + the heat of vaporization. Each of these steps requires additional energy from the heated flow and changes depending on the specific polymer used. These two concepts provide a basic understanding that the regression rate is proportional to the heat flux, defined as the heat transfer per unit area to the fuel surface (\dot{Q}_w) over the density of the fuel (ρ_f) and the effective heat of gasification (ΔH) in Eqn. 2.1:

$$\dot{r} \propto \frac{\dot{Q}_w}{\rho_f \Delta H} \quad (2.1)$$

Further, they determine the regression rate of a solid fuel with a heated cross flow, which shows that the regression rate is also directly proportional to the mass flux of oxidizer (G) with additional contributions from other parameters, such as the blowing coefficient (mass addition at the wall) and the blowing friction coefficient. Effectively, the regression rate is controlled primarily by the rate of heat delivered to the surface from the turbulent boundary layer provided by the mass flux of oxidizer and not necessarily the surface reaction rate of the solid fuel [39].

The following year, Marxman et al. [40] experimentally investigated their theories using a PMMA slab burner and tube burner with propane spark igniters. Above a lower limit regression rate, they matched the earlier theoretical estimates within 10%. Below that rate, they were finding similar issues to the previous experiments by Houser with fuel material blowing off the surface as it softens [40]. This lower limit of regression rate is determined to be a result of very low mass fluxes causing low convective heat-transfer to the fuel surface. Instead of pyrolysis, the fuel melts and is ejected out of the exit of the combustor, and it does not contribute to the combustion reaction. Alternatively, an upper limit of high mass flux of oxidizer prevents burning, likely due to the limited residence time of the oxidizer over the fuel surface; however, this concept has not been heavily experimented [23].

Studies of how solid fuel is consumed are also conducted using small scale experimental apparatus like counterflow burners [41, 42, 43]. These direct an oxidizer flow to impinge on the surface of a small fuel sample. Small scale experiments allow simple and cost-effective determination of combustion properties and flame characteristics for a solid fuel in a reactive flow, like the flame standoff distance and or flame temperature. They do not necessarily provide accurate data for implementation into complete hybrid rocket or air-breathing propulsion systems [42]. They do, however, allow for direct observation of the instantaneous regression rate of the combusting fuel's surface and improved characterization for solid fuel combustion

simulations [44].

Of particular interest, is the works by Connell et al. and Young et al. [34, 35] who use additive manufacturing to investigate modifications to the geometry and composition of PMMA fuel grains in ground testing for hybrid rockets. They took advantage of 3D printing to easily design and build novel geometries and mixing different additives into the filament. In addition to using unique rifling or swirling geometries for fuel grains that would not have been possible with casting methods, they also determined that 3D printed fuel grains with greater than 90% theoretical maximum density (TMD) achieve equivalent regression rates to the same fuel grains being cast.

Despite over half a century of research in solid fuel combustion, there is still not a definitive and complete expression to define the regression rate for all cases. Realistically, as more effects are considered from flow, fuel, and environmental conditions, there are many different correlations which could be used to determine the regression rate [23]. Generally, the accepted regression rates are primarily related to the mass flux of oxidizer (G_o) raised to an empirical constant (n), and an empirical coefficient (a), and multiplied by any number of additional variables. The backbone of these regression rate equations ties back to the earlier works of Marxman by which the regression rate is proportional to the mass flux of the oxidizer, shown in Eqn. 2.2:

$$\dot{r} = aG_o^n \quad (2.2)$$

Although the mass flux of the fuel does contribute to the total mass flux affecting the regression rate, it is negligible when compared to the mass flux of the oxidizer and is rarely contained within the regression rate equations. Beyond this, the empirical coefficient can be changed by various flow and fuel conditions such as port size and geometry, inlet design, and

oxidizer properties [23]. One simple and effective empirical formula proposed by Muzzy [45] for regression rate in a PMMA hybrid rocket system with negligible radiative heat transfer can be related to the combustor pressure (P_c) and the distance along the fuel grain (x):

$$\dot{r} = aG_o^{0.4}P_c^{0.5}x^{-0.1} \quad (2.3)$$

This demonstrates that as the oxidizer travels further through the fuel grain, the regression rate decreases. However, as previously discussed, this correlation applies to the specific conditions that Muzzy considered. A collection of many different regression rates equations for classical hybrid rockets are summarized in the textbook written by Chiaverini and Kuo [23].

2.2 Flameholding and Supersonic Combustion

The stabilization of a flame in a supersonic combustion process is the key to a sustained reaction that generates thrust. There are different techniques available for flameholding: creating a recirculation zone to mix air and fuel at decreased velocity, introducing a shock wave interaction by injecting fuel perpendicular to the flow, or using turbulence to mix the fuel and oxidizer creating a diffusion flame downstream [3]. Liquid and gas fueled propulsion methods often utilize the shock wave interaction strategy by injecting the fuel normal to the flow. This interaction creates a shock, separating the boundary layer and promoting mixing. To do this, however, requires a delicately, and optimally, designed nozzle to fully evaporate the fuel for combustion in an extremely short residence time [46]. Although the shock creates large pressure losses for a high velocity flow, it is the most simple and direct method of promoting flame holding when injection is required for liquid or gas [3, 8, 47]. The flow

field can be improved by injecting the fuel at an angle, weakening the resulting shock, and allowing for high velocity flow with less pressure losses. However, since the shock is much weaker, the flow must have a much higher enthalpy to auto ignite and stabilize at the desired location [48]. These are productive improvements to the performance of liquid and gas fueled propulsion; however, solid fuels do not have the luxury of injection-based mixing.

The increasing investigation of scramjets and supersonic combustion in the 1990s has turned more studies towards using a recirculation zone to mix the air and injected fuel in a lower velocity region [49, 50, 51, 52]. All these studies have shown that the use of a cavity downstream from the injector improved supersonic combustion efficiency. The same cavity based recirculation concept that was used in liquid fueled combustors was translated for use in the SFSJ by Ben-Yakar et al., and the subsequent investigations conducted of SFSJs [6, 7, 53, 54]. For both the solid and liquid fueled investigations, the cavity is generally shaped to include a backward facing step to separate the shear layer. The shear layer reattaches downstream at the forward facing step, creating a high pressure zone and recirculation as displayed in Fig 2.1 [3].

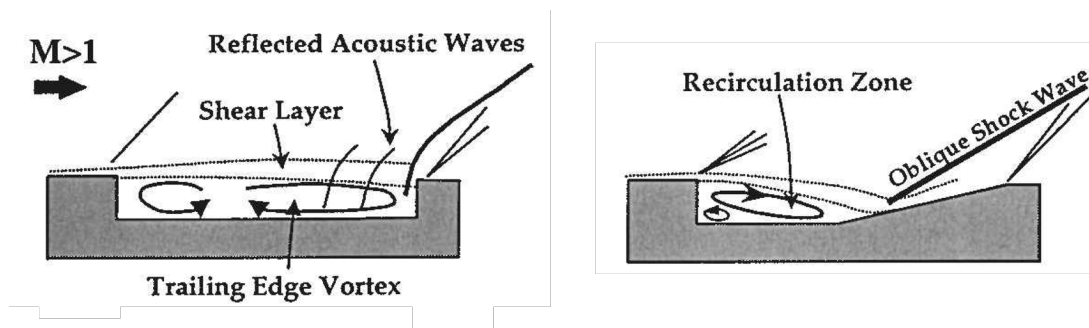


Figure 2.1: Adding a downstream angle to reduce pressure oscillations [3].

The cavities used to create recirculation are also observed to create distinct pressure fluctuations and oscillations depending on the specific geometry and flow conditions presented through a combustor [55, 56, 57, 58], which varies the density and velocity around the cavity

and causes high drag. There are methods that minimize the pressure oscillations and still produce the desired flameholding effect in the cavity, though many of them are impractical in the context of fuel regression of a SFSJ fuel grain [59, 60]. Gruber et al. [61] investigated the effect of varying aft ramp angles in non-reacting supersonic flow and found that, although a shallower ramp angle improves the stability of a flow in the cavity, it also reduces the residence time of the flow in the cavity, which could ultimately negate the benefits of introducing a cavity to the flow.

Recently, chemiluminescent imaging techniques have been used to further analyze supersonic ignition and flameholding in cavities in the context of developing a deeper understanding of scramjets [62, 63, 64, 65]. Kato et al. investigated the flame dynamics of a model scramjet with and without a cavity to determine the effect on flameholding. They explain that the stability of a flame in supersonic combustion increases in stability in the presence of a cavity. However, when the back pressure in the combustion chamber increases enough to choke the flow, and effectively become a ramjet, the cavity behaves like an acoustic source, altering the frequencies within the combustor and diminishing flameholding through extreme fluctuations in the flame [65].

2.3 Solid Fuel Ramjet

The solid fuel ramjet (SFRJ) has been investigated in static testing rigs since the 1970s. It is designed to create a recirculation zone resulting from a rearward facing step to cause separation forming a shear layer. The recirculation zone provides flame stabilization where the pyrolyzed fuel can mix with the air. As more fuel is consumed, the thermal energy from the recirculation zone is transferred down the length of the fuel grain to create thrust [66]. These mechanisms are visualized in Fig. 2.2 [4]. The flow reattaches to the fuel surface some

distance downstream, creating a local maximum heat flux to cause high fuel regression rates.

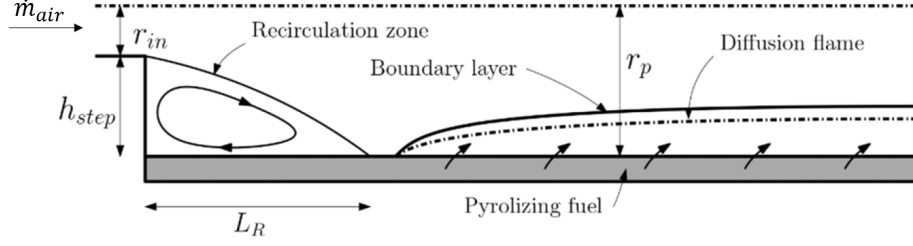


Figure 2.2: Flow field for a traditional SFRJ [4].

The factors which improve flameholding are mostly linked to increasing the residence time of the fuel/air mixture. This can be achieved with active methods, such as swirling the flow upstream of the combustor [67, 68, 69], or through passive methods, such as changing the fuel grain geometry. The geometry of the fuel grain is found to be extremely influential in determining the ignition and burning characteristics of a SFRJ [70]. In particular, the ratio of port diameter to inlet size, also characterized by the size of the rearward facing step, is the most important in providing the recirculation zone for proper flameholding. This ratio is important because most of the combustion occurs in the shear layer of the recirculation zone, though it does not tend to be well mixed [71]. Many different sizes and configurations of SFRJs have been developed for investigating the most optimal conditions for improved mixing and combustion efficiency [72, 73, 74, 75]. In general, these experiments found that a smaller rearward facing step and a smaller overall combustor size led to declining flameholding capability and lower efficiency.

Novel geometries have been investigated in efforts to further improve ignition characteristics and flameholding in SFRJs. Due to the unavailability of continuous fuel slabs which were the length of their two-dimensional windowed combustor, Woolridge and Netzer [76] used two shorter fuel slabs in succession in a SFRJ combustor. This created an uneven joint in the middle of the combustor and was noted to have contributed to improved flameholding after

the initial inlet step exceeded its flammability limits. Gallegos et al. [4] creates favorable geometries for improved flameholding by creating a forward-facing step and forming a cavity. The cavity greatly improves the contrast between the recirculation zone and the core flow through the rest of the combustor and results in enhanced flameholding for high-speed solid fuel combustion [4].

To investigate the combustion process in a more holistic study, Schulte [71] inserted thermocouples and utilized gas-chromatography to obtain temperature profile and species concentration throughout the combustion process. The temperature profile has a maximum near the fuel grain wall in the recirculation zone, then decreases sharply in the core flow. Additionally, the lowest level of oxygen detected was in this same location near the wall, signifying that the combustion process occurs primarily in the recirculation zone near the fuel grain wall, then fuel-rich gas is recirculated into the core flow to react with the air near the inlet. The importance of vortex shedding and recirculation resulting from the rearward facing step was visualized through the development of an optically accessible SFRJ.

A recent investigation uses chemiluminescence to further confirm the earlier discoveries in the topic of how solid fuel combusts in a ramjet. In addition to visualizing the combustion and recirculation previously described, higher mass flow rates of the air are observed to compress the diffusion flame closer to the fuel grain wall, concluding that the ability to change the inlet nozzle geometry would improve the flame stability and heat-release distribution in the combustion chamber [77].

Some work has been done in quantifying the regression rate of SFRJs through empirical correlations. Like the hybrid rocket systems, there are different forms of empirical SFRJ regression rate equations. The generally accepted form of the equation relies on the mass flux of air (G_{air}), the temperature of the inlet air ($T_{2,tot}$), the combustor pressure (P_c), and an empirical constant (a). The complete equation is used as early as 1973 [78], and has been

corroborated by others [70, 73].

$$\dot{r} = aP_c^b G_{air}^c T_{2,tot}^d \quad (2.4)$$

Broadly, this is similar to the hybrid rocket regression rate equations, like Eqn. 2.3, used to describe the combustion rate of hybrid rockets. The difference is the SFRJ relies on the mass flux of atmospheric air, instead of the mass flux of an oxidizer.

2.4 Solid Fuel Scramjet

The solid fuel scramjet (SFSJ) has been investigated in static testing rigs since the 1990s, with most investigations occurring at the Technion – Israel Institute of Technology. The first recorded successful ignition of a SFSJ, however, was by Witt at the Naval Post Graduate School in 1989 [26]. They used a PMMA fuel grain with a cavity upstream of a smooth bore. There was difficulty in ignition with these early experiments. They required a hydrogen pilot flame upstream of the fuel grain and never demonstrated combustion entirely reliant on the solid fuel. The most widely investigated fuel grain shape was determined shortly after by Angus [5], also at the Naval Postgraduate School, when a diverging section was added downstream of the smooth bore constant area section. The geometry used is depicted in Fig. 2.3 [5], consisting of a flameholding cavity for improved recirculation, followed by a constricted section with a constant cross-sectional diameter, then a diverging section through the end of the combustor, preventing choking as the flow re-accelerates. These experiments also required a hydrogen pilot flame to achieve ignition and sustained combustion [5].

Experimental SFSJ research was continued by the Technion. Ben-Yakar [6] outlines the difficulties of sustained solid fuel supersonic combustion:

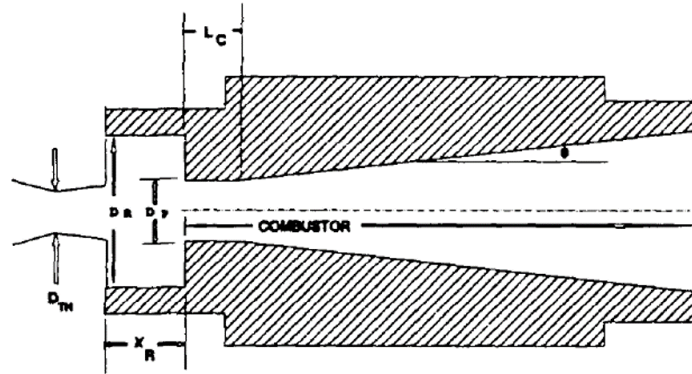


Figure 2.3: SFSJ fuel grain cross-section as used by Angus [5].

1. The fuel-to-air ratio cannot be controlled due to the reliance on fuel regression.
2. Burning primarily at the walls limits combustion efficiency due to incomplete mixing.
3. High flow speeds result in very short residence time in the combustor.
4. Supersonic flameholding is extremely difficult.
5. Internal port geometries change, and could cause undesired effects.

Nonetheless, by varying the geometry established previously to support recirculation as a flame stabilization zone by adding an angled converging section, the sustained self-ignition of a SFSJ using only a vitiated heater upstream of the inlet nozzle was achieved. By varying key parameters of the fuel grain geometry, flameholding limits were established based on non-dimensional geometric parameters describing the fuel grain in Fig. 2.4 [6]. These non-dimensional parameters are the relative size of the flameholding cavity to the inlet size, shown as $d_{fh}L_{fh}/d_{in}^2$, and d_{fh}^2/d_{cyl}^2 , representing the relative step height from the flameholder cavity to the constant area section. The larger each of these parameters is, the greater the capability of a fuel grain for sustained flameholding. These parameters are plotted to create

a flammability map, which can be used to define the lower limits of a sustained combustion in a SFSJ at the specific inlet conditions [6].

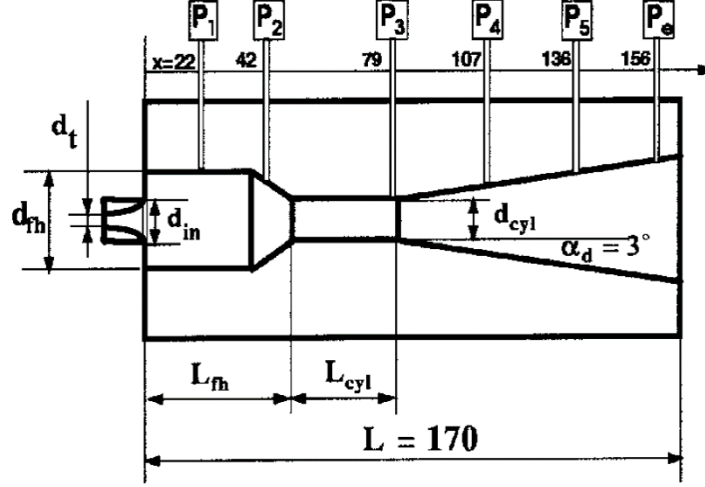


Figure 2.4: SFSJ fuel grain cross-section as used by Ben-Yakar et al. [6].

In addition to developing these important geometric parameters, Ben-Yakar et al. described initial theories explaining the flow fields during the combustion process. Initially, the flow is likely choked in the constricted constant area section downstream of the flameholder. The fuel quickly regresses to cease choking, and the core flow is supersonic throughout. After this point, the flow consists of two patterns: a supersonic core flow in the freestream and partially subsonic recirculation in the flameholding cavity [6].

Cohen-Zur and Natan [7] went further to use these parameters to find an empirical correlation for the spatially averaged instantaneous SFSJ regression rate of PMMA, based on the aforementioned format for the SFRJ regression rate equations. The formula found for regression rate in mm/s at the specific conditions examined is expressed by:

$$\dot{r} = 2.96 * 10^{-6} \dot{m}_{air}^{0.85} T_{t,in} P_{t,in}^{0.2} \quad (2.5)$$

where \dot{m}_{air} is the mass flow rate of air in grams per second, $T_{t,in}$ is the temperature at the inlet of air in Kelvin, and $P_{t,in}$ is the air pressure in atmospheres at the inlet. During the experiments, a difference was also noticed between the initially choked vs initially unchoked conditions depending on the diameter of the constant area section of the fuel grain. The initially choked flow decreases the pressure through the flameholding cavity and the converging section. The decreasing pressure shows signs of a subsonic flow in this constant area section. As the combustion continues, and the fuel regresses, the port area increases to weaken the choke and create fully supersonic flow in the freestream. The initially unchoked fuel grain geometry indicates supersonic flow throughout the entire experiment by the pressure increasing through the flameholding cavity and converging section, with the highest pressure at the narrowest portion of the fuel grain [7].

Every self-igniting and sustained firing of a SFSJ uses a vitiated heater, with the exception of the experiment described by the technical notes from Chernov in 2019 [54]. Instead, they used an arc heater, which provides heated, atmospheric air to the combustion chamber without additional biproducts from combustion in a vitiated heater. Due to the constraints from the arc heater, a rectangular configuration SFSJ was used for three tests. Besides the rectangular cross-section, the geometry mimicked the previously described shapes. The results showed a similar choking phenomenon to the axisymmetric works, but otherwise they provide limited information on the results of the experiment.

Other studies investigate the effect of different fuels and additives in the effectiveness of SFSJ combustion [53, 79]. Additive material studies primarily use HTPB to cast fuel grains with ammonium perchlorate (AP) or aluminum, and they found that higher regression rates in a softer material created a quicker decrease in the relative size of the constant diameter section to the flameholding cavity (d_{fh}^2/d_{cyl}^2). This makes the fuel grain not as effective at supporting sustained combustion after the initial ignition. Although the changing geometry

is a known issue with sustained combustion, this factor was exaggerated more by the softer material.

Computational and numerical studies provide some additional confirmation on the functionality of SFSJs [80, 81, 82, 83, 84]. Many of the more recent numerical studies have been conducted at the Beijing Institute of Technology. Chi et al. [84] investigated the self-ignition characteristics of many geometric parameters and flow conditions on a PMMA fuel grain using finite-rate chemical kinetics. They provide numerical evidence that the flow conditions are limited by oxygen levels and total temperature of the inlet. Additionally, their results match the previous flammability maps which show that a longer and deeper flameholding cavity is beneficial to self-ignition. They also numerically determined the effects of some previously unstudied geometric parameters, such as the angle at the aft end of the flameholding cavity or adding a ‘step type’ flameholding cavity.

The achievements in SFSJs creates many paths forward, outlined by Zhao [85] and Gany [24]. The fuel grain and combustor geometry require significant work in optimization to achieve higher combustion efficiency and reliability. Additionally, longer flameholding methods will be required after the fuel grain has changed geometries beyond the flameholding limits. Generally, many of the specific mechanisms for how the fuel decomposes and combusts is still not well understood. This greatly limits the ability for numerical and computational studies to effectively establish models that can optimize and design SFSJs for lower cost and time.

Chapter 3

Methods and Experimental Apparatus

This chapter explains the methods and procedures used to design, prepare, and fire an experiment with the SFSJ at Virginia Tech’s Advanced Propulsion and Power Laboratory. These experiments investigate and characterize combustion properties of the SFSJ with varying geometric and environmental conditions using novel experimental and data collection techniques.

3.1 Experimental Facility

The Advanced Propulsion and Power Laboratory (APPL) houses the SFSJ and its associated diagnostic and experimental apparatus. The test stand, developed by Gallegos et al. [4], is configurable for testing both solid fuel ramjets and solid fuel scramjets. In the SFSJ configuration, shown in Fig. 3.1, dried air is provided from the APPL compressors at a total pressure of 12.9 atm. The air flow is directed through a TUTCO SureHeat 192 kW electric heater with a maximum output of 650°C (923.15K). The electric heater requires air to flow through it to operate. To allow the heater sufficient time to achieve the desired temperature, the flow is directed through a bypass around the combustor body. Two pneumatic ball valves control whether the flow is directed through the combustor or the bypass. The ball valves separate the electric heater from the combustor body. To reduce the difference in temperature between the pipe leading to the combustor and the core flow, constant wattage heaters are

wrapped around the pipe, resulting in a combustor inlet temperature of approximately 550°C (823.15K), producing nominal flow rates of 245 g/s.

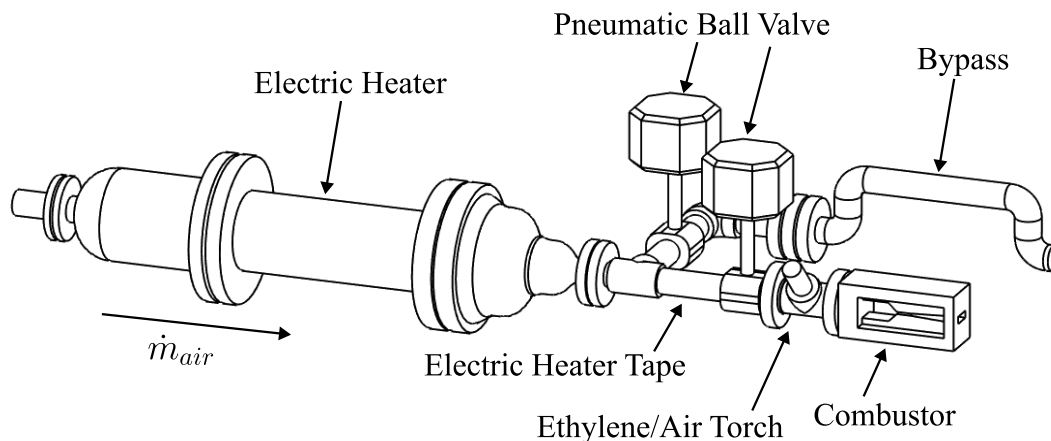


Figure 3.1: Full SFSJ system schematic at APPL.

An optional ethylene and air torch can be affixed to the system immediately upstream of the combustor body to increase the temperature of the flow at the combustor inlet to approximately 950°C (1225K), producing nominal flow rates of 200 g/s. The torch operates at stoichiometric conditions with 1.5 g/s of ethylene and 22.1 g/s of air. By reacting the ethylene at stoichiometric conditions, minimal products of the combustion are present in the core flow into the SFSJ combustor.

To safely fire the SFSJ, a plume containment system is placed immediately downstream of the bypass exhaust and the combustor body exhaust. During an experiment, it continuously sprays water and directs the air flow out the back of the building and towards a containment wall. This ensures that any material that is ejected out of the combustor does not damage any of the nearby facilities.

3.1.1 Combustor Design

There are two SFSJ combustors used for the experiments: a 25.4 mm wide combustor for rectangular cross-section experiments and a 50.8 mm wide combustor for optically accessible experiments. Both have the same design, with the only exception being the width. A cross section of the combustor is shown in Fig. 3.2. The body of the combustor assembly is made from 304 stainless steel, and its dimensions are 304.8 mm in length and 139.7 mm in height, allowing it to hold 266.7 mm long fuel grains. To maintain an airtight seal, the stainless-steel parts are joined together with twenty-eight 316 stainless steel screws and John Crane flexible graphite gaskets.

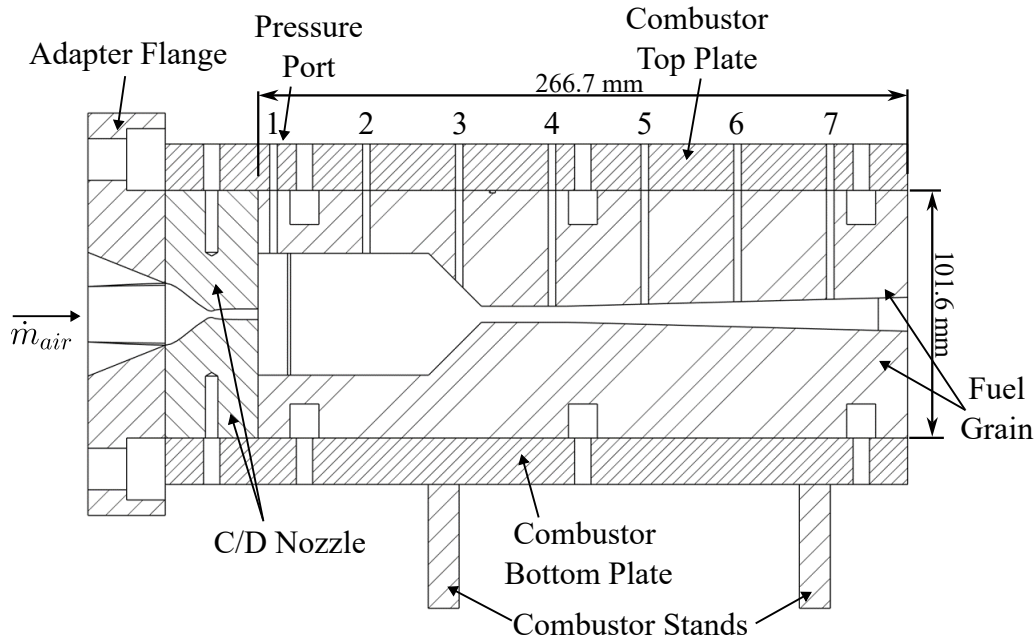


Figure 3.2: Cross-section of the SFSJ combustor at APPL. The pressure ports are numbered 1-7.

Upstream of the combustor, the system air moves in a 2-inch NPT round pipe. To attach the combustor, an adaptor flange at the far left side of Fig. 3.2 converts the flow to rectangular flow. The converging/diverging (C/D) contoured inlet nozzle is attached to the rectangular end of the adaptor flange. The 25.40 mm wide nozzle converges from 25.40 mm x 25.40 mm

to a throat of 25.40 mm x 5.23 mm, then diverges to 25.40 mm x 8.79 mm before the flow is exhausted into the combustor body. The 50.80 mm wide nozzle converges from 50.80 mm x 25.40 mm to a 50.80 mm x 2.62 mm throat, then it diverges to 50.80 mm x 4.39 mm. These two nozzles have identical area ratios of 1.68 to produce a Mach 2.0 flow entering the combustor body. The sides of the combustor are designed to accommodate either quartz windows for optically accessible investigations or steel plates for fully enclosed combustion as depicted on the left in Fig. 3.3. When installed with quartz windows on the right in Fig. 3.3, the window holders open a 222.25 mm x 63.50 mm port for optical analysis of the combustion process. To ensure pressure is maintained within the combustor, and all air travels the full length of the fuel grain, the windows and steel plates are sealed with custom cut, high-temperature, silicone rubber sheet gaskets and O-rings (orange in Fig. 3.3). The top and bottom of the combustor are flat plates. To allow for wall pressure taps, holes are placed in the top plate. Figure 3.2 numbers seven holes on top of the combustor, down the center of the top plate, at 38.10 mm increments to hold Scanivalve 0.63-inch diameter bulged stainless steel tubes for connecting to a pressure scanner. Stainless steel bulged tubules are affixed to the top plate with J-B Weld two-part epoxy to connect the Scanivalve tubes.

3.1.2 Controls and Data Acquisition

The system is controlled via a National Instruments LabVIEW VI. To conduct an experiment, the system initially directs the flow around the combustor and through the bypass while the heater warms up to the required temperatures. After the heater reaches its temperature, the VI firing sequence is initiated to flip the ball valves and direct the air flow through the combustor body. To prevent damage to the system, the firing sequence first opens the combustor ball valve for 1.5 seconds before closing the bypass ball valve. The air then flows through the combustor for the desired amount of time or until the operator

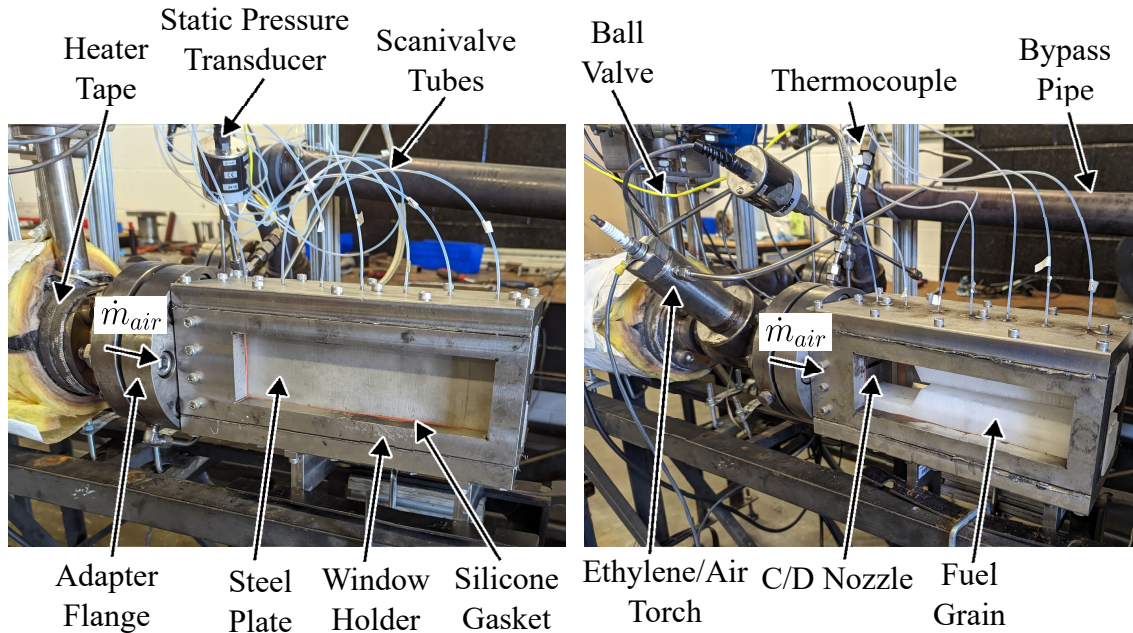


Figure 3.3: 25.4mm wide combustor with no optical access (left). 50.8mm wide combustor with optical access (right). Many of the key components are labeled, and are the same between both configurations.

manually terminates the firing. If the ethylene torch is installed, it is triggered only after the air is already flowing through the combustor body. Upon the completion of a firing, the bypass valve opens for 1.5 seconds before the combustor valve is closed. A nitrogen purge is opened into the combustor to make certain the combustion reaction has completely extinguished.

To determine inlet conditions, pressure is collected immediately upstream of the nozzle using a Setra 206B pressure transducer, and temperature is collected using a type K thermocouple inserted into the flow. Pressure is also collected through the fuel grain at the seven pressure ports on the top plate using a Scanivalve DSA3217-PTP.

Real time video is recorded using a Sony Handycam FDR-AX43A 4K Camcorder. The video output is also connected to a monitor in the control room to allow the operator to have live footage of the firing for observation and enacting emergency protocol. High speed video

is recorded using a Vision Research Phantom VEO 710 high-speed camera coupled with the Phantom Camera Control Software. High speed CH^* chemiluminescence (CL) video is recorded using a Photron FASTCAM SA5 with a Specialised Imaging SIL3 image intensifier and a Nikon PF10545MF-UV ultraviolet lens.

3.2 Fuel Grain Sample Preparation

Fuel grains are designed to a specific geometry using SolidWorks. The models are loaded into the ideaMaker 3D printing slicer software to configure the fuel grains to print at 100% infill and 0.29 mm layer height. The fuel grains are printed one at a time on a Raise 3D Pro2 Plus using PMMA supplied by Push Plastic. To maintain the greatest dimensional accuracy of the cross-section of the completed sample, the fuel grains are printed with the downstream end adhered to the print bed as in the left image in Fig. 3.4. This is because fused deposition modeling 3D printers have the greatest accuracy in the X-Y axis. A large raft is printed as a base layer to reduce the likelihood of failed prints. To improve print quality and consistency, the print surface of the 3D printer is covered with a layer of Kapton tape.

The fuel grains for the fully enclosed experiments, depicted in the bottom right image in Fig. 3.4, are printed as one piece with the top and bottom changing the internal geometry and the sides being flat walls. The top of the fuel grain is printed with seven holes that line up with the pressure ports in the top plate of the combustor body. The sides of the fuel grain are printed to be the same dimensions as the window so the fuel grain fits comfortably inside the combustor body. The fuel grains are 266.7 mm long, and the internal width of these fuel grains is 25.4 mm wide.

For optically accessible combustion experiments, the top and bottom sections of the fuel

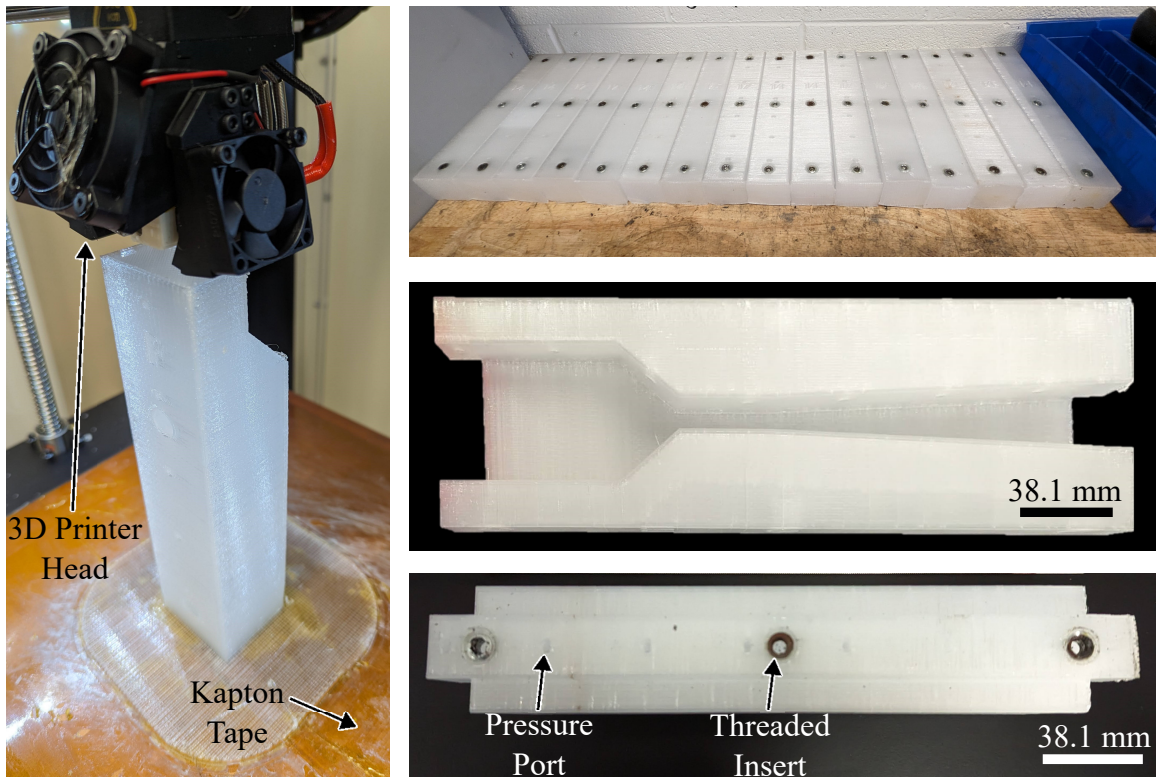


Figure 3.4: 3D printing fuel grains in preparation for experiments. PMMA fuel grain prints on a Raise 3D Pro2 Plus 3D printer for the 50.8mm wide optical combustor (left). A series of completed fuel grains for the 50.8mm wide optical combustor (top right). A 25.4mm wide enclosed fuel grain printed without one wall to show the internal geometry (middle right). The top of a 25.4mm enclosed fuel grain with pressure ports spaced at 38.1mm, and threaded inserts for mounting the fuel grain to the combustor body (bottom right).

grain are printed separately, and no fuel is made for the sides, as shown in the top right image of Fig. 3.4. The top and bottom fuel grains are identical, except for the pressure port holes printed into the top fuel grain. These fuel grains are 50.8 mm wide and 266.7 mm long.

To secure the fuel grains to the combustor body, six $\frac{1}{4}$ - 20 threaded inserts are attached to the top and bottom of the fuel grains using J-B Weld two-part epoxy. The $\frac{1}{4}$ -20 screws, which hold the fuel grains, are outfitted with sealing gasket washers to maintain a pressure seal on the system.

The fully enclosed fuel grain experiments do not use the ethylene torch, therefore they

need an igniter propellant to initiate the combustion reaction. One sheet of propellant is prepared with 2.57g of HTPB from RCS Rocket Motor Components, 16g of 200 micron ammonium perchlorate (AP) and 4g of 90 micron AP powder from Pyro Chemical Source, and 2.7g aluminum powder from VALIMET. This mixture is combined with 1.75g of isodecyl pelargonate (IDP) as a plasticizer and 0.67g of methylene diphenyl diisocyanate (MDI) as a curative, both from RCS Rocket Motor Components. The mixture cures overnight in 3D printed molds to make small sheets shown in Fig. 3.5. To prepare the propellant for an experiment, the 3D printed mold is removed, and the propellant sheet is sliced into strips that are connected to the top and bottom of the fuel grain flameholding cavity using two-part epoxy as seen in the right image in Fig. 3.5. The propellant slices are cut specifically to avoid blocking the pressure port holes and are considered small enough to be fully consumed within the first half second of ignition.

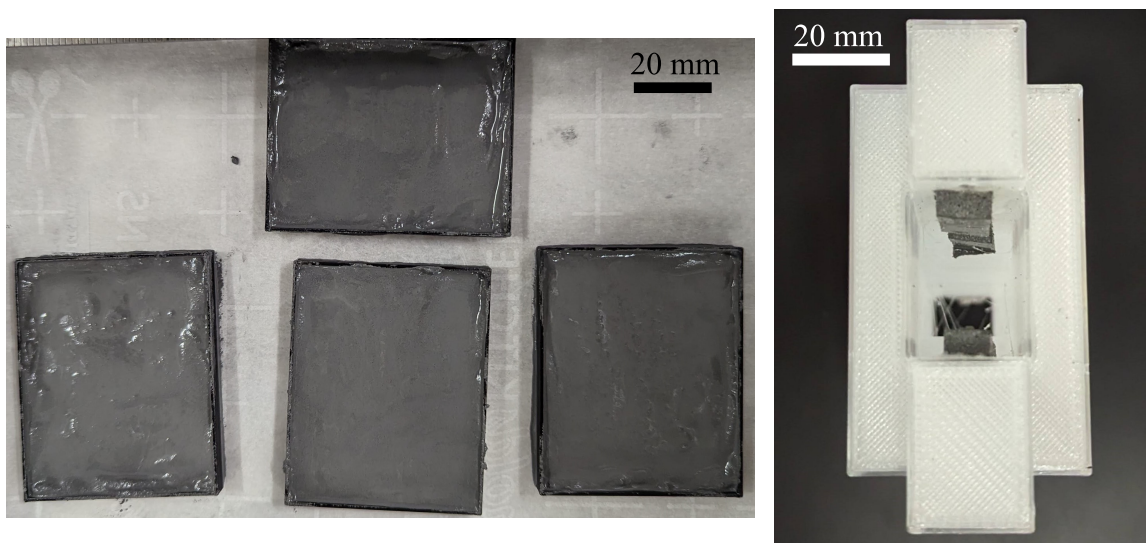


Figure 3.5: Aluminized HTPB-AP propellant curing in 3D printed molds. The propellant cures overnight and settles to be about 5mm thick (left). The propellant strips are secured to the top and bottom of the flameholding cavity with two-part epoxy (right).

3.3 Experimental Procedures

Although the two experiments are conducted on the same system with similar configurations, the enclosed fuel grain and optical fuel grain experiments investigate different properties of SFSJ combustion including regression rate, combustion concentrations, ignition limits, and flow properties. As a result, their specific procedures vary slightly to allow the focus on the data of interest. Each of their specific procedures are laid out in Chapters [4](#) and [5](#).

In general, a single firing consists of running the air through the electric heater until the desired temperature is achieved. This is followed by the toggling of the pneumatic ball valves, which re-direct the air flow through the combustor for no more than 12 seconds. This time limit is placed on firings to prevent potential damage to the facility. Following the firing, the ball valves reset to flow air through the bypass, and a nitrogen purge is flushed through the combustor to ensure all combustion has ceased. The firing is concluded when the heater is shut off and the air supply valve is closed.

Chapter 4

Enclosed, Rectangular Cross-section SFSJ Experiments

This chapter details the rectangular cross-section, fully enclosed, fuel grain experiments. The results from this experiment have been presented at the Thirteenth International Symposium on Special Topics in Chemical Propulsion and at the 2023 American Institute of Aeronautics and Astronautics Aviation conference [86].

4.1 Experimental Procedure and Data Collection

The rectangular cross-section, enclosed SFSJ experiments require the pressure and temperature measurements as well as the real time camera for recording and monitoring of the combustor. Once the fuel grain is secured into the combustor with the igniter propellant attached in the flameholding cavity, the air flow is opened while the electric heater is given time to warm up to the desired temperature. Once the heater achieves the temperature, the firing sequence is initiated which consists of a 5 second delay, then a maximum of 12 seconds of open combustor flow. If sustained combustion is achieved, the operator manually shuts off the air after approximately 5 seconds to prevent damage to the facilities.

Within the rectangular cross-section experiments, both fuel grain geometries and inlet temperature are investigated. For the varying geometry experiments, the heater is set to 650°C

Table 4.1: Tested Enclosed Fuel Grain Geometries

Test # & Geo	T_{in} K	\dot{m}_{air} g/s	H_{fh} mm	L_{fh} mm	H_{const} mm	$\frac{A_{fh}}{A_{const}}$	$\frac{H_{fh}L_{fh}}{A_{in}}$	Sustained Ignition
1 A	806	246	60	70	13.5	4.4	19.6	Yes
2 A	790	248	60	70	13.5	4.4	19.6	Yes
3 A	772	251	60	70	13.5	4.4	19.6	Yes
4 A	754	254	60	70	13.5	4.4	19.6	Yes
5 A	716	261	60	70	13.5	4.4	19.6	No
6 A	822	243	60	70	13.5	4.4	19.6	Yes
7 B	788	249	60	60	13.5	4.4	16.8	Yes
8 C	835	242	60	50	13.5	4.4	14.0	Yes*
9 D	815	245	55	70	13.5	4.1	18.0	Yes
10 E	830	242	60	70	20	3.0	19.6	Yes
11 F	817	244	60	70	16.5	3.6	19.6	Yes
12 G	785	249	50	70	13.5	3.7	16.3	Yes
13 H	829	242	60	45	13.5	4.4	12.6	No
14 I	843	240	60	50	16.5	3.6	14.0	No
15 J	820	244	45	70	13.5	3.3	14.7	Yes
16 K	816	244	45	80	13.5	3.3	16.8	Yes
17 L	814	245	60	70	22.5	2.7	19.6	Yes
18 M	841	241	40	70	13.5	3.0	13.1	No
19 N	822	243	60	70	25.5	2.4	19.6	Yes
20 B	801	247	60	60	13.5	4.4	16.8	Yes
21 F	792	248	60	70	16.5	3.6	19.6	Yes
22 O	812	245	45	80	15.5	2.9	16.8	Yes*
23 P	811	245	37.5	85	15.5	2.4	14.9	Yes*
24 Q	819	244	60	70	29.5	2.0	19.7	No
25 R	815	245	40	90	18	2.2	16.8	No
26 O	818	244	45	80	15.5	2.9	16.8	Yes*
27 P	841	241	37.5	85	15.5	2.4	14.9	Yes*
28 C	831	242	60	50	13.5	4.4	14.0	No

* Showed sustained reignition

For all geometries:

$$L_{const} = 35mm, \alpha = 45^\circ, DivergingAngle = 3^\circ, H_{in} = 8.79mm$$

(923.15 K), producing approximately 550°C (823.15 K) air flow at 245 g/s just upstream of the C/D nozzle. The specific tested geometries, listed in Table 4.1, are varied by three geometric properties based on the non-dimensional geometric parameters used in the flammability map produced by previous research efforts [6, 7]. Since the previous studies used axisym-

metric combustors, their parameters are based on the internal diameter of the fuel grain. The present investigation alters the geometric parameters to be relationships between cross-sectional areas to allow for comparison to previous works. The length of the flameholding cavity (L_{fh}), the height of the flameholding cavity (H_{fh}), and the height of the constant area section (H_{const}) are systematically varied to create a distributed spread on the flammability map of non-dimensional parameters. Specifically for the rectangular cross-section geometry, A_{fh}/A_{const} represents the relative step height from the flameholding cavity to the constant area section, and the relative size of the flameholding cavity is $H_{fh}L_{fh}/A_{in}$ using the dimensions in Fig. 4.1. Tests with repeated geometries are designated by shared letters next to the test number.

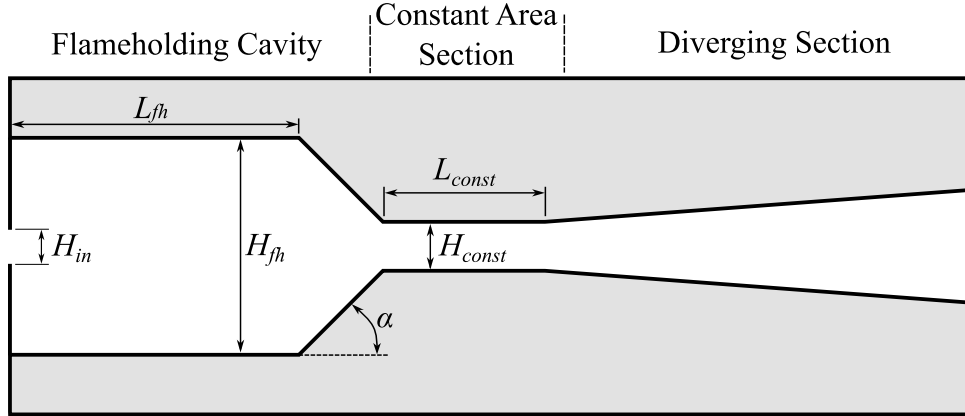


Figure 4.1: Schematic showing the geometric dimensions which can be varied in a SFSJ.

Additional parameters, such as the converging cavity angle (α), the length of the constant area section (L_{const}), the height of the inlet to the combustor (H_{in}), and the diverging section angle are held constant to focus on the variables in the non-dimensional geometric flammability map in Fig. 4.2. This is not to say that they do not affect the ignition characteristics of the fuel grain. They are shown to have some effects in computational investigations [84]. The parameters on the flammability map are used to provide a relevant comparison to previous experimental publications which validate the effectiveness of the

rectangular cross-section combustor [6, 7].

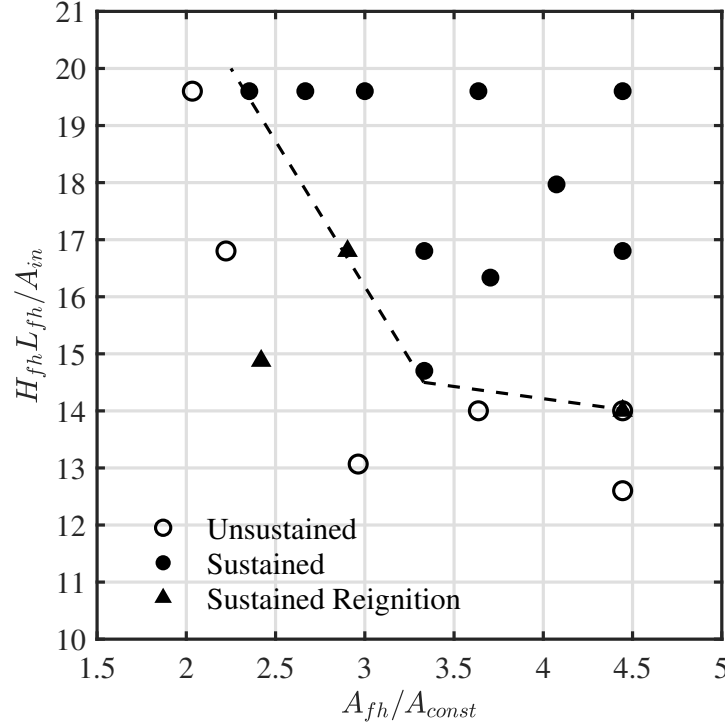


Figure 4.2: Flammability map from the enclosed, rectangular cross-section SFSJ. The dashed line shows the estimated flammability limit based on geometry.

To extract regression rate data, the fuel grains are cut in half using a bandsaw on the vertical plane parallel to the flow. Each half of the fuel grains are spray-painted matte black, then the regressed interior fuel edge is painted white using a paint marker. The paint provides enough contrast to take images of each half of the fuel grain and load them into MATLAB to be analyzed using MATLAB's Image Processing Toolbox. A code is written to detect the edge from the white to the black and provide an accurate profile of the regression. This process is visualized in Fig. 4.3 and the code is printed out in Appendix B.1. A ruler is placed in view of the camera for calibration. Images are also taken of the fuel grain looking in the direction of the air flow by placing spacers the width of the bandsaw blade between the two halves of a fuel grain. The images could not be accurately taken before cutting the fuel grain in half, because the black paint adds contrast to the image in Fig. 4.4. A light illuminates

the white surface behind the fuel grain to further increase the edge contrast. When these images are loaded into the MATLAB code in Appendix B.1, it returns the regressed edge at the constant area section.

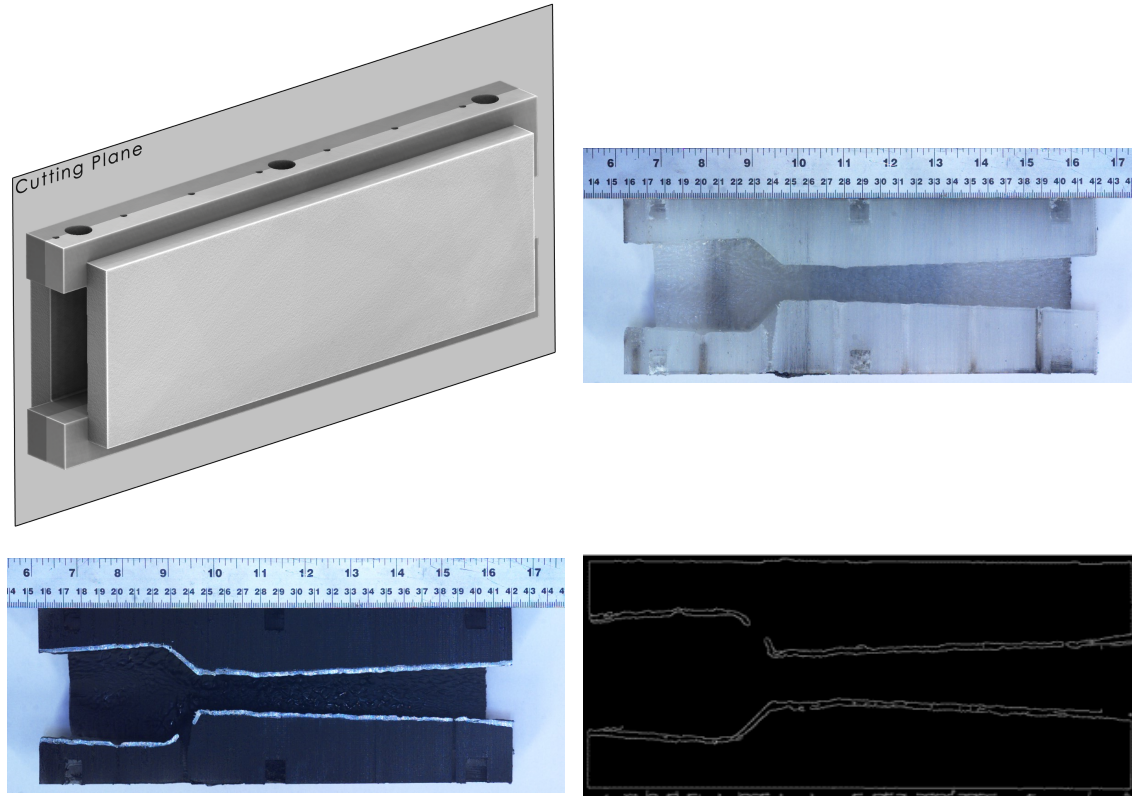


Figure 4.3: The process for cutting and analyzing the enclosed fuel grain for time-averaged regression analysis. The fuel grain is cut with a bandsaw along the cutting plane (top left) to produce two halves of a fuel grain (top right). The surface is painted black, and the edges are highlighted with white paint to increase contrast (bottom left). MATLAB’s Image Processing Toolbox returns the fuel grain edge (bottom right).

The second portion of the enclosed fuel grain experiments use a single geometry, but systematically decreases the temperature to examine the lower limits of inlet conditions. The geometry chosen is the most likely to sustain combustion based on the non-dimensional parameters, it is the furthest up and to the right on the flammability map. This corresponds to the geometry labeled A in Table 4.1, with each decreasing temperature firing from tests 1-5. The heater set point is decreased for each test until the fuel grain does not sustain

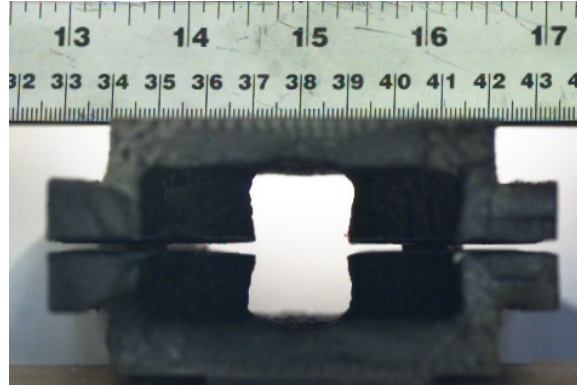


Figure 4.4: Representative image taken in the direction of the flow to measure the regression in the constant area section of the enclosed fuel grain.

ignition. The analysis and data collection is the same as the varying geometry portion of the experiment.

4.2 Results

The combustion experiments conducted using the fully enclosed fuel grain demonstrate that the flammability map limits, with adjusted parameters from previous studies, applies to non-axisymmetric combustors [6, 7]. The exhaust from the combustor is confirmed to be supersonic by the shock diamonds within the exhaust plume while firing in Fig. 4.5.

4.2.1 Varying Geometry Experiment

The test matrix in Table 4.1 provides both geometric parameters and inlet conditions of each test conducted. The order of Table 4.1 does not necessarily reflect the order of the tests conducted. The previously mentioned flammability map of geometric parameters in Fig. 4.2 indicate the geometric conditions that sustain combustion for a period of at least 5 seconds with a filled circle, and the non-sustained conditions examined are marked with an open

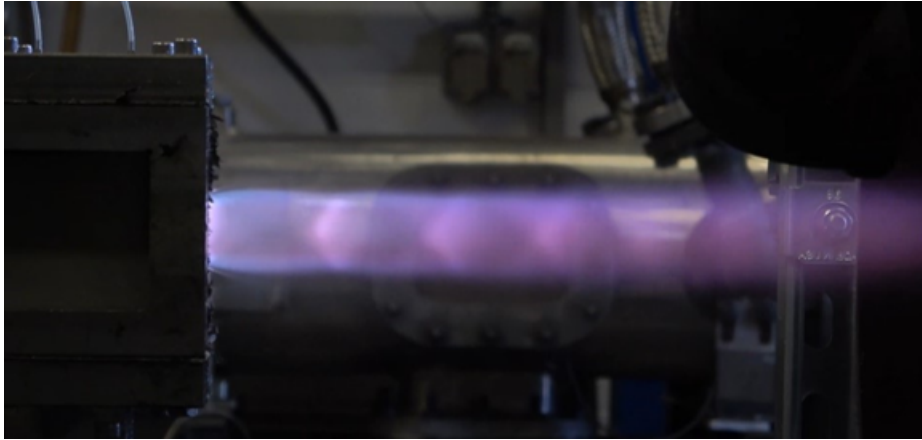


Figure 4.5: An exhaust plume from an enclosed SFSJ firing showing the shock diamonds. Flow from left to right.

circle. The triangle symbol represents a sustained re-ignition; defined as ignition beginning and extinguishing, then reigniting and sustaining for at least 5 seconds. This phenomenon is observed in fuel grains marked near the lower limits of the flammability map. The re-ignition is thought to be a result of the initial ignition stage consuming enough fuel to change the geometry into a more favorable condition, supporting a sustained ignition. These geometries have repeated firings to confirm the sustained re-ignition.

Compared to previous investigations with PMMA [6, 7, 54], these rectangular cross-section experiments have a lower inlet temperature resulting in higher required parameterized geometric values for ignition and sustained combustion. Although noticeable in both axes, the increase is primarily a concern for the relative size of the flameholding cavity to the inlet, plotted on the vertical axis of Fig. 4.2. For previous investigations [6], a value of around 7 is required for sustained combustion, however, the rectangular cross-section investigation requires approximately 15 for sustained combustion.

An example of the pressure data collected through the Scanivalve ports in the fuel grain are presented in Fig. 4.6. The varying geometry between fuel grains changes which section of the fuel grain the pressure ports are located. For example, the third pressure port can be

located in the flameholding cavity or in the constant area section depending on the length of the flameholding cavity. Most of the firings have similar pressure profiles to Fig. 4.6, with the exception being the initial fuel grain geometries which have wider constant area sections, as in Fig. 4.7.

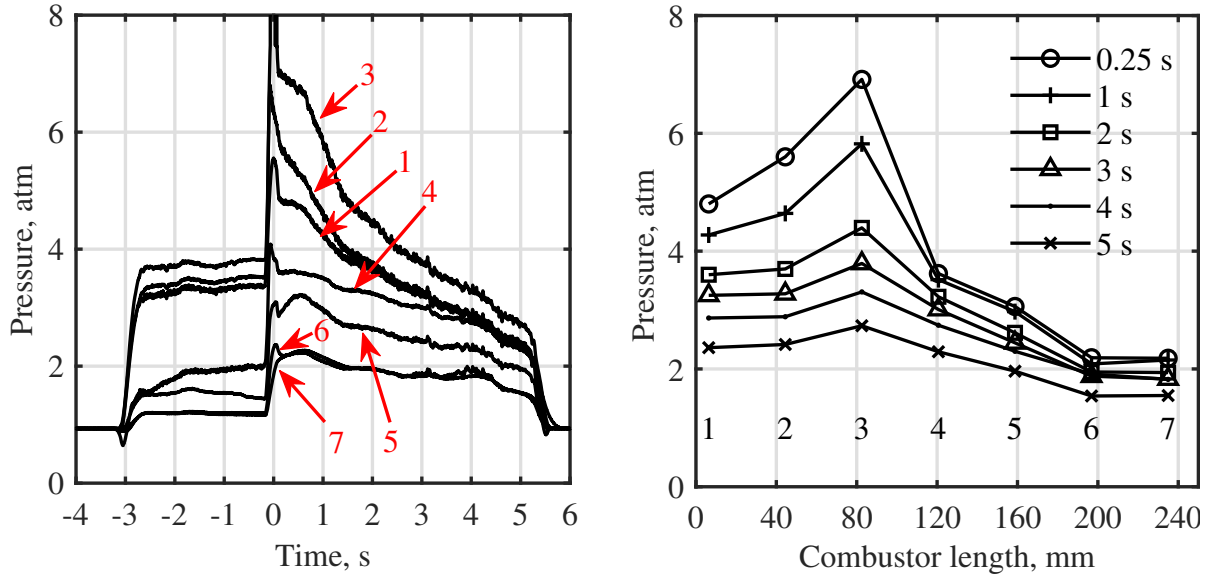


Figure 4.6: Wall pressure measurements of a typical enclosed fuel grain SFSJ combustion experiment, test 16. The numerical labels correspond to the pressure ports labeled on Fig. 3.2. Pressure-time measurements (left) and pressure-distance measurements (right) are plotted.

The pressure data begins collection when air starts flowing through the combustor. The data is adjusted so that the large spike in pressure positioned at 0 seconds in the left plot of Fig. 4.6 represents the instant of ignition. The drop in pressure shortly after the spike is the completed consumption of the igniter propellant leaving the remainder of the firing to rely exclusively on pyrolyzing PMMA. In this firing, the highest pressure is observed in pressure port 3, located in the angled converging section of the flameholding cavity. The pressure measured in ports 1 and 2, upstream in the flameholding cavity, is lower. The highest pressure is observed in port 3. The higher pressure at port 3 is likely due to flow stagnation occurring on the converging surface, but also could be an effect of more pyrolysis

and combustion occurring in this area. Sequentially decreasing pressure is observed in the constant area section at port 4 and in the diverging section at ports 5, 6, and 7. Pressure port 7, which is nearest the exit plane, sustains pressures of greater than 2 atmospheres during the entire firing. The elevated pressure near the exit plane is indicative of supersonic flow in the expansion region. A supersonic exhaust is further confirmed by the previously mentioned shock diamonds visible in the plume. The final sharp drop at around 5 seconds is the conclusion of the firing, terminated by the air flow being manually shut off.

The pressure throughout the entire fuel grain is observed to decrease steadily as fuel regresses and the cross-sectional area increases, as demonstrated in the right plot in Fig. 4.6. Immediately after ignition ($t=0.25s$), the pressure trace shows the highest pressure across the entire fuel grain, especially in the flameholding cavity (ports 1-3). As time progresses, and fuel is consumed, the pressure decreases. The pressures observed in the downstream section of the fuel grain decrease at a slower rate, likely due to the lower regression rate changing the cross-sectional area at a slower rate.

The pressure trace from geometries with a larger initial constant area section (larger H_{const}), do not produce a large dramatic spike at ignition. The larger cross-sectional area does not force thermal choking, and therefore does not create a high pressure zone in the upstream flameholding cavity. Figure 4.7 shows a significant difference in the pressure profiles of the tests with a larger constant area section. The video recordings of the plumes resulting from these fuel grains do not show shock diamonds. The lack of shock diamonds initially leads to the assumption that the flow velocity is dropping to a subsonic regime. However, upon reviewing the pressure trace at port 7 in Fig. 4.7, the pressure is greater than the atmospheric pressure throughout the entire firing. At this point, it is important to note that the higher elevation of the testing location decreases the atmospheric pressure at APPL to slightly less than 1 atm. Since the pressure near the end of the combustor and the atmospheric pressure

are close, the plume does not produce strong, visible shocks as it exhausts into the plume containment. Another note about these specific fuel grain geometries is the pressure tends to increase throughout the duration of the firing, likely due to additional mass being added to the flow at a slightly lower velocity.

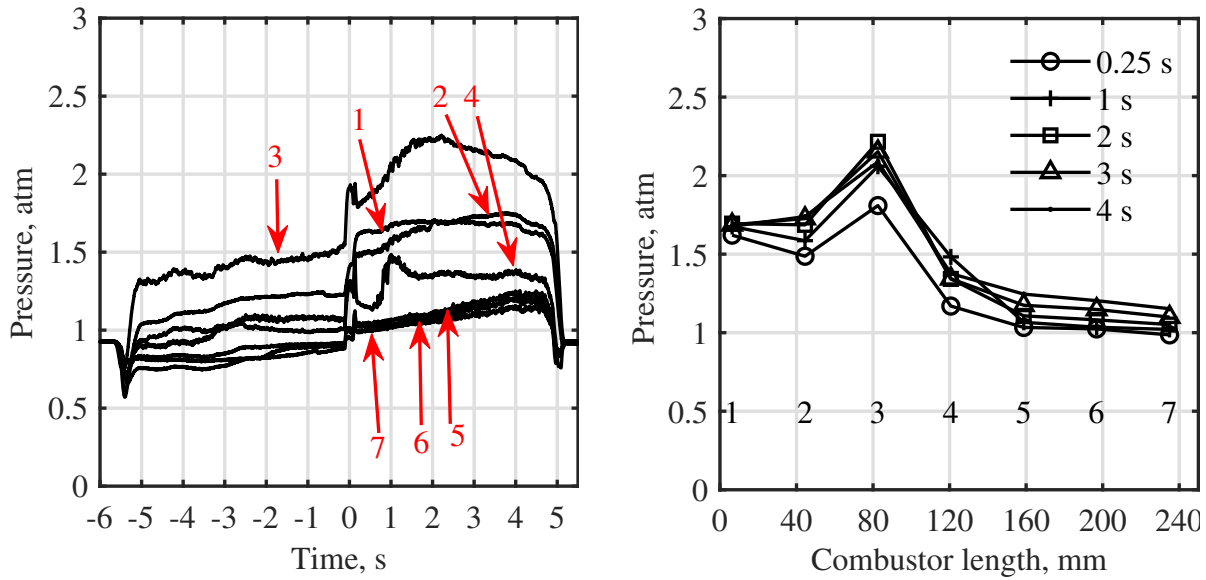


Figure 4.7: Wall pressure measurements from test 19, demonstrating the effects of a larger H_{const} on the pressure during combustion. The numerical labels correspond to the pressure ports labeled on Fig. 3.2. Pressure-time measurements (left) and pressure-distance measurements (right) are plotted.

The time-averaged regression rates are measured after each firing to prepare plots shown in Fig. 4.8 for each geometry. Figure 4.8 is an example of one side of a fuel grain post fire compared to its original geometry. Since collecting these measurements requires cutting the fuel grains in half, the regression is measured on both the left and right sides, then averaged, and divided over the elapsed time from a test, as determined by the pressure measurements. This process allows for the regression rate to be determined in the direction perpendicular to the combustor axis across the length of the fuel grain. Additionally, since the band saw effectively drags material through the cutting plane, there is expected to be some error in the measurements. The time averaged regression rates for the bottom of some selected fuel

grains are plotted in Fig. 4.9. The band saw cuts directly through the pressure ports on the top of the fuel grain, resulting in periodic gaps or spikes in the regression rate. For all future discussion involving the regression across the length of the enclosed fuel grain, the bottom side of the fuel grain is primarily considered. One additional point to consider is that the fuel grains do not ignite immediately upon contact with the heated air. This delayed ignition causes some melting and shearing to occur, and it removes some fuel and slightly changes the fuel grain geometry prior to combustion. There is no way of differentiating the shearing effect from pyrolysis, since the regression rate profiles in Fig. 4.9 are gathered from the difference between a known initial geometry and the measured final fuel grain geometry.

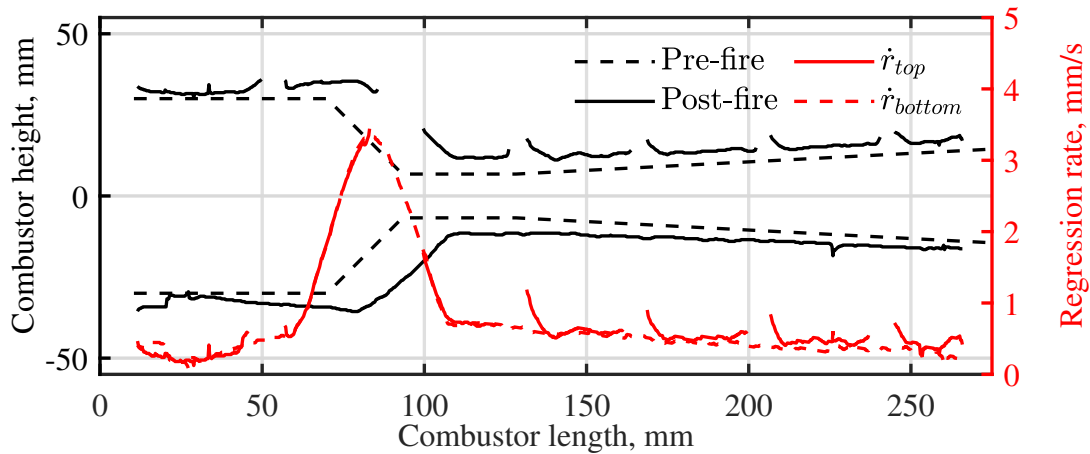


Figure 4.8: Representative plot showing pre- and post-fired fuel grains, as well as time-averaged regression rate, test 1.

Both Fig. 4.8 and Fig. 4.9 show significantly more fuel removed from the angled converging section of the flameholding cavity and the beginning of the constant area section. The average regression rate for this location is 3 to 5 times greater than anywhere else on the fuel grain. This is similar to the regression patterns observed by Ben-Yakar et al. and Cohen-Zur and Natan [6, 7].

Images are taken looking in the downstream direction from the opening of the fuel grain to

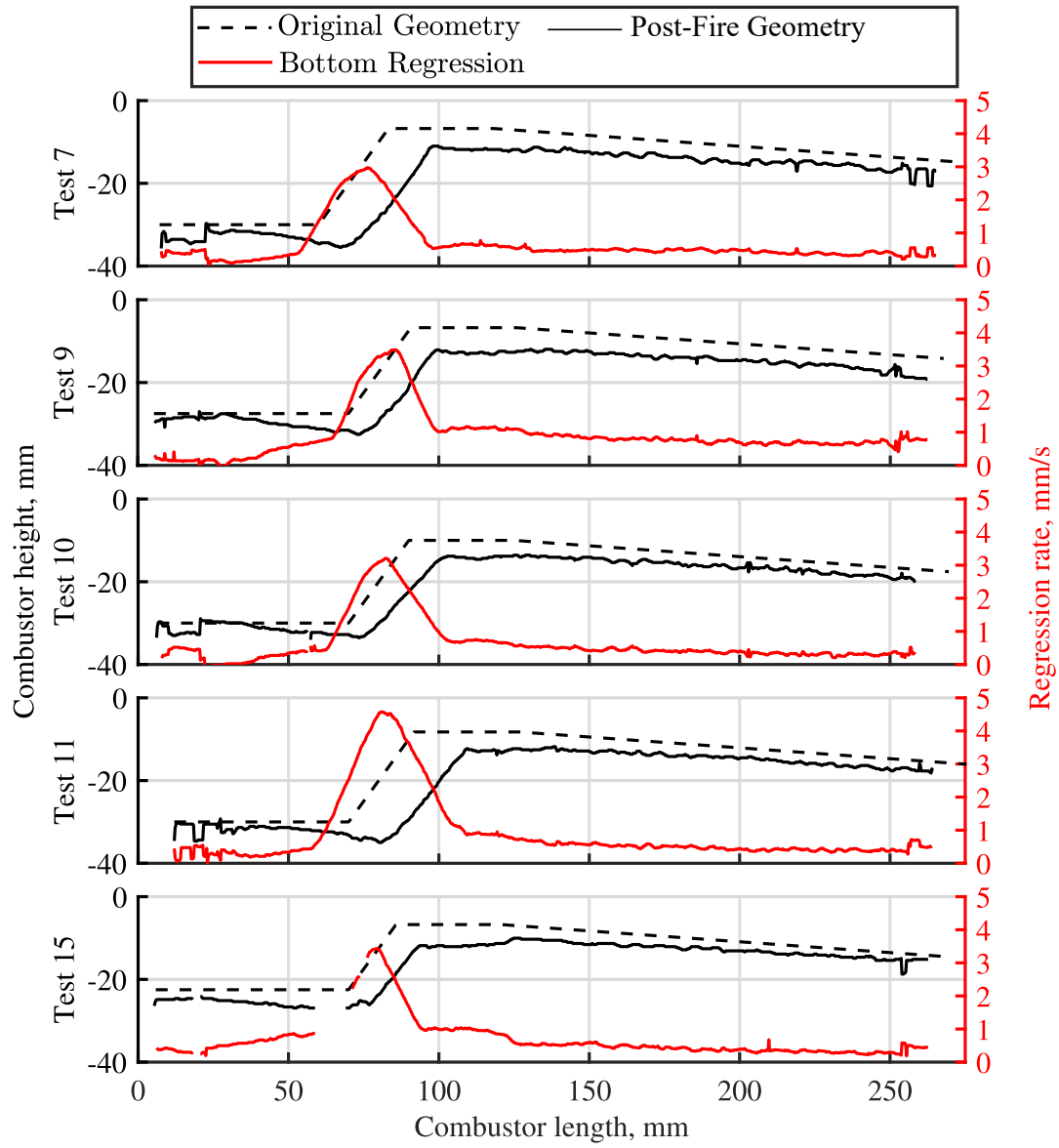


Figure 4.9: Representative plots showing average regression rate of the bottom of select fuel grains.

investigate the regression in the lateral side walls (x-axis of Fig. 4.10) of the constant area section. The regression rate at the constant area section is a pertinent location to study due to the belief of thermal choking. Qualitatively, the regression rate along the flat lateral walls of the fuel grains is observed to be uniform and small compared to the regression of the contoured top and bottom of the fuel grain.

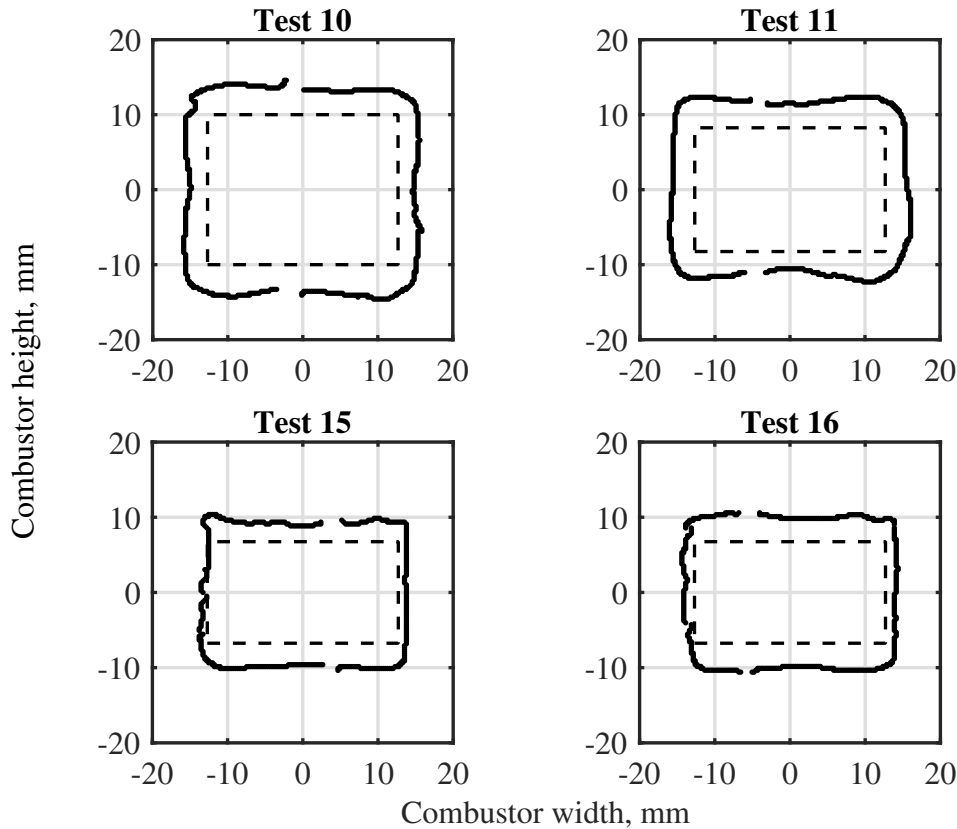


Figure 4.10: Representative plots showing time-averaged regression in the constant area section for selected tests.

To better understand the effects of the geometry changes on the regression rate, the rates measured from the constant area section are plotted in a 3-dimensional contour over the flammability map in Fig. 4.11. This contoured flammability map presents a clear correlation between increasing the non-dimensional parameters and an increasing regression rate. Although the increase is observed in all directions of the flammability map, there is a dra-

matic change in regression rates between fuel grains with widening constant area sections (previously discussed to not thermally choke). On the flammability map, this is observed when the relative size of the flameholding cavity ($H_{fh}L_{fh}/A_{in}$) parameter is large and the relative step height from the flameholding cavity to the constant area section (A_{fh}/A_{const}) parameter is decreasing. This idea agrees with conventional knowledge of flow fields. A flow field that is decreasing its velocity from supersonic to sonic produces higher local temperature and pressure effects than a flow that remains supersonic. Furthermore, Heller and Bliss [57] describe that the behavior of supersonic cavity flow is characterized by periodic fluctuations of mass exchange between the core flow and the flow in the cavity. By this understanding, a larger cavity creates a longer residence time of high temperature flow through the recirculation zone and increases the amount of heat transferred to the surface to increase regression rates. Increasing residence times is evidenced by Fig. 4.11; as both non-dimensional parameters increase with the relative size of the flameholding cavity, the regression rate is observed to increase.

To understand where most of the regression occurs during different stages of a firing, tests 1 and test 6 are set for the same conditions, but they are allowed to burn for different times. Table 4.2 presents a comparison between these two tests in regression data found in different locations. The shorter duration test experiences 173% greater maximum regression in the converging section at the end of the flameholding cavity. Comparatively, there is a 111% greater time averaged regression rate in the constant area section during the longer test duration. This evidence suggests that the initial flameholding and ignition relies heavily on the fuel in the flameholding cavity, then it begins to consume fuel from the rest of the fuel grain after a sustained flame is established. In both lengths of tests, the fuel removed in the diverging section is close to none, indicating that the majority of fuel consumed, and therefore the sustained combustion, primarily occurs in the flameholding cavity.

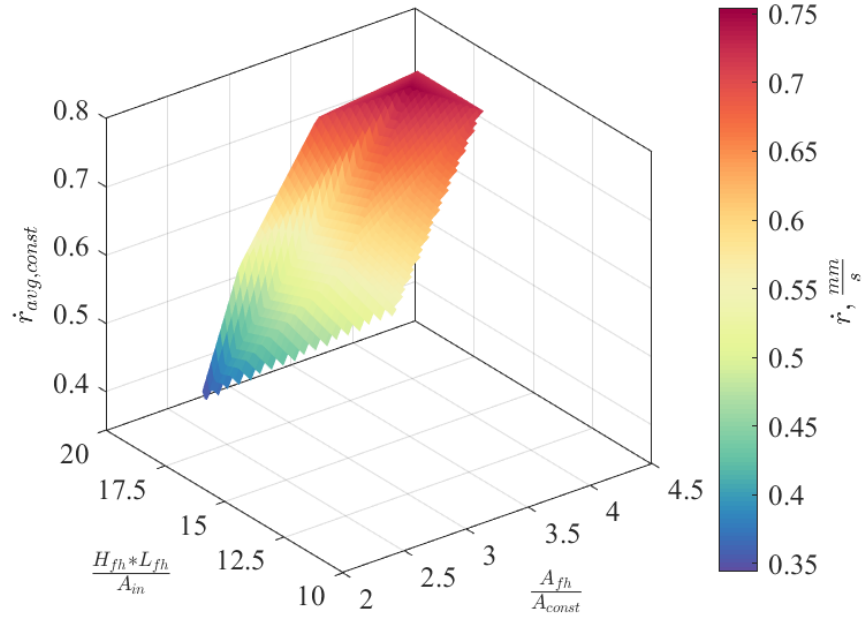


Figure 4.11: Average constant area section wall regression rates plotted with respect to geometric parameters.

To qualitatively analyze the post-fire fuel grain geometry, select grains are 3D scanned using an Artec3D Space Spider. The scanning system provides a 0.1mm monochromatic resolution to produce the images in Fig. 4.12. Upon initial observations, the sharp corners of the flameholding cavity are rounded, highlighting the increased amount of fuel removed in this area. The interior surface of the fuel grain has large roughness patterns, varying in size, but all much larger than the resolution of the 3D printed layer lines. The scale of the patterns

Table 4.2: Comparison of Varying Test Duration

	Test 1	Test 6
Test Ignition Time (s)	6.8	3.7
Test Temperature (K)	806	822
Average Regression, Constant Area Section (mm/s)	0.72	0.65
Maximum Regression, Converging Section (mm/s)	3.44	5.95
Average Regression, Full Grain (mm/s)	0.72	0.87

suggests that they are not a result of the 3D printing process, and instead present influences from the flow field. A characteristic waviness and roughness is present in the diverging section, similar to the observations from axisymmetric investigations of SFSJ [6, 87]. The scans, however, also show a similar roughness near the converging section of the flameholding cavity and near the central flow directly out of the nozzle. This unique patterning is believed to be a result of the corners creating eddys or larger scale turbulent patterns.

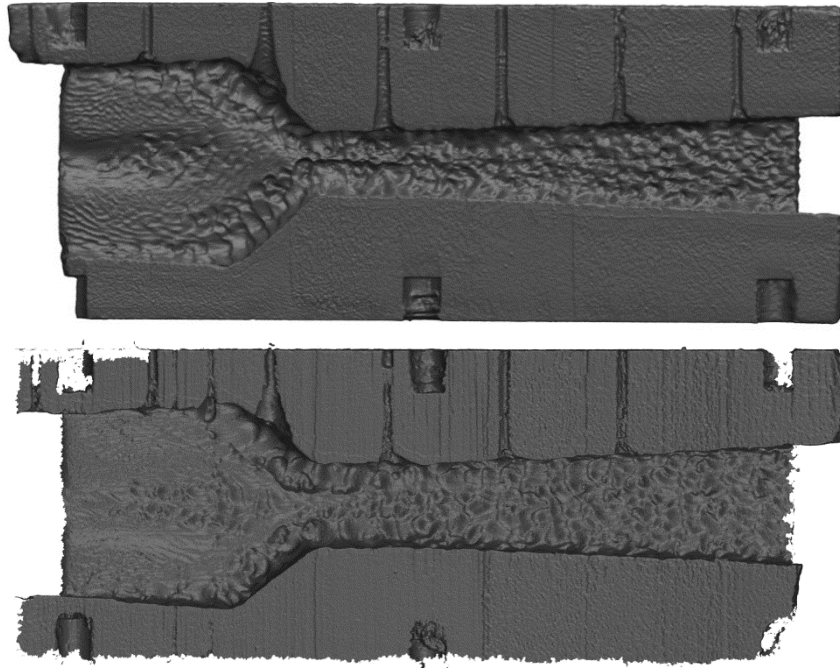


Figure 4.12: Cut and 3D scanned fuel grain, flow from left to right, test 1 (top) and test 10 with larger initial H_{const} (bottom).

The scanned fuel grains which are previously discussed to have not been thermally choked due to a larger constant area section (H_{const}), have this same patterning in a much smaller scale. This size difference is postulated to be a result of higher velocity flow occurring without choking, reducing the size of the eddys. The qualitative differences between a fuel grain that is believed to be choked and unchoked are shown in Fig. 4.12.

4.2.2 Varying Temperature Experiments

The fuel grain geometry A in Table 4.1 is fired at systematically lower temperatures in tests 1-5, and the results are summarized in Table 4.3. A consequence of varying temperature is also a varying mass flow rate through the combustor. From the minimum temperature (716 K) to the maximum temperature (806 K), there is about a 6% increase in flow rate, corresponding to a 12.5% decrease in temperature. Based on the established correlation in Eqn. 2.5 from Cohen-Zur and Natan [7], the regression rate is primarily influenced by the temperature of the flow.

Table 4.3: Tested Enclosed Fuel Grain Varying Temperature

Test Number	Air Temp (K)	Flow Rate (g/s)	Ignition Delay (s)	Ignition Pressure (atm)	Sustained Ignition
1	806	246	3.0	7.2	Yes
2	790	248	3.8	7.0	Yes
3	772	251	5.1	6.4	Yes
4	754	254	7.1	4.3*	Yes
5	716	261	N/A	N/A	No

* The cavity ignition pressure is measured at pressure port 2, due to insufficient pressure data at port 1.

Table 4.3 summarizes the ignition delay and peak pressure at port 1 from the firings which changed inlet temperatures. The temperature is systematically decreased until a lower limit is reached. The ignition delay more than doubles as the temperature decreases to the lowest examined temperature. The measured pressure in the flameholding cavity changes by a similar interval. Extreme changes are expected as the lower operational limit of the combustor is achieved. Since pyrolysis is primarily driven by heat transferred to the fuel grain [40], a lower temperature results in less pyrolysis occurring on the surface of the fuel. Less fuel being pulled into the flow leads to a lower equivalence ratio and lower heat released from the fuel. Additionally, as the temperature decreases the combustor moves from thermally choked at the constant area section, to unchoked, further reducing the likelihood of ignition.

The regression rate from the varying temperature fuel grains is measured in the same process as the varying geometry fuel grains. The transition from thermally choked to unchoked in the constant area section as temperature decreases directs a deeper investigation to the regression rate at the constant area section. Figure 4.13 plots the time averaged regression rate in the constant area section at each of the temperatures tested. It shows a distinction between the top and bottom, and lateral walls in this location, as well as the average regression rate for the full cross-section. Considering the temperature only decreased by 50 K, the change in regression rate is large. The significantly lower regression rates, explained by the lack of thermal choking, parallels the results found from the fuel grain geometries with larger constant area sections (H_{const}). Beyond that, as temperature increases, a higher regression rate is measured. A decreasing regression rate resulting from decreasing inlet temperature is consistent with previously discussed regression rate empirical models.

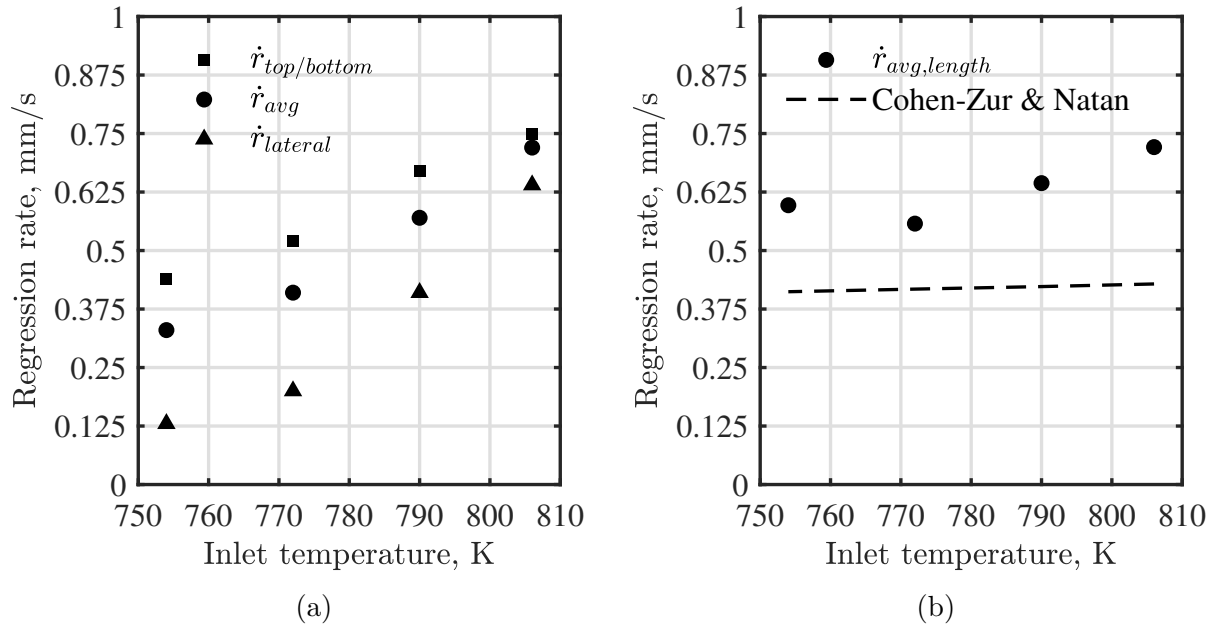


Figure 4.13: Time-averaged constant area section regression rates plotted with respect to varying temperature of air (left). Time-averaged top/bottom regression rates across the length of the fuel grain compared to a regression rate correlation from Cohen-Zur & Natan [7] (right).

The regression rate for each of the sustained firings with decreasing temperature is plotted in Fig. 4.14. The most observable difference between each of these plots is at the maximum regression location, near the downstream end of the flameholding cavity. The average regression rate down the length of the fuel grain is plotted in comparison to the regression rates calculated from Eqn. 2.5 in Fig. 4.13. The decreasing trend is similar in slope. However, the rectangular fuel grain presents considerably higher time-averaged regression rates than the correlation. This can be explained by the correlation originally being obtained in higher temperature, pressure, and mass flow rate conditions than the current rectangular cross-section fuel grains. Additionally, as previously mentioned, the regression rate measured for the rectangular cross-section experiment cannot differentiate between fuel removed by pyrolysis, and fuel removed by melting and shearing. The fuel grains used by Cohen-Zur and Natan also have a larger port area than the rectangular cross-section fuel grains. Furthermore, the regression rates calculated in an axisymmetric fuel grain are assumed to be equally distributed in all directions radially from the center perforation. This assumption cannot be made for a rectangular cross-section fuel grain, and therefore it can be expected to experience more irregular distributions of the regression [7].

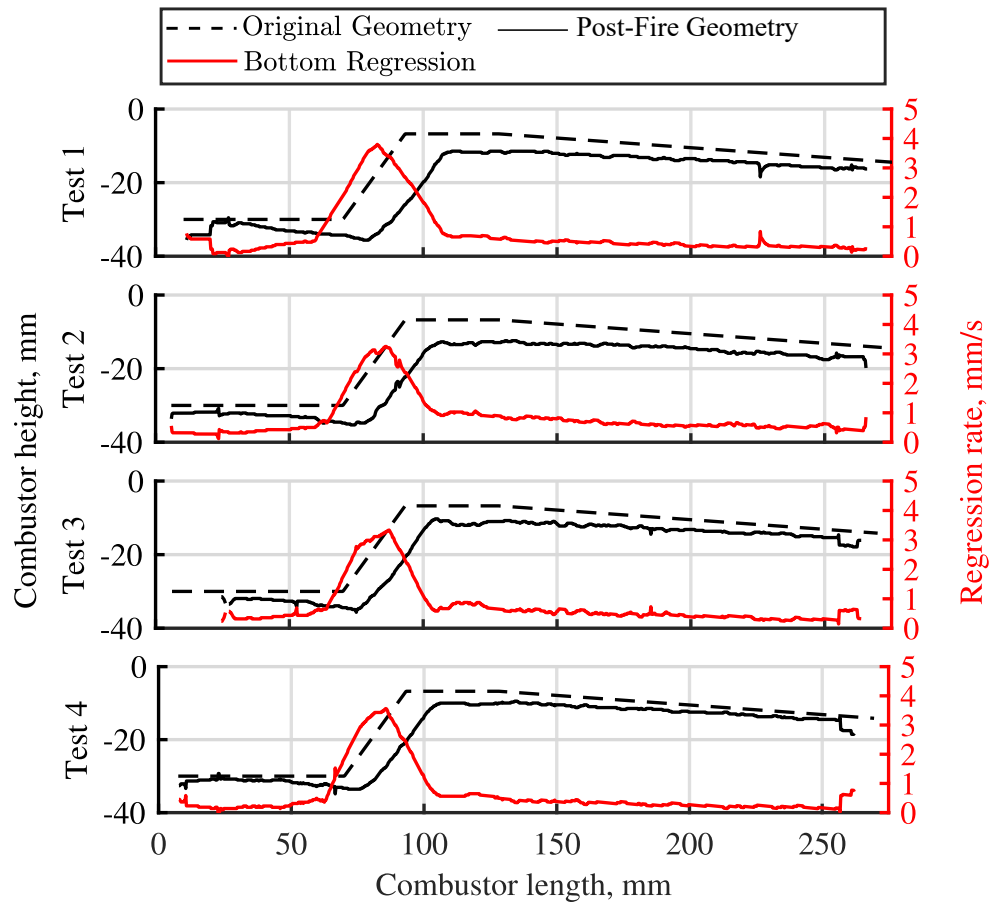


Figure 4.14: Regression profiles and regression rates of varying fuel grain experiments, tests 1-4.

Chapter 5

Optically Accessible SFSJ

Experiments

This chapter explains the process and results from the optically accessible solid fuel scramjet combustion experiment. This is the first known optically accessible combustion of a SFSJ, and it provides a new insight on the complexities of supersonic solid fuel combustion. The optically accessible SFSJ experiments use high speed video recording as the primary source of data acquisition. This experiment focuses less on flammability limits of the SFSJ and more on the flow field and combustion process observed through the quartz windows.

5.1 Experimental Procedure and Data Collection

To conduct the experiments, the 50.8 mm wide combustor is outfitted with separated top and bottom fuel grains to allow for observations through the quartz side windows in Fig. 3.3. Once the top and bottom of the fuel grain are secured into the combustor, the air flow is opened through the bypass pipe while the electric heater is given time to warm up to the desired temperature. After the heater achieves the required temperature, the firing sequence is initiated which consists of a 5 second delay to initialize data collection systems, 6 seconds of electrically heated air flowing through the combustor, 3 seconds of burning the ethylene/air torch to further increase the inlet air temperature and trigger ignition, and 2 seconds of

continued electrically heated air flow through the combustor without the torch. Then, the air is switched back to the bypass pipe while nitrogen flows through the combustor and the ethylene torch to ensure all combustion reactions have stopped. The total time allotted for combustion after the ethylene torch is ignited is limited to 5 seconds total to avoid damaging the facilities.

Within the optical SFSJ experiments, seven fuel grain geometries are examined, with two geometries being selected for the remainder of optical analyses including shadowgraphy, chemiluminescence (CL) imaging, and regression rate measurement. The two primary fuel grains are labeled A and B, with the only difference between them being the length of the flameholding cavity. The geometries are listed in Table 5.1. The shadowgraph imaging is set up according to the diagram in Fig. 5.1 using the high speed camera and concave mirrors.

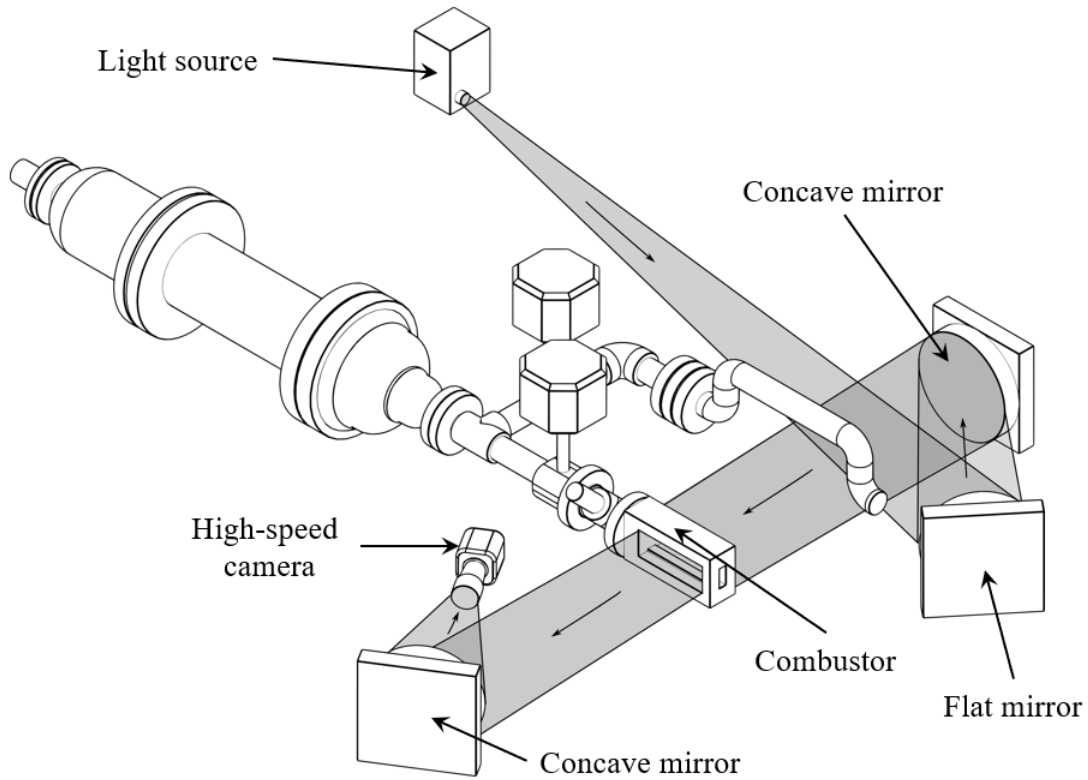


Figure 5.1: Schematic of shadowgraph setup.

Table 5.1: Tested Optical Fuel Grain Geometries

Test # & Geo	H_{fh} <i>mm</i>	L_{fh} <i>mm</i>	H_{const} <i>mm</i>	$\frac{A_{fh}}{A_{const}}$	$\frac{H_{fh}L_{fh}}{A_{in}}$	Sustained Ignition	Test Focus
1 A	50	70	6.61	7.6	16.0	Yes	Ignition and Regression
2 B	50	85	6.61	7.6	19.4	Yes	Ignition and Regression
3 A	50	70	6.61	7.6	16.0	Yes	Regression
4 C	50	85	14	3.6	19.4	No	Ignition
5 D	50	85	8.0	6.3	19.4	Yes	Ignition
6 E	50	55	6.61	7.6	12.6	No	Ignition
7 F	50	85	11	4.5	19.4	No	Ignition
8 G	50	100	6.61	7.6	22.9	Yes	Ignition
9 B	50	85	6.61	7.6	19.4	Yes	Regression, Full CL
10 A	50	70	6.61	7.6	16.0	Yes	Regression
11 A	50	70	6.61	7.6	16.0	Yes	Regression, Full CL
12 A	50	70	6.61	7.6	16.0	Yes	Regression
13 A	50	70	6.61	7.6	16.0	Yes	Regression, Shadowgraph
14 B	50	85	6.61	7.6	19.4	Yes	Regression, Shadowgraph
15 A	50	70	6.61	7.6	16.0	Yes	Cavity CL, HS
16 B	50	85	6.61	7.6	19.4	Yes	Regression, Cavity CL, HS
17 B	50	85	6.61	7.6	19.4	Yes	Regression, HS
18 B	50	85	6.61	7.6	19.4	Yes	Regression, HS

All tests are conducted with air inlet at a nominal $T_{in} \approx 1225K$, $\dot{m}_{in} \approx 200g/s$

For all geometries:

$$L_{const} = 35mm, \alpha = 45^\circ, DivergingAngle = 1.5^\circ, H_{in} = 4.39mm$$

The optical accessibility of the combustor provides unique opportunities for improved analysis. The regression rate is measured by a MATLAB code printed in Appendix B.2 that displays individual frames of the combustor from a real-time video. As each frame is displayed, the fuel edge is selected at specific time intervals. The MATLAB Image Processing Toolbox cannot be used on the fuel grains while they are combusting because PMMA appears to glow and reflect in the quartz windows while burning. The edge recognition program used in Chapter 4 only works effectively at edges with high contrast. The experimental uncertainty of manually measuring the regression rate is calculated based on methods described by Kline and McClintock [88] in Appendix A.

The CH^* chemiluminescence video is time-averaged and scaled to provide a normalized intensity of the radicals resulting from combustion. In addition to imaging of the full combustor, the camera is positioned to zoom into the flameholding cavity to provide finer details.

5.2 Results

5.2.1 Ignition Experiments

The sustained ignition of an optically accessible SFSJ provides previously unattainable insight into the flow mechanics and characteristics of supersonic solid fuel combustion. It is determined that removing the fuel on the side walls from Chapter 4 reduces the surface area of fuel exposed to the flow by 52%, and the system experiences a major decrease in the equivalence ratio. To solve this problem, a wider combustor is used with the same inlet pressure and converging/diverging nozzle area ratios to create a Mach 2 flow. Additionally, to allow for an uninterrupted line of sight through the combustor for the entirety of the firing, and consistent ignition timing between firings, an ethylene/air torch is used to increase the temperature for ignition instead of the HTPB-AP propellant.

Despite these changes, the results of the wall pressure measurements from the Scanivalve are consistent between the two experiments. A sample of pressure measurements for each of the two primarily examined fuel grain geometries is shown in Fig. 5.2, where the pressure spike at the instant of ignition is set to 0 seconds. The ethylene torch is burning from approximately -0.5 seconds until 2.5 seconds. The pressures measured from the optical SFSJ are typically lower than the enclosed SFSJ. Although the amount of fuel exposed to the fuel is the same between the experiments, there are some other differences to consider. The ethylene torch increases the temperature of inlet air to approximately 1225 K while reducing the nominal

mass flow rate of air through the combustor to 200 g/s. Since mass flow rate and pressure are directly proportional by $\dot{m} \propto PA/(T)^{1/2}$, the pressure through the optical SFSJ is lower [89].

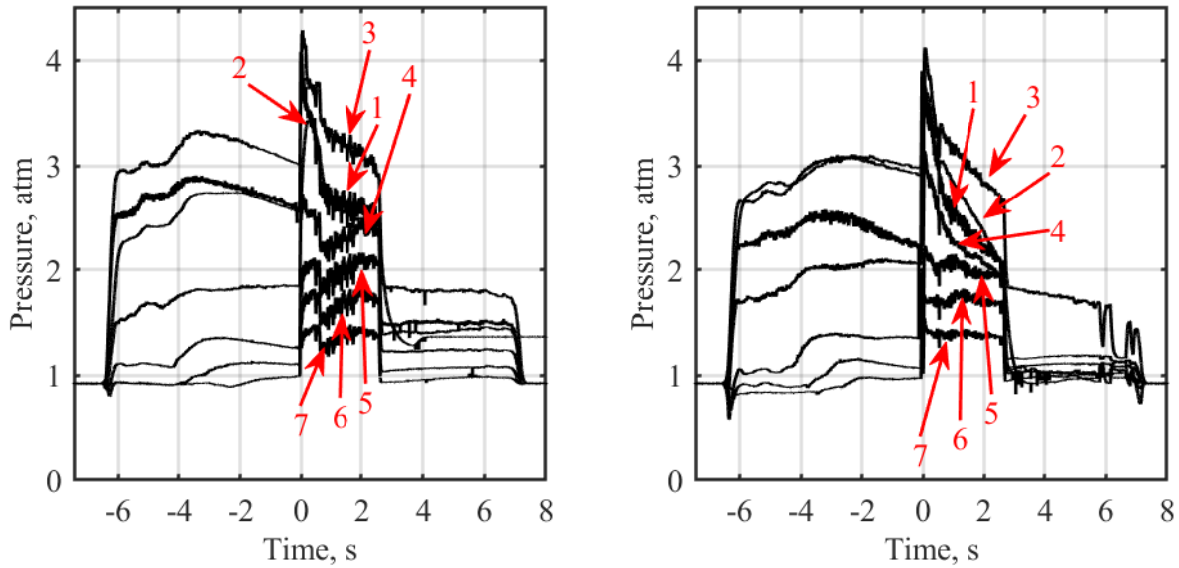


Figure 5.2: Typical Scanivalve pressure measurements for optical SFSJ. Fuel grain geometry A, test 1 (left). Fuel grain geometry B, test 2 (right).

Following the first two sustained ignitions of the optically accessible SFSJ, it is observed that the visible core flow biases to the top in fuel grain geometry B, whereas fuel grain geometry A remains symmetric. The bias is abundantly clear in the snapshots taken from real-time video recordings in Fig. 5.3.

The initial firings attribute the bias to the size of the flameholding cavity causing high pressure oscillations, effectively treating both the top and bottom flameholding cavities as a single large recirculation zone. Zhang and Edwards [58] describe the influence of the length to depth ratio of a cavity (L/D) on pressure oscillations propagating into the free stream. A small L/D produces small vortices attached to the front wall that do not affect the shear layer or the free stream. A larger L/D produces larger vortices at this wall that deflect the shear layer into the free stream, shown in Fig. 5.4. An angled back wall in the cavity is

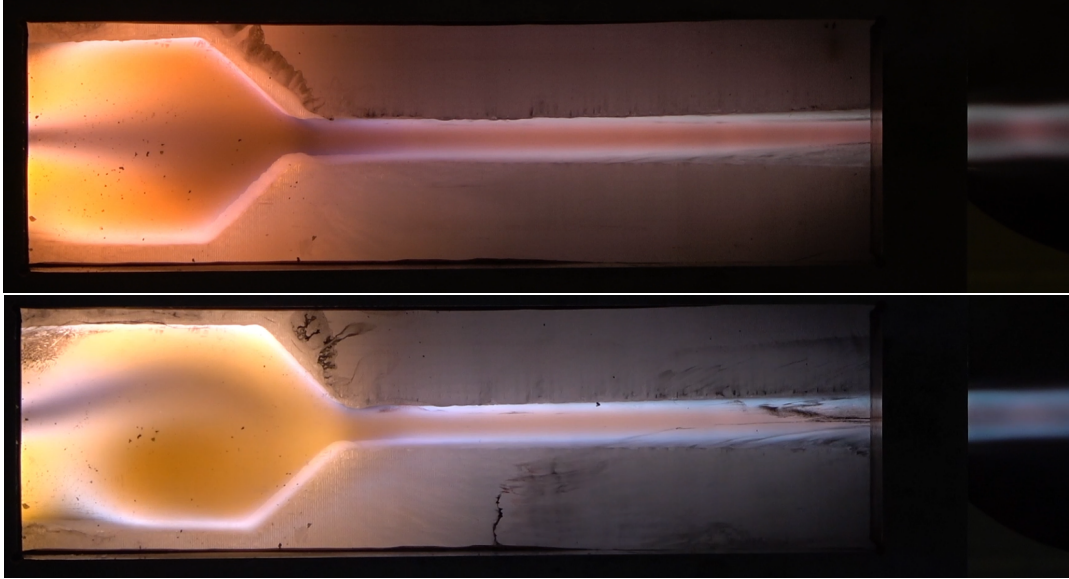


Figure 5.3: Combusting samples of the optical SFSJ, demonstrating a biasing phenomena. Flow from left to right. Symmetric core flow during optical SFSJ firing of geometry A, test 1 (top). Upward biased core flow during optical SFSJ firing of geometry B, test 2 (bottom).

shown to suppress the cavity oscillations, but a large L/D can overcome the effects from the angle and create high enough pressure in the cavity to cause instability [3, 8, 58].

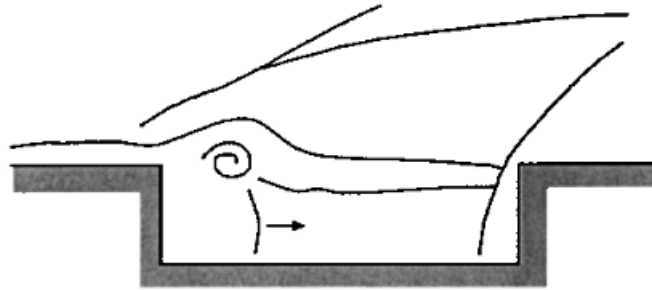


Figure 5.4: Visualization of a vortex attached to the front edge of a cavity that deflects the shear layer into the free stream [8].

To determine how the flow biasing is related to the fuel grain geometry, multiple geometries of varying flameholding cavity lengths (L_{fh}) and varying constant area section heights (H_{const}) are examined in cold flow shadowgraphs. The cold flow shadowgraphs utilize air that is coming directly from the compressor without engaging the heater. This produces air inlet

temperature around 300 K. Snapshots from each of the geometries tested in the cold flow shadowgraph are displayed in Fig. 5.5. All of the fuel grains cause bias in the core flow except for the fuel grain with the shortest cavity length, fuel grain E. The flow through fuel grains A, B, C, D, and F, all look similar: an upward biasing core flow. The core flow through fuel grain G biases downward, but otherwise looks similar in structure to the other biasing fuel grain geometries.

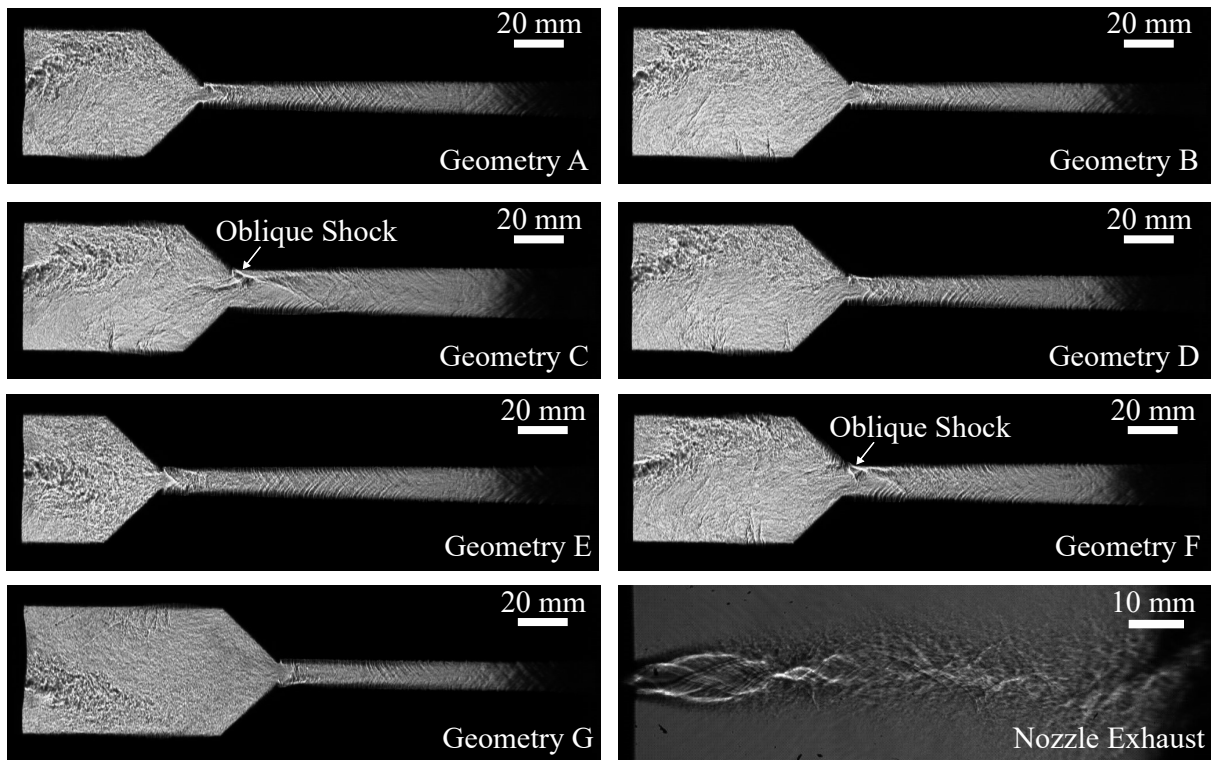


Figure 5.5: Cold flow shadowgraph of multiple fuel grain geometries and flow directly from the C/D nozzle. Flow from left to right.

Geometries C and F have the largest constant area section and have a single oblique shock extending from the top of the fuel grain and through the entire constant area section. The oblique shock is a result of the flow interacting with the converging section of the flameholding cavity. It is present and visible due to the flow not choking at the constant area section. The choking of a flow normalizes the alignment of the flow at its narrowest point. Since the

flow field in geometries C and F are not choking, the flow remains unsymmetrical for the entire length of the combustor.

To additionally confirm that the combustor does not have an inconsistency in its design and construction, a cold flow jet is exhausted directly out of the converging/diverging Mach 2 nozzle, in the bottom right image of Fig. 5.5. Aside from the oscillatory nature as the supersonic flow encounters the quiescent atmospheric air, the flow directly from the nozzle is symmetric, leaving the conclusion that the asymmetric behavior is related exclusively to the fuel grain geometry.

Each of these additional geometries is combusted in tests 3-8 in Table 5.1 and are plotted on a flammability map in Fig. 5.6. Geometries C, E, and F do not sustain combustion, while A, B, D, and G all ignite and sustain combustion. None of the examined fuel grains experience sustained re-ignition. On the flammability map, the non-dimensional geometric parameters are much higher than from the previous experiments shown in Fig. 4.2. Due to the limited number of fuel grain geometries examined, no explicit ignition limit is found on the flammability map in Fig. 5.6.

The cases where a large L/D causes unsteady pressure oscillations in the SFSJ, such as the longer flameholding cavity of geometry B, demonstrate a reduction to a single, large recirculation zone that expands to fill both the top and bottom flameholding cavity. The larger L/D induces large vortices within both flameholding cavities that deflect the shear layer into the core flow, like in Fig. 5.4. It is believed that, since the SFSJ has two opposing cavities, a geometry with a large L/D causes competition between the top and bottom. The pressure from one side eventually overpowers the other, creating a single, larger recirculation zone. Although this is not always the case, the single recirculation zone is mostly seen attached to the bottom flameholding cavity, biasing the flow upward (the core flow in geometry B in Fig. 5.11 biases down). The high pressure from the vortices in the top cavity are slightly

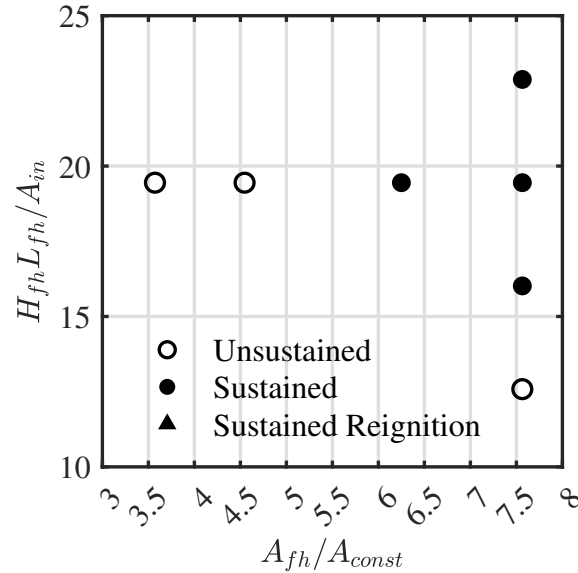


Figure 5.6: Flammability map from the optically accessible SFSJ. Due to the limited geometries examined, no flammability limit has been explicitly determined.

diminished due to the pressure ports.

Geometry A shows flow biasing in the cold flow examination, but not while combusting. This relates to the fuel grain geometry changing during the test. The changing geometry increases the depth of the flameholding cavity to a lower L/D that can maintain stable vortices without interfering with the core flow. The geometry of the cavity is altered when the fuel pyrolyzes at the surface and increases the ratio of flameholding cavity height with respect to the other geometric parameters. Fuel grain geometry E, although it shows symmetric flow in the cold flow, is below the ignition limits of this combustor and does not sustain combustion. A balance must be found between having a large enough cavity for sustained combustion, but a small enough L/D to prevent unstable pressure oscillations.

To confirm this hypothesis, the high-speed camera is positioned to record the cavity of geometry A at 5000 frames per second in Fig. 5.7. At 0.0 s, the light glow is the ethylene torch ignition and at 0.0460 s, the PMMA fuel grain ignites. Additional snapshots from the video show the oscillation of the core flow alternating between up and down before it settles

at centered with minor oscillations from 1.1016 s until the conclusion of the firing. These snapshots show that there is a relation between the startup of ignition, the regressing fuel grain, and the biasing of the core flow in a fuel grain cavity that is near the limit of a stable L/D .

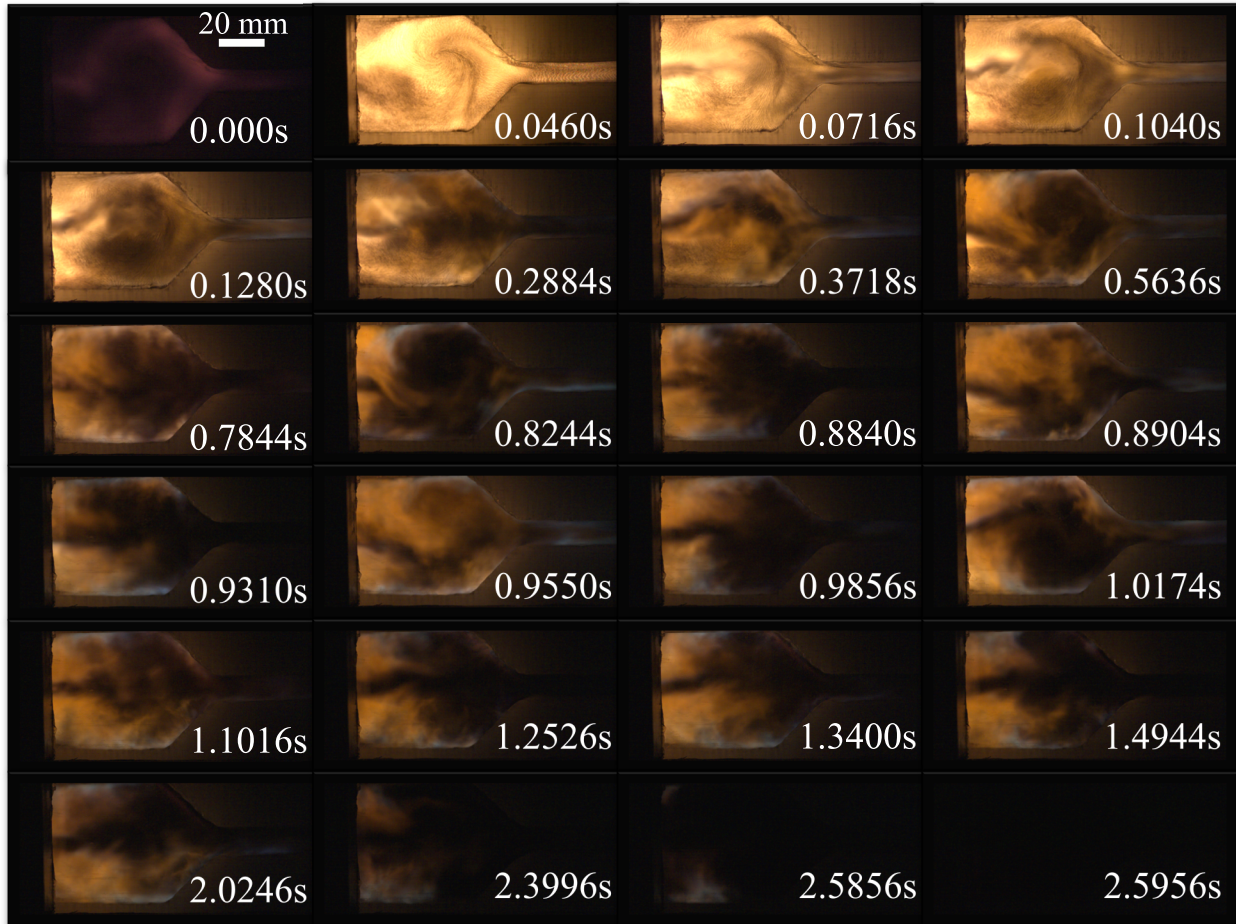


Figure 5.7: Snapshots of high speed video of combustion on geometry A, flow from left to right. Non-uniformed time increments are chosen to show each time the flow bias changes direction, test 15. Scaling is the same for all snapshots.

The shadowgraph set up is applied to a combustng flow of geometries A and B in tests 13 and 14. Recording clean videos with the shadowgraph is difficult because soot buildup prior to ignition blocks the light shining through the quartz windows. The soot is visible in the early frames in Fig. 5.7, and it prevents this imaging technique from being used to study

the oscillatory startup biasing. Only about 1.5 seconds out of a 3 second firing has clean enough windows for shadowgraph data collection. Even during combustion, some soot is still present near the fuel grain edge in the recording. Videos showing the shadowgraph of combustng flow are recorded at 7000 frames per second and snapshots are shown in Fig. 5.8 and Fig. 5.9.

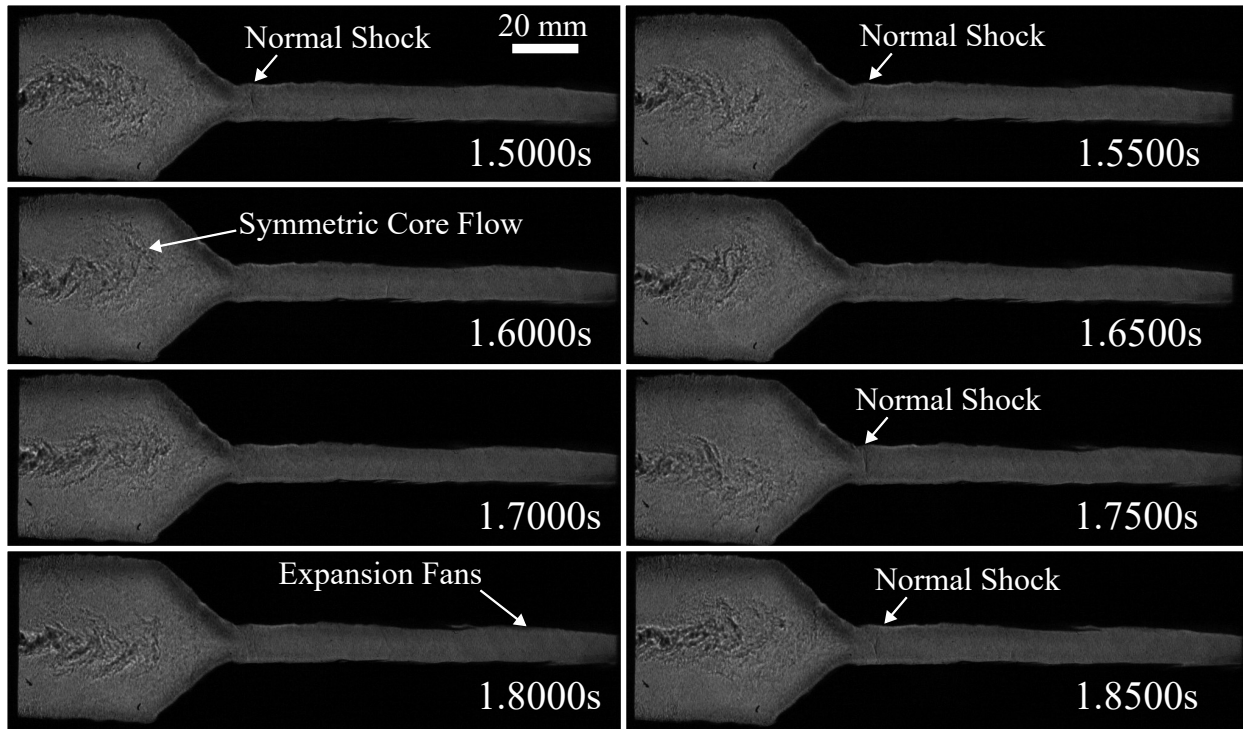


Figure 5.8: Snapshots of combustng shadowgraph video on geometry A, flow from left to right, test 13. Scaling is the same for all snapshots.

In addition to the obstruction from soot, the shadowgraphs exhibit highly turbulent and complex flow fields. A faint normal shock is visible in the opening to the constant area section in some frames, and faint expansion fans are visible in the diverging section. The presence of a normal shock in the constant area section further demonstrates that the flow is supersonic in this region. The flow biasing is clearly present in Fig. 5.9. The two dark spots in the diverging section are water droplets that splashed from the plume containment onto the exterior of the window. They do not alter the flow or combustion. The oblique shocks

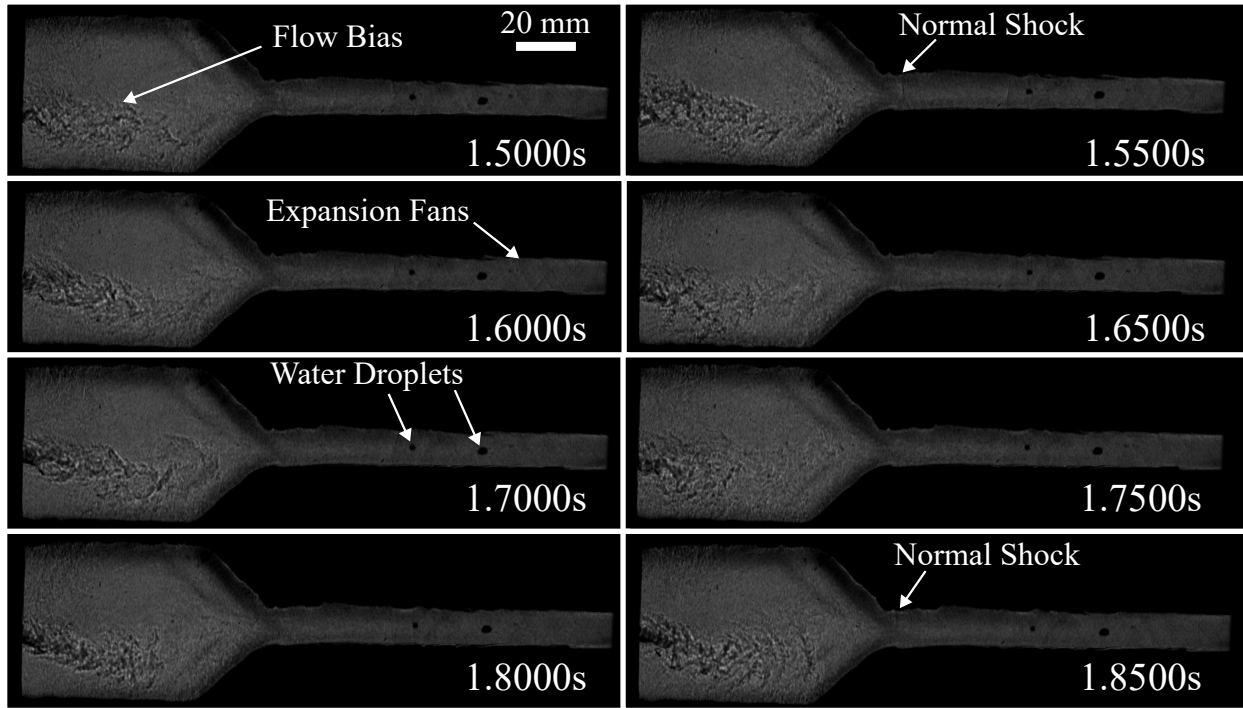


Figure 5.9: Snapshots of combustng shadowgraph video on geometry B, flow from left to right, test 14. Scaling is the same for all snapshots.

that are present in the diverging section of the cold flow shadowgraph images in Fig. 5.5 are not present in the combustng flow shadowgraphs. The heated flow removes the textured surface from the 3D printing process, and it does not form oblique shocks.

High speed solid fuel combustion has limited published literature involving chemiluminescence [77]. As discussed in Chapter 2, liquid fuel scramjets, and high speed cavity flows have recently become one of the focuses of this technique. To record the CH^* radicals in the optical SFSJ, the camera is initially set to view the full fuel grain at 4000 frames per second. Time-averaged CH^* chemiluminescence over the middle 1 second of combustion is shown in Fig. 5.10. The original fuel grain geometry is plotted in a white dotted line. Seconds 1 through 2 after ignition is selected because this is when the quartz windows are most cleared of soot and, based on the analysis of Fig. 5.7, the flow field of geometry A has stabilized. Both fuel grain geometries show the highest intensity of combustion in the upstream region

of the flameholding cavity near the fuel grain wall. The flow biasing is present in Fig. 5.10 for geometry B, where it appears that the core flow impinges on the top surface of the fuel grain and limits the combustion reaction there.

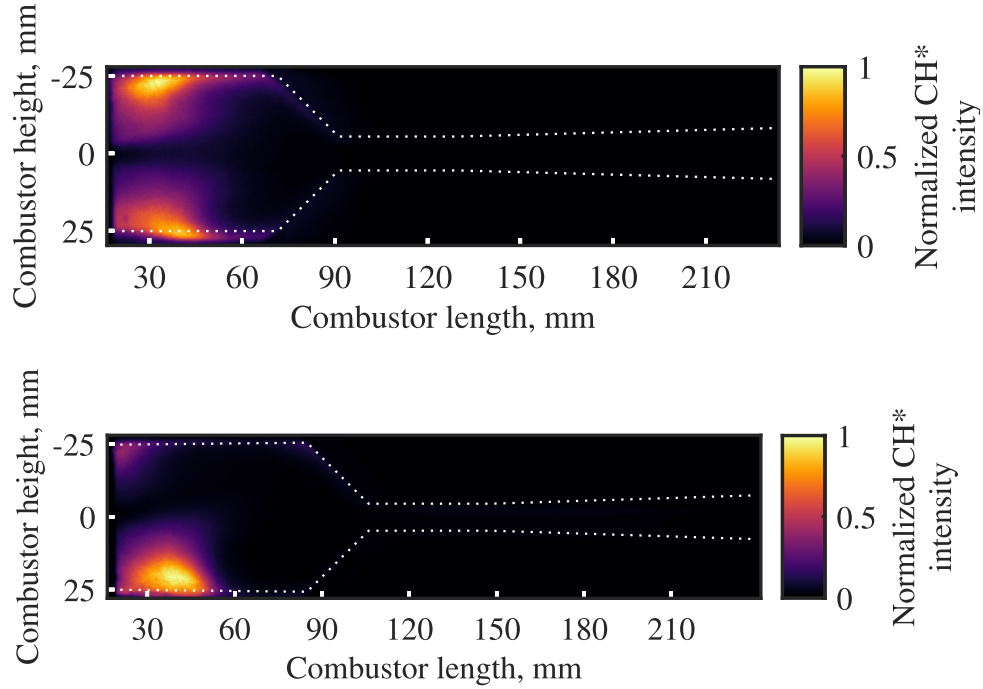


Figure 5.10: Geometry A, test 11 (top), and geometry B, test 17 (bottom) time-averaged CH^* chemiluminescence from full length of fuel grain, flow from left to right.

In both tests that measure the CH^* intensity across the entire fuel grain, there is little observable heat release occurring in the constant area and diverging sections. Although this could be a result of exposure time or the optical path through the window, the concentration of heat release prompted two more firings with CH^* chemiluminescence that zoom into the flameholding cavity at 20000 frames per second. The 1 second time-averaged intensities of CH^* radicals in the flameholding cavity are displayed in Fig. 5.11 with the original geometry shown in a white dotted line. Similar to the measurements from the full fuel grain, the highest intensity is at the upstream region of the flameholding cavity. By focusing on this area, the normalized intensity is more prevalent along the angled wall of the cavities, but still the

highest intensity is focused in the upstream area near the walls of the fuel grain. In test 16, the core flow through fuel grain geometry B biases downward, resulting in higher CH^* intensity on the top fuel grain wall.

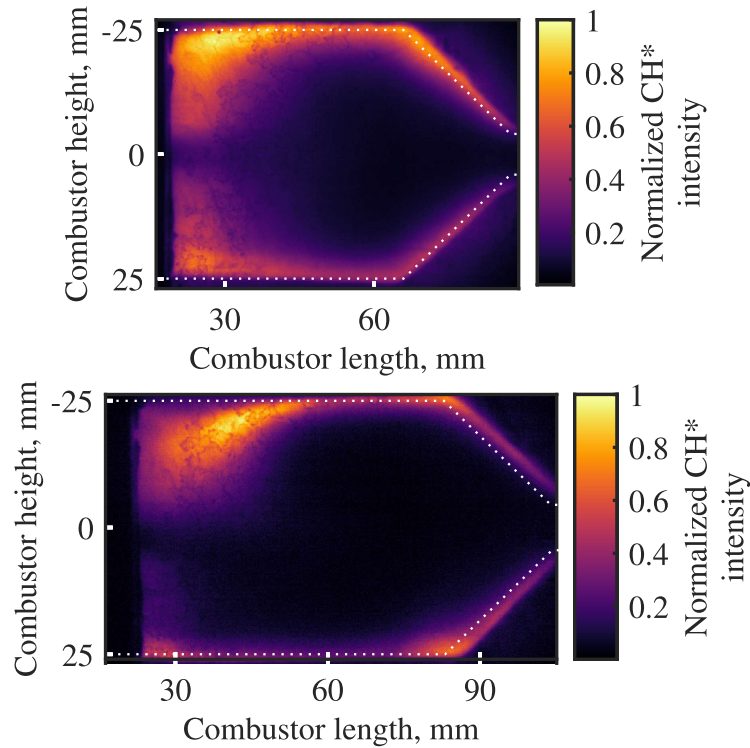


Figure 5.11: Geometry A, test 15 (top), and geometry B, test 16 (bottom) time-averaged CH^* chemiluminescence from flameholding cavity, flow from left to right.

The regression rate is determined at discrete points on the fuel grain by measuring the difference between fuel grain locations at incremental time steps in the real-time videos. The discrete points allow for the representation of the fuel grain shape at 1/3 second increments. One profile for geometry A and one profile for geometry B are in Fig. 5.12. There is a significant gap between the first measured time step of regression and the original geometry of the fuel grain. The gap is a result of melting and shearing of the PMMA during the 6 seconds of pre-flow before ignition occurs. The time-averaged regression rate is plotted over the reconstructed fuel grain profiles. The experimental uncertainty, as calculated in

Appendix A, is represented by the error bars at each location the regression is measured. The experimental uncertainty for the manually measured regression rate is acceptable at ± 0.075 mm/s, which is less than the statistically averaged standard deviations, ± 0.127 mm/s, as plotted in Fig. 5.13 and Fig. 5.14. The regression is only measured at the locations with error bars; however, to provide an idea of the shape of the regressing fuel grain, the points from each time step are connected by straight lines.

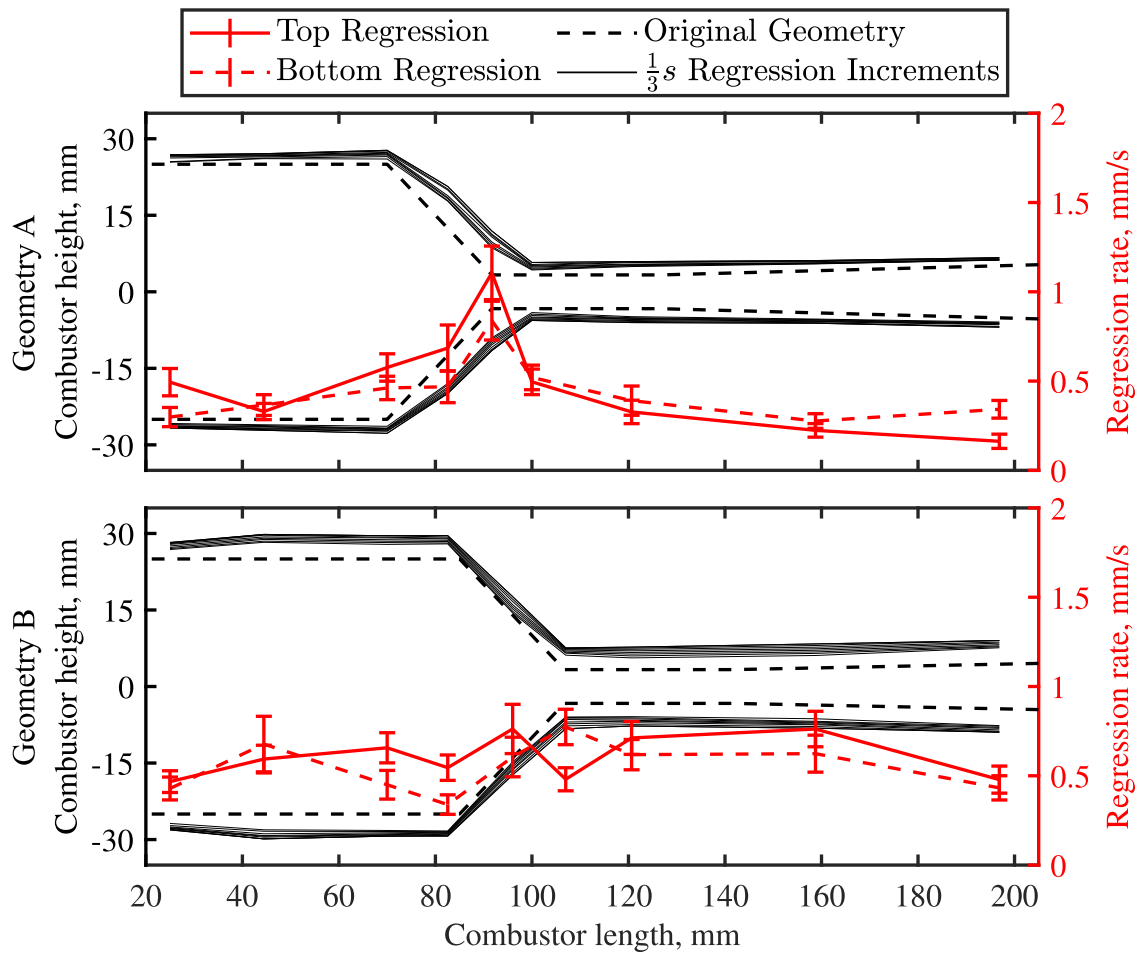


Figure 5.12: Regression Profiles and time averaged regression rates for fuel grain geometry A, test 3 (top), and geometry B, test 2 (bottom). The error bars represent the experimental uncertainty from data collection methods.

The time averaged regression rates of the top and bottom of the fuel grain are also presented in Fig. 5.12. The pattern in geometry A agrees with the patterns in the enclosed fuel grain

regression from Fig. 4.9 and other studies [6, 7]. The highest regression rate measured is in the angled converging section and the beginning of the constant area section. Geometry B, however, maintains a nearly constant time-averaged regression rate across the entire length of the fuel grain. The single large recirculation zone that results from the unstable, high pressure oscillations does not take full advantage of the geometry and does not receive fuel from the same locations.

The statistically averaged regression rate of the top and bottom of each fuel grain geometry is plotted in Fig. 5.13 and Fig. 5.14. The error bars on the plots are the standard deviation across the 6 examined firings of each fuel grain geometry. The top sides of both fuel grains results in a higher standard deviation than the bottoms. Although no exact cause can be determined for this, the pressure ports in the top fuel grain can cause unpredictable and irregular flow patterns. Post fire observations show that the 3D printed port holes widen significantly during combustion and play a role in the variable regression rates.

The magnitudes of the regression rate is similar between the two geometries, with the exception of the angled end of the flameholding cavity. In fuel grain geometry A, the regression rate has a sharp spike at this location in both the top and bottom. Fuel grain geometry B, however, has a more gradual increase from its lowest regression at the upstream end of the flameholding cavity to its maximum at the downstream end of the flameholding cavity. This gradual change is more noticeable in the top of the fuel grain and parallels the observations from the chemiluminescence imaging in Fig. 5.10, where a higher intensity of CH^* radicals represent more heat release from combustion occurring in this region.

An advantage of collecting the instantaneous regression rate during an experiment comes when investigating how the regression rate changes as the fuel geometry changes. In this case, the regression rate is not explicitly instantaneous, but the 1/3 second increments provide an idea of how the regression rate changes over time. Fuel grain geometry A and geometry B

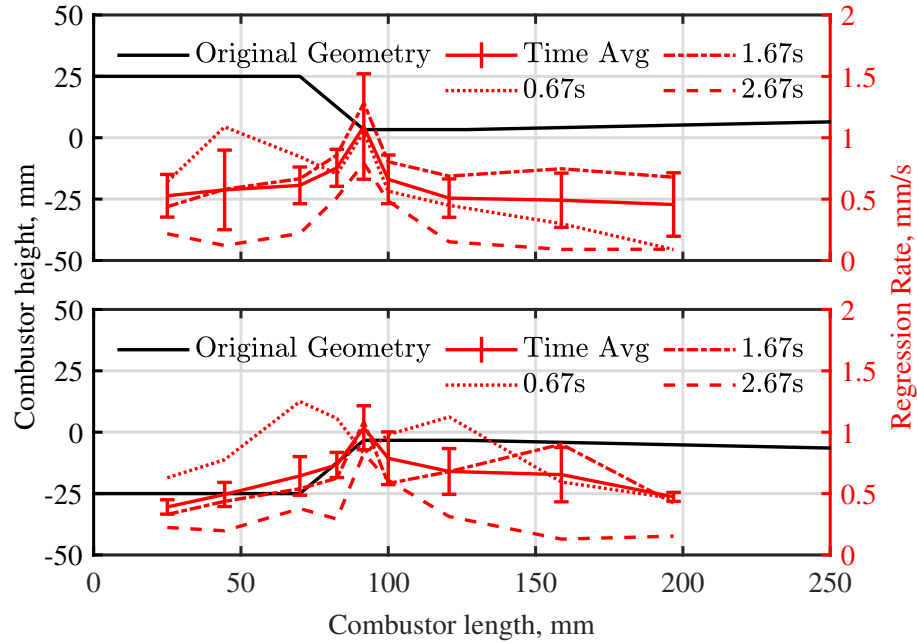


Figure 5.13: Statistically averaged regression rates for geometry A.

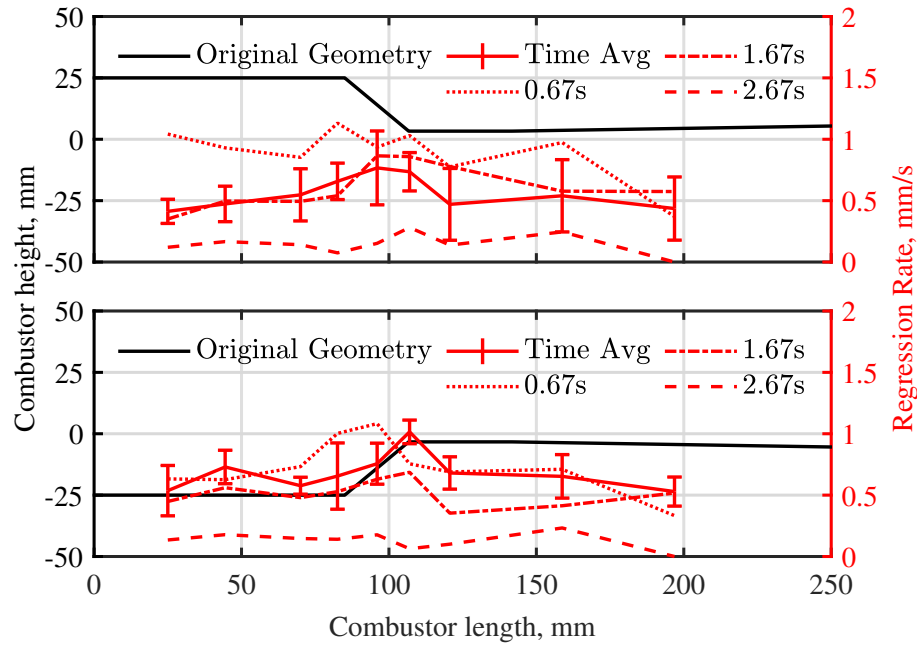


Figure 5.14: Statistically averaged regression rates for geometry B.

regression rates at specific time intervals are plotted in Fig. 5.13 and Fig. 5.14 respectively. The expectation based on the enclosed fuel grain regression versus geometry plot in Fig. 4.11 is a larger cross-sectional area in the flameholding cavity and constant area section will produce lower regression rates. This translates to as a fuel grain consumes more fuel, the regression rate will decrease. The decreasing pattern is clear in the flameholding cavity and some of the constant area section. However, it is not observed in the downstream half of the fuel grain through the diverging section. Based on the chemiluminescence data in Fig. 5.10, there is a low intensity of CH^* radicals present downstream of the constant area section. Fuel is not combusting as effectively in this region due to a lower residence time, and it is instead likely subject to melting and shearing from the hot gasses combusting in the flameholding cavity.

Figure 5.15 summarizes the combustion process in a SFSJ with a small L/D of the flameholding cavity and Fig. 5.16 summarizes the combustion process in a SFSJ with a large L/D of the flameholding cavity as determined through analysis of the optical SFSJ experiment.

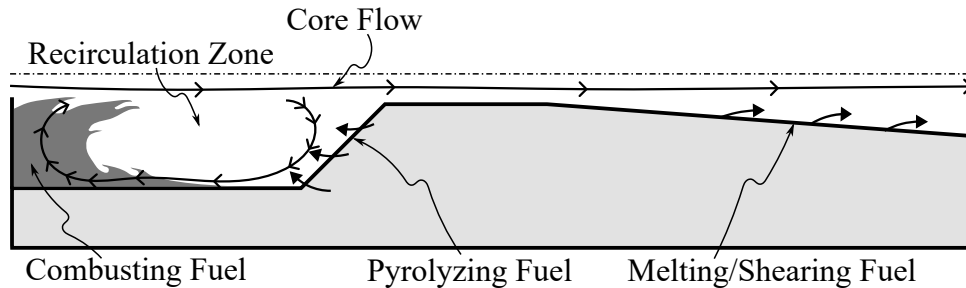


Figure 5.15: Summarized process of combusting fuel in a SFSJ with a small L/D flameholding cavity.

The flameholding cavity creates a recirculation zone to increase the residence time of air in the combustor. As the flow is moving away from the core into the cavity, it pyrolyzes fuel from the converging angle of the flameholding cavity, breaking the long polymer chains into smaller molecules. The smaller molecules of fuel are carried in the upstream direction across

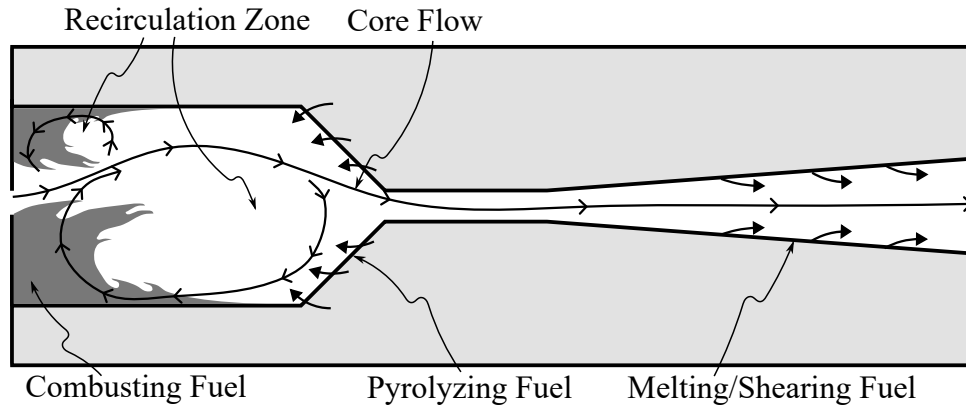


Figure 5.16: Summarized process of combusting fuel in a SFSJ with a large L/D flameholding cavity.

the bottom of the flameholding cavity where they are mixed with the air and combusted as the recirculation pushes the higher temperature flow up and towards the core flow near the inlet. As the high temperature flow combines with the core flow, it is expelled through the constant area section and diverging section. A normal shock is occasionally present in the constant area section that shows the flow is supersonic upstream of this location. Without any recirculation to increase the residence time, fuel in the diverging section is melted and sheared as the core flow moves across the surface.

Chapter 6

Conclusions

The research conducted in this thesis includes major accomplishments that advance the field of supersonic solid fuel combustion. The enclosed, rectangular cross-section combustor expands the available literature on SFSJs to new internal geometries, and lower temperatures than examined before. The development of the first optically accessible, 2D SFSJ combustor provides opportunities for advanced analysis that deepen the understanding of the mechanisms defining SFSJ combustion.

The experiments conducted in an enclosed, rectangular cross-section SFSJ provide analysis on the ignition characteristics and time-averaged regression rate with varying geometries and varying inlet conditions. Evidence is presented that more ideal geometric conditions are dependent on a larger flameholding cavity with respect to both the inlet size and the constant area size. However, the size of the flameholding cavity is limited by the overall size of the combustor. Additionally, a larger cavity reduces the amount of fuel that the combustor can consume, reducing the total possible combustion duration.

Sustained combustion is credited to a larger flameholding cavity providing a more suitable environment for the recirculation of the flow over the surface. The recirculation pyrolyzes the fuel from the walls of the fuel grain to increase the enthalpy of the flow, which is then carried into the core flow and expelled through the fuel grain. The geometries which show sustained ignition also yield higher time-averaged regression rates. The regression and consumption of fuel is related to the size of the recirculation zone, as most of the regression occurs in

the flameholding cavity. Particularly, the highest regression rate is observed in the corner at the downstream end of the flameholding cavity. If the fuel grain geometry has a larger constant area section, lower pressures and regression rates are observed throughout the entire fuel grain on the effect of limiting the thermal choking. Decreasing the time of combustion demonstrates an early favoring of fuel regression in the flameholding cavity, again signalling the dominance of the flameholding cavity in determining if the fuel grain sustains supersonic combustion.

The enclosed SFSJ testing also features experiments investigating the effect of varying inlet temperature. Decreasing the inlet temperature increases the time to ignition and decreases the pressure at ignition and regression rates. A minimum threshold for combustion is determined to be 754 K for this specific configuration. The varying temperature experiment demonstrates the lowest temperature conditions ever applied to a direct connect SFSJ in published literature.

The development of an optically accessible SFSJ provides opportunities at the forefront of studying supersonic solid fuel combustion. Shadowgraph imaging techniques are utilized to explore the flow fields presented through the unique geometry of a SFSJ. These techniques show flow biasing as an effect of pressure fluctuations in the flameholding cavity. They also provide confirmation of a supersonic flow through the fuel grain by the presence of a normal shock. CH^* chemiluminescence imaging highlights the primary regions of combustion along the walls of the fuel grain. Primarily, combustion is observed at the wall in the upstream area of the flameholding cavity, explaining the importance of the recirculation zone and increasing residence time to sustain combustion. Incremental time-averaged regression rates are measured to provide insight on the effect of a varying fuel geometry on the combustion process. As the fuel is consumed, the flow cross-sectional area increases, decreasing the regression rate. This phenomena, however, is found to not apply in the diverging section

which mostly loses fuel by melting and shearing.

The SFSJ is still relatively untouched in the larger field of propulsion, leaving many opportunities for future work. Of course, new geometries can be created and tested to create a complete flammability map for the optical SFSJ. Looking closer at the flow fields could provide an analytical method for prescribing the limits of a particular combustor. Additional optical based methods include Particle Image Velocimetry, Tunable Diode Laser Absorption Spectroscopy, and more detailed views of the combusting fuel through endoscopic and microscopic lenses. Related to the experiments conducted, there is still uncertainty of the true reason of the flow biasing in the optical SFSJ. Insight of the pressure oscillation in the flameholding cavity could be discovered using powerful post-processing techniques, such as Dynamic Mode Decomposition or Spectral Proper Orthogonal Decomposition.

Bibliography

- [1] S. N. B. Murthy and E. T. Curran, *High-Speed Flight Propulsion Systems*. No. 137 in Progress in Astronautics and Aeronautics, Washington, D. C: American institute of aeronautics and astronautics, 1991.
- [2] W. H. Heiser and D. T. Pratt, *Hypersonic Airbreathing Propulsion*. AIAA Education Series, Washington, D.C: American Institute of Aeronautics and Astronautics, 1994.
- [3] A. Ben-Yakar and R. K. Hanson, “Cavity Flame-Holders for Ignition and Flame Stabilization in Scramjets: An Overview,” *Journal of Propulsion and Power*, vol. 17, pp. 869–877, July 2001.
- [4] D. Gallegos, H. Pace, C. Arnold, L. Massa, and G. Young, “Regression and Flame Structure in Cavity Flameholding Solid-Fuel Ramjet Fuel Grains,” *Journal of Propulsion and Power*, pp. 1–11, May 2023.
- [5] W. Angus, “An Investigation into the Performance Characteristics of a Solid Fuel SCRAMJET Propulsion Device,” Master’s thesis, Naval Postgraduate School, Dec. 1991.
- [6] A. Ben-Yakar, B. Natan, and A. Gany, “Investigation of a Solid Fuel Scramjet Combustor,” *Journal of Propulsion and Power*, vol. 14, pp. 447–455, July 1998.
- [7] A. Cohen-Zur and B. Natan, “Experimental Investigation of a Supersonic Combustion Solid Fuel Ramjet,” *Journal of Propulsion and Power*, vol. 14, pp. 880–889, Nov. 1998.
- [8] A. Ben-Yakar and R. Hanson, “Experimental investigation of flame-holding capabil-

- ity of hydrogen transverse jet in supersonic cross-flow,” *Symposium (International) on Combustion*, vol. 27, no. 2, pp. 2173–2180, 1998.
- [9] P. Hill and C. Peterson, *Mechanics and Thermodynamics of Propulsion*. Pearson, 2 ed., 1992.
- [10] M. J. Moran, *Fundamentals of Engineering Thermodynamics, 9th Australia and New Zealand Edition*. New York: John Wiley & Sons, Incorporated, 2019. OCLC: 1240581558.
- [11] E. W. Constant, *The Origins of the Turbojet Revolution*. No. 5 in Johns Hopkins Studies in the History of Technology New Series, Baltimore: Johns Hopkins Univ. Press, 1980.
- [12] W. J. Boyne, D. S. Lopez, A. Franz, and N. A. a. S. Museum, eds., *The Jet Age: Forty Years of Jet Aviation*. Washington: National Air and Space Museum, Smithsonian Institution : Distributed by Smithsonian Institution Press, 1979.
- [13] S. A. Brandt, *Introduction to Aeronautics: a Design Perspective*. AIAA education series, Reston, Virginia: American Institute of Aeronautics and Astronautics, Inc, third edition ed., 2015.
- [14] *The Pocket Ramjet Reader*. Hartford, CT: Chemical Systems Division United Technologies, 1978.
- [15] W. H. Avery, “Twenty-Five Years of Ramjet Development,” *Journal of Jet Propulsion*, vol. 25, pp. 604–614, Nov. 1955.
- [16] R. S. Fry, “A Century of Ramjet Propulsion Technology Evolution,” *Journal of Propulsion and Power*, vol. 20, pp. 27–58, Jan. 2004.

- [17] C. Segal, *The Scramjet Engine: Processes and Characteristics*. No. 25 in Cambridge aerospace series, Cambridge ; New York: Cambridge University Press, 2009. OCLC: ocn277118461.
- [18] C. Peebles, *Road to Mach 10: Lessons Learned From the X-43A Flight Research Program*. Reston, Va: American Institute of Aeronautics and Astronautics, 2008.
- [19] J. Connors and N. Allen, *The Engines of Pratt & Whitney: A Technical History*. Reston, VA: American Institute of Aeronautics and Astronautics, 2010. OCLC: ocn435918238.
- [20] S. Murthy and E. Curran, *Scramjet Propulsion*. Progress in Astronautics and Aeronautics, AIAA, 2001.
- [21] L. D. Luca, *Chemical Rocket Propulsion: A Comprehensive Survey of Energetic Materials*. New York, NY: Springer Berlin Heidelberg, 2016.
- [22] J. P. Agrawal, *High Energy Materials: Propellants, Explosives and Pyrotechnics*. Weinheim: Wiley-VCH, 2010.
- [23] M. J. Chiaverini and K. K. Kuo, eds., *Fundamentals of Hybrid Rocket Combustion and Propulsion*. No. v. 218 in Progress in Astronautics and Aeronautics, Reston, Va: American Institute of Aeronautics and Astronautics, 2007. OCLC: ocn123961364.
- [24] A. Gany, “Accomplishments and challenges in solid fuel ramjets and scramjets,” *International Journal of Energetic Materials and Chemical Propulsion*, vol. 8, no. 5, pp. 421–446, 2009.
- [25] J. Tirpak, “U.S.-Norway Solid-Fuel Ramjet Passes Tests for Speed, Range,” *Air & Space Forces Magazine*, Oct. 2022.

- [26] M. Witt, “Investigation into the feasibility of using solid fuel ramjets for high supersonic/low hypersonic tactical missiles,” Master’s thesis, Naval Postgraduate School, June 1989.
- [27] D. P. Mishra, *Fundamentals of Rocket Propulsion*. Boca Raton: CRC Press, Taylor & Francis Group, CRC Press is an imprint of the Taylor & Francis Group, an informa business, 2017.
- [28] D. Pelosi-Pinhas and A. Gany, “Bypass-Regulated Solid Fuel Ramjet Combustor in Variable Flight Conditions,” *Journal of Propulsion and Power*, vol. 19, pp. 73–80, Jan. 2003.
- [29] J. V. Evans, W. C. B. Senior, R. M. Gejji, and C. D. Slabaugh, “Performance of a Solid-Fuel Ramjet Combustor with Bypass Air Addition,” *Journal of Propulsion and Power*, pp. 1–9, Oct. 2022.
- [30] D. Altman, “Hybrid rocket development history,” in *27th Joint Propulsion Conference*, (Sacramento,CA,U.S.A.), American Institute of Aeronautics and Astronautics, June 1991.
- [31] K. Gańczyk-Specjalska and P. Magnuszewska, “An analysis of the mechanical properties of HTPB-propellants using DMA,” *Materiały Wysokoenergetyczne / High Energy Materials*, pp. 81–91, Dec. 2020.
- [32] J. Rabinovitch, E. T. Jens, A. C. Karp, B. Nakazono, A. Conte, and D. A. Vaughan, “Characterization of PolyMethylMethAcrylate as a Fuel for Hybrid Rocket Motors,” in *2018 Joint Propulsion Conference*, (Cincinnati, Ohio), American Institute of Aeronautics and Astronautics, July 2018.
- [33] F. S. Mechentel, B. R. Hord, and B. J. Cantwell, “Optically Resolved Fuel Regression

- of a Clear Polymethylmethacrylate Hybrid Rocket Motor,” *Journal of Propulsion and Power*, vol. 36, pp. 763–772, Sept. 2020.
- [34] T. Connell, G. Young, K. Beckett, and D. R. Gonzalez, “Enhanced solid fuel regression in a hybrid rocket employing additively manufactured fuels exhibiting novel grain port geometries,” in *AIAA Scitech 2019 Forum*, (San Diego, California), American Institute of Aeronautics and Astronautics, Jan. 2019.
- [35] G. Young, T. L. Connell, K. Fennell, S. Possehl, and M. Baier, “Examining Port Geometry/Solid Loading for Additively Manufactured Fuels in Hybrid Rockets,” *Journal of Propulsion and Power*, vol. 37, pp. 305–313, Mar. 2021.
- [36] G. Lengelle, “Thermal degradation kinetics and surface pyrolysis of vinyl polymers,” *AIAA Journal*, vol. 8, pp. 1989–1996, Nov. 1970.
- [37] S. Madorsky, *Thermal Degradation of Organic Polymers*, vol. 7 of *Polymer Reviews*. Interscience Publishers, 1964.
- [38] T. Houser, “Final Report: Research in Hybrid Combustion,” Tech. Rep. AD No. 404883, Rocketdyne, May 1963.
- [39] G. Marxman and M. Gilbept, “Turbulent boundary layer combustion in the hybrid rocket,” in *Symposium (International) on Combustion*, vol. 9, pp. 371–383, 1963.
- [40] G. A. Marxman, C. E. Wooldridge, and R. J. Muzzy, “FUNDAMENTALS OF HYBRID BOUNDARY-LAYER COMBUSTION,”
- [41] G. Risha, G. Harting, K. Kuo, A. Peretz, D. Koch, H. Jones, and J. Arves, “Pyrolysis and combustion of solid fuels in various oxidizing environments,” in *34th AIAA/ASME/SAE/ASEE Joint Propulsion Conference and Exhibit*, (Cleveland, OH, U.S.A.), American Institute of Aeronautics and Astronautics, July 1998.

- [42] S. C. Shark, C. R. Zaseck, T. L. Pourpoint, and S. F. Son, “Solid-fuel regression rates and flame characteristics in an Opposed Flow Burner,” *Journal of Propulsion and Power*, vol. 30, pp. 1675–1682, Nov. 2014.
- [43] G. Young, S. Hromisin, S. Loeffler, and T. L. Connell, “Effect of Oxidizer Type on Solid Fuel Combustion,” *Journal of Propulsion and Power*, vol. 36, pp. 248–255, Mar. 2020.
- [44] H. Pace, A. Jessup, D. Gallegos, G. Young, and L. Massa, “Counterflow Combustion and Regression of PMMA Model Fuel,” in *AIAA AVIATION 2022 Forum*, (Chicago, IL & Virtual), American Institute of Aeronautics and Astronautics, June 2022.
- [45] R. Muzzy, “Applied hybrid combustion theory,” in *8th Joint Propulsion Specialist Conference*, (New Orleans, LA, U.S.A.), American Institute of Aeronautics and Astronautics, Nov. 1972.
- [46] F. S. Billig, “Supersonic combustion of storable liquid fuels in Mach 3.0 to 5.0 air streams,” *Symposium (International) on Combustion*, vol. 10, pp. 1167–1178, Jan. 1965.
- [47] P. W. Huber, C. J. Schexnayder, and C. R. McClinton, “Criteria for self-ignition of supersonic hydrogen-air mixtures,” Tech. Rep. NASA-TP-1457, NASA, 1979.
- [48] D. W. Riggins, C. R. McClinton, R. C. Rogers, and R. D. Bittner, “Investigation of scramjet injection strategies for high Mach number flows,” *Journal of Propulsion and Power*, vol. 11, pp. 409–418, May 1995.
- [49] J. Tishkoff, J. Drummond, T. Edwards, A. Nejad, J. Tishkoff, J. Drummond, T. Edwards, and A. Nejad, “Future directions of supersonic combustion research - Air Force/-NASA workshop on supersonic combustion,” in *35th Aerospace Sciences Meeting and Exhibit*, (Reno, NV, U.S.A.), American Institute of Aeronautics and Astronautics, Jan. 1997.

- [50] P. Ortwerth, A. Mathur, V. Vinogradov, V. Grin, M. Goldfeld, and A. Starov, “Experimental and numerical investigation of hydrogen and ethylene combustion in a Mach 3-5 channel with a single injector,” in *32nd Joint Propulsion Conference and Exhibit*, (Lake Buena Vista, FL, U.S.A.), American Institute of Aeronautics and Astronautics, July 1996.
- [51] M. G. Owens, S. Tehranian, C. Segal, and V. A. Vinogradov, “Flame-holding configurations for kerosene combustion in a Mach 1.8 airflow,” *Journal of Propulsion and Power*, vol. 14, pp. 456–461, July 1998.
- [52] V. A. Vinogradov, S. A. Kobigsky, and M. D. Petrov, “Experimental investigation of kerosene fuel combustion in supersonic flow,” *Journal of Propulsion and Power*, vol. 11, pp. 130–134, Jan. 1995.
- [53] I. Feldman and A. Gany, “Parametric investigation of supersonic combustion of solid fuels,” tech. rep., Technion - Israel Institute of Technology, 2002.
- [54] V. Chernov, “Experimental Investigation of a Solid Fuel Scramjet Using an Arc Heater,” *Journal of Propulsion and Power*, vol. 35, pp. 879–882, July 2019.
- [55] K. Krishnamurty, “Acoustic Radiation from Two-dimensional Rectangular Cutouts in Aerodynamic Surfaces,” Tech. Rep. NACA-TN-3487, California Institute of Technology, 1955.
- [56] H. Plumblee, J. Gibson, and L. Lassiter, “A theoretical and experimental investigation of the acoustic response of cavities in an aerodynamic flow,” Tech. Rep. AD277803, Wright-Patterson Air Force Base, Arlington, VA, 1962.
- [57] H. Heller and D. Bliss, “The Physical Mechanism of Flow-Induced Pressure Fluctuations

- in Cavities and Concepts for their Suppression,” in *AIAA 2nd Aeroacoustics Conference*, (Hampton, Virginia), AIAA, Mar. 1975.
- [58] X. Zhang and J. A. Edwards, “An investigation of supersonic oscillatory cavity flows driven by thick shear layers,” *The Aeronautical Journal*, vol. 94, pp. 355–364, Dec. 1990.
- [59] R. L. Sarno and M. E. Franke, “Suppression of flow-induced pressure oscillations in cavities,” *Journal of Aircraft*, vol. 31, pp. 90–96, Jan. 1994.
- [60] X. Zhang, A. Rona, and J. A. Edwards, “The effect of trailing edge geometry on cavity flow oscillation driven by a supersonic shear layer,” *The Aeronautical Journal*, vol. 102, pp. 129–136, Mar. 1998.
- [61] M. R. Gruber, R. A. Baurle, T. Mathur, and K.-Y. Hsu, “Fundamental Studies of Cavity-Based Flameholder Concepts for Supersonic Combustors,” *Journal of Propulsion and Power*, vol. 17, pp. 146–153, Jan. 2001.
- [62] S. Nakaya, H. Yamana, and M. Tsue, “Experimental investigation of ethylene/air combustion instability in a model scramjet combustor using image-based methods,” *Proceedings of the Combustion Institute*, vol. 38, no. 3, pp. 3869–3880, 2021.
- [63] T. M. Ombrello, C. D. Carter, C.-J. Tam, and K.-Y. Hsu, “Cavity ignition in supersonic flow by spark discharge and pulse detonation,” *Proceedings of the Combustion Institute*, vol. 35, no. 2, pp. 2101–2108, 2015.
- [64] D. Cuppoletti, T. Ombrello, C. Carter, S. Hammack, and J. Lefkowitz, “Ignition dynamics of a pulse detonation igniter in a supersonic cavity flameholder,” *Combustion and Flame*, vol. 215, pp. 376–388, May 2020.
- [65] N. Kato and S.-k. Im, “Flame dynamics under various backpressures in a model scramjet

- with and without a cavity flameholder,” *Proceedings of the Combustion Institute*, vol. 38, no. 3, pp. 3861–3868, 2021.
- [66] K. M. Krall and E. M. Sparrow, “Turbulent Heat Transfer in the Separated, Reattached, and Redevelopment Regions of a Circular Tube,” *Journal of Heat Transfer*, vol. 88, pp. 131–136, Feb. 1966.
- [67] P. Buckley, R. Craig, and B. Obleski, “The effect of swirl on a ramjet dump combustor,” in *4th International Symposium on Air Breathing Engines*, (Orlando, FL, U.S.A.), American Institute of Aeronautics and Astronautics, Apr. 1979.
- [68] O. Musa, C. Xiong, and Z. Changsheng, “Experimental and numerical investigation on the ignition and combustion stability in solid fuel ramjet with swirling flow,” *Acta Astronautica*, vol. 137, pp. 157–167, Aug. 2017.
- [69] O. Musa, L. Weixuan, C. Xiong, G. Lunkun, and L. Wenhe, “Experimental investigation on the effect of swirling flow on combustion characteristics and performance of solid fuel ramjet,” *Acta Astronautica*, vol. 148, pp. 163–174, July 2018.
- [70] C. Mady, P. Hickey, and D. Netzer, “Combustion Behavior of Solid-Fuel Ramjets,” *Journal of Spacecraft and Rockets*, vol. 15, pp. 131–132, May 1978.
- [71] G. Schulte, R. Pein, and A. Hög, “Temperature and concentration measurements in a solid fuel ramjet combustion chamber,” *Journal of Propulsion and Power*, vol. 3, pp. 114–120, Mar. 1987.
- [72] A. Netzer and A. Gany, “Burning and flameholding characteristics of a miniature solid fuel ramjet combustor,” *Journal of Propulsion and Power*, vol. 7, pp. 357–363, May 1991.

- [73] G. Schulte, “Fuel regression and flame stabilization studies of solid-fuel ramjets,” *Journal of Propulsion and Power*, vol. 2, pp. 301–304, July 1986.
- [74] R. Zvuloni, A. Gany, and Y. Levy, “Geometric effects on the combustion in solid fuel ramjets,” *Journal of Propulsion and Power*, vol. 5, pp. 32–37, Jan. 1989.
- [75] R. Zvuloni, Y. Levy, and A. Gany, “Investigation of a small solid fuel ramjet combustor,” *Journal of Propulsion and Power*, vol. 5, pp. 269–275, May 1989.
- [76] R. C. Wooldridge and D. W. Netzer, “Ignition and flammability characteristics of solid fuel ramjets,” *Journal of Propulsion and Power*, vol. 7, pp. 846–848, Sept. 1991.
- [77] W. C. B. Senior, R. M. Gejji, and C. D. Slabaugh, “Flame Dynamics in an Optically Accessible Solid Fuel Ramjet Combustor,” *Journal of Propulsion and Power*, pp. 1–10, Apr. 2023.
- [78] L. D. Boaz, “Internal ballistics of solid fuel ramjets,”
- [79] S. Saraf and A. Gany, “TESTING METALLIZED SOLID FUEL SCRAMJET COMBUSTOR,” pp. 1176–1187, AIAA, 2007.
- [80] T. A. Jarymowycz, V. Yang, and K. K. Kuo, “Numerical study of solid-fuel combustion under supersonic crossflows,” *Journal of Propulsion and Power*, vol. 8, pp. 346–353, Mar. 1992.
- [81] D. Simone and C. Bruno, “Preliminary Investigation on Lithium Hydride as Fuel for Solid-Fueled Scramjet Engines,” *Journal of Propulsion and Power*, vol. 25, pp. 875–884, July 2009.
- [82] X. Pei, Z. Wu, Z. Wei, and J. Liu, “Numerical Investigation on Internal Regressing Shapes of Solid-Fuel Scramjet Combustor,” *Journal of Propulsion and Power*, vol. 29, pp. 1041–1051, Sept. 2013.

- [83] L. Wang, Z. Wu, H. Chi, C. Liu, H. Tao, and Q. Wang, “Numerical and experimental study on the solid-fuel scramjet combustor,” *Journal of Propulsion and Power*, vol. 31, pp. 685–693, Mar. 2015.
- [84] H.-w. Chi, Z.-j. Wei, L.-h. Wang, B. Li, and Z.-w. Wu, “Numerical Investigation of Self-Ignition Characteristics of Solid-Fuel Scramjet Combustor,” *Journal of Propulsion and Power*, vol. 31, pp. 1019–1032, July 2015.
- [85] X. Zhao, Z. Xia, L. Ma, C. Li, C. Fang, B. Natan, and A. Gany, “Research progress on solid-fueled Scramjet,” *Chinese Journal of Aeronautics*, vol. 35, pp. 398–415, Jan. 2022.
- [86] E. Schlussel, D. Gallegos, and G. Young, “Supersonic Combustion of Solid Fuels,” in *AIAA AVIATION 2023 Forum*, June 2023.
- [87] W. Angus, M. A. Witt, D. Laredo, and D. Netzer, “Solid Fuel Supersonic Combustion,” *Recherche aerospatiale*, no. 6, pp. 1–8, 1993.
- [88] S. Kline and F. McClintock, “Describing Uncertainties in Single-Sample Experiments,” *Mechanical Engineering*, no. 75, pp. 3–8, 1953.
- [89] J. D. Anderson, *Modern Compressible Flow: With Historical Perspective*. McGraw-Hill series in aeronautical and aerospace engineering, Boston: McGraw-Hill, 3rd ed ed., 2003.

Appendix A

Uncertainty Analysis

The uncertainty analysis for the regression rate measurements is conducted using the Kline and McClintock method of uncertainty in single sample experiments [88]. The method determines uncertainty by considering R as a function of n independent variables. For small variations in the variables (v) the propagation of uncertainty (σ) is determined using Eqn. [A.1](#).

$$\sigma_R = \pm \sqrt{\left(\sigma_1 \frac{\partial R}{\partial v_1}\right)^2 + \left(\sigma_2 \frac{\partial R}{\partial v_2}\right)^2 + \dots + \left(\sigma_n \frac{\partial R}{\partial v_n}\right)^2} \quad (\text{A.1})$$

In the case of measuring the uncertainty of the regression rates, as measured in Fig. [5.12](#), the regression rate in Eqn. [A.2](#) has time (t) and location (y) as independent variables.

$$\dot{r} = \frac{\Delta y}{\Delta t} \quad (\text{A.2})$$

The uncertainty in the time measurement is limited by the frame rate of the recording camera, or 30 frames per second. The uncertainty with respect to time $\pm 1/30$ seconds. The uncertainty of the location of the fuel grain edge is determined by the standard deviation of multiple iterations of measuring the fuel grain edge using the MATLAB program. The resulting uncertainty for the regression rate is solved by Eqn. [A.3](#).

$$\sigma_{\dot{r}} = \pm \sqrt{\left(\sigma_t \frac{\partial \dot{r}}{\partial t}\right)^2 + \left(\sigma_2 \frac{\partial \dot{r}}{\partial y}\right)^2} \quad (\text{A.3})$$

Conducting this analysis for the regressing edge of the fuel grains provides an average uncertainty of ± 0.075 mm/s.

Appendix B

Matlab Codes

B.1 Edge Detecting Codes for Enclosed, Rectangular Cross-Section SFSJ

B.1.1 Fuel Grain Length Edge Detection

```
1 %% Edge detection for cut SFSJ rectangular cross-section fuel grains
2 %% Ethan J. Schlussel
3
4 clc , clear
5 close all
6 clear all
7
8 %%%%%%%%%%%%%%%%%%%%%%%%%%%%%%%%%%%%%%%%%%%%%%%%%%%%%%%%%%%%%%%%%%%%%%%%%%
9 %% Input Values for test
10 Fuel_Grain = 11;    % Fuel Grain Number
11 Side = 'B';        % Side A or B
12 Temp = 650;        % Tested heater temperature
13 %%%%%%%%%%%%%%%%%%%%%%%%%%%%%%%%%%%%%%%%%%%%%%%%%%%%%%%%%%%%%%%%%%%%%%%%%%
14
15 %% Edge Detection Script
16
17 % Pull data from spreadsheet with original geometries based on input
```

```

18 total = 15; % Total number of tested fuel grains
19 opts.DataRange = '2:15'; opts.SelectedVariableRange = 2:10;
20 IgnitionData = readmatrix("Test_Summary.xlsx"); % Pulls data from spreadsheet
21 for j = 1:total % Loop to pull desire test based on inputs
22     if IgnitionData(j,2) == Fuel_Grain
23         if IgnitionData(j,7) == Temp
24             Row = j;
25             break
26         else
27             end
28     elseif j == total
29         disp('INPUT ERROR')
30     else
31         end
32 end
33
34 % Assign values from spreadsheet to Matlab Variables
35 Day = IgnitionData(Row, 4); Month = IgnitionData(Row, 3);
36 Year = IgnitionData(Row, 5); Testnum = IgnitionData(Row, 6);
37 Mass_i = IgnitionData(Row, 8); Mass_f = IgnitionData(Row, 9);
38 Time = IgnitionData(Row, 10);
39 % Defines the file to pull based on spreadsheet information
40 Folder = "Cut_Photos\";
41 test_name = sprintf("FG%d, %02d/%02d/%d, Test %d, T = %dC, %s", Fuel_Grain,
    Month, Day, Year, Testnum, Temp, Side);
42 file = sprintf("%s%02d_%02d_%d_Test_%d_%s_Paint.tif", Folder, Month, Day, Year,
    Testnum, Side);
43
44 cal_factor = 2.7523e-4; % Preset calibration value, m/px
45
46 threshold = 0.35; % Edge detect threshold value

```

```

47
48 % Original Grain dimensions , based on spreadsheet
49
50 AAA = FG(Fuel_Grain);
51 h_fl = AAA(1)/1000; h_const = AAA(2)/1000;
52 L_fl = AAA(3)/1000; L_const = AAA(4)/1000;
53
54 L_t = 0.2667; % Overall grain length , m
55
56 a_conv = 45 * (pi/180); % Converging section angle , rad
57 a_div = 3 * (pi/180); % Diverging section angle , rad
58
59 %%%%%%%%%%%%%%%%%%%%%%%%%%%%%%%%%%%%%%%%%%%%%%%%%%%%%%%%%%%%%%%%%%%%%%%%%%
60 %% Calibration factor
61 cal_distance = 0.3; % Distance between points selected in calibration image , m
62 f1 = figure('Name', 'Select calibration distance 30 cm');
63 imshow(imread(file))
64 [x_cal , y_cal] = ginput(2);
65
66 cal_factor = cal_distance / (x_cal(2) - x_cal(1));
67
68 %%%%%%%%%%%%%%%%%%%%%%%%%%%%%%%%%%%%%%%%%%%%%%%%%%%%%%%%%%%%%%%%%%%%%%%%%%
69
70 %% Main script
71 fullImage = imread(file);
72 f1 = figure('Name', 'Crop image to fuel grain , include outer surface');
73 croppedImage = imcrop(fullImage);
74 close(f1)
75
76 f1 = figure();
77 imshow(croppedImage)

```



```

78 set(f1, 'Name', ...
79     'Select four points to define grain centerline – clockwise from upper
    right')
80 [x_cen, y_cen] = ginput(4);
81
82 left_mid = [(x_cen(3) + x_cen(4))/2, (y_cen(3) + y_cen(4))/2];
83 right_mid = [(x_cen(1) + x_cen(2))/2, (y_cen(1) + y_cen(2))/2];
84
85 centerline_slope = (floor(right_mid(2)) - ...
86     floor(left_mid(2)))/(floor(right_mid(1) - left_mid(1)));
87
88 centerline_x = floor(left_mid(1)):1:floor(right_mid(1));
89 centerline_y = centerline_slope.*centerline_x + left_mid(2);
90
91 hold on
92 plot(centerline_x, centerline_y, "r")
93
94 edgeImage = edge(rgb2gray(croppedImage), 'Canny', threshold');
95 [edgeM, edgeN] = size(edgeImage);
96
97 region_mask_continue = "Y";
98
99 while region_mask_continue == "Y"
100     f2 = figure('Name', ...
101         'Mask false edges inside fuel grain. Double click inside closed
        polygon to proceed. ');
102     mask = roipoly(edgeImage);
103     edgeImage = edgeImage.*~mask;
104     close(f2)
105
106     region_mask_continue = upper(input("Mask more regions? (Y/N): ", "s"));

```

```

107 end
108
109 top_surface = zeros(size(centerline_x));
110 bot_surface = zeros(size(centerline_x));
111 top_distance = zeros(size(centerline_x));
112 bot_distance = zeros(size(centerline_x));
113
114 for i = 1:length(centerline_x)
115     x_pos = centerline_x(i);
116     y_pos = centerline_y(i);
117
118     edge_points = find(edgeImage(:, i));
119     upper_values = find(edge_points > y_pos);
120     lower_values = find(edge_points < y_pos);
121     try
122         bot_surface(i) = edge_points(upper_values(1));
123     catch
124         bot_surface(i) = 0;
125     end
126     try
127         top_surface(i) = edge_points(lower_values(end));
128     catch
129         top_surface(i) = 0;
130     end
131
132     top_distance(i) = abs(top_surface(i) - y_pos) * cal_factor; % Distance in
        m
133     bot_distance(i) = abs(bot_surface(i) - y_pos) * cal_factor; % Distance in
        m
134 end
135

```

```

136 threshold = 1.2 * h_fl/2;
137 top_distance(top_distance > threshold) = NaN;
138 bot_distance(bot_distance > threshold) = NaN;
139
140 x_distance = centerline_x.*cal_factor;
141
142 %% Regression
143 [x_original, y_original] = generate_grain_geometry(L_fl, L_const, h_fl,
144     h_const, a_conv, ...
145     a_div, centerline_x, cal_factor);
146
147 RegressTop = top_distance - y_original; % Total perpendicular regression at
148     each x location top m
149 RegressBot = bot_distance - y_original; % Total perpendicular regression at
150     each x location bottom m
151
152 AveRegressTop = RegressTop/Time; % Average perpendicular regression rate at
153     each x location top m/s
154 AveRegressBot = RegressBot/Time; % Average perpendicular regression rate at
155     each x location bottom m/s
156
157 %% Plotting
158
159 % Plotting regressed surfaces in mm
160
161 f3 = figure();
162 GG(1) = subplot(2,1,1, 'align');
163 AA(1) = plot(x_original* 1000, y_original* 1000, "— Black");
164 hold on
165 AA(2) = plot(x_original* 1000, -y_original* 1000, "— Black");
166 hold on

```

```

162 AA(3) = plot((x_distance - x_distance(1))* 1000, top_distance* 1000, "Black");
163 hold on
164 AA(4) = plot((x_distance - x_distance(1))* 1000, -bot_distance* 1000, "Black")
    ;
165
166 axis equal
167 title(test_name)
168 ylim([-60 60])
169 xlim([-10 290])
170 set(gca, 'FontSize', 18, 'FontName', 'Times New Roman')
171 legend('Pre-Fire', '', 'Post-Fire', '')
172 xlabel('Axial combustor location, mm')
173 ylabel('Distance perpindicular to flow, mm')
174
175 GG(2) = subplot(2,1,2, 'align');
176 AA(7) = plot((x_original-x_distance(1))* 1000, AveRegressBot* 1000, "Blue");
177 hold on
178 AA(8) = plot((x_original-x_distance(1))* 1000, AveRegressTop* 1000, "Red");
179 title(test_name + ' Regression Rate')
180 ylim([0 5])
181 xlim([-10 290])
182 set(gca, 'FontSize', 18, 'FontName', 'Times New Roman')
183 legend('Bottom', 'Top')
184 xlabel('Axial combustor location, mm')
185 ylabel('Average Regression Rate, mm/s')
186
187 function [x_fuel, y_fuel] = generate_grain_geometery(L_fl, L_cyl, h_fl, h_cyl,
    a_conv, a_div, x, factor)
188     y_fuel = zeros(size(x));
189
190     x_conv = L_fl + (h_fl/2 - h_cyl/2)/tan(a_conv);

```

B.1.2 Constant Area Section Edge Detection

```
1 clc , clear  
2 close all  
3 clear all  
  
4  
5 %%%%%%%%%%%%%%%%%%%%%%%%%%%%%%%%%%%%%%%%%%%%%%%%%%%%%%%%%%%%%%%%%%%%%%%%%  
6 %% Edit this section  
7 Fuel_Grain = 11;      % Fuel Grain Number  
8 Temp = 650;           % Tested heater temperature  
9 %%%%%%%%%%%%%%%%%%%%%%%%%%%%%%%%%%%%%%%%%%%%%%%%%%%%%%%%%%%%%%%%%%%%%%%%%  
10  
11 %% Do not edit below this
```

```

12 % Pull data from spreadsheet based on input
13 total = 16; % Total number of tested fuel grains
14 opts.DataRange = '2:15'; opts.SelectedVariableRange = 2:10;
15 IgnitionData = readmatrix("Test_Summary.xlsx"); % Pulls data from spreadsheet
16 for j = 1:total % Loop to pull desire test based on inputs
17     if IgnitionData(j,2) == Fuel_Grain
18         if IgnitionData(j,7) == Temp
19             Row = j;
20             break
21         else
22             end
23     elseif j == total
24         disp('INPUT ERROR')
25     else
26         end
27 end
28
29 % Assign values from spreadsheet to Matlab Variables
30 Day = IgnitionData(Row, 4); Month = IgnitionData(Row, 3);
31 Year = IgnitionData(Row, 5); Testnum = IgnitionData(Row, 6);
32 Mass_i = IgnitionData(Row, 8); Mass_f = IgnitionData(Row, 9);
33 Time = IgnitionData(Row, 10);
34 % Defines the file to pull based on spreadsheet information
35 Folder = "Cut_Photos\";
36 test_name = sprintf("FG%d, %02d/%02d/%d, Test %d, T = %dC", Fuel_Grain, Month
    , Day, Year, Testnum, Temp);
37 file = sprintf("%s%02d_%02d_%d_Test_%d_Throat.tif", Folder, Month, Day, Year,
    Testnum);
38
39 cal_factor = 2.7523e-4; % Preset calibration value, m/px
40

```

```

41 threshold = 0.35; % Edge detect threshold value
42
43 % Original Grain dimensions, based on spreadsheet
44 AAA = FG(Fuel_Grain);
45 h_fl = AAA(1)/1000; h_const = AAA(2)/1000;
46 L_fl = AAA(3)/1000; L_const = AAA(4)/1000;
47
48 L_t = 0.2667; % Overall grain length, m
49
50 a_conv = 45 * (pi/180); % Converging section angle, rad
51 a_div = 3 * (pi/180); % Diverging section angle, rad
52
53 %%%%%%%%%%%%%%%%%%%%%%%%%%%%%%%%%%%%%%%%%%%%%%%%%%%%%%%%%%%%%%%%%%%%%%%%%
54 %% Calibration factor
55 cal_distance = 0.15; % Distance between points selected in calibration image,
    m
56 f1 = figure('Name', 'Select calibration distance 15 cm');
57 imshow(imread(file))
58 [x_cal, y_cal] = ginput(2);
59
60 cal_factor = cal_distance / (x_cal(2) - x_cal(1));
61
62 %%%%%%%%%%%%%%%%%%%%%%%%%%%%%%%%%%%%%%%%%%%%%%%%%%%%%%%%%%%%%%%%%%%%%%%%%
63
64 %% Main script
65 fullImage = imread(file);
66 f1 = figure('Name', 'Crop image to fuel grain, include outer surface');
67 croppedImage = imcrop(fullImage);
68 close(f1)
69
70 f1 = figure();

```

```

71 imshow(croppedImage)
72 set(f1, 'Name', ...
73     'Select four points to define grain centerline – clockwise from upper left
74     ')
75
76 [x_cen, y_cen] = ginput(4);
77
78
79 left_mid = [(x_cen(3) + x_cen(4))/2, (y_cen(3) + y_cen(4))/2];
80 right_mid = [(x_cen(1) + x_cen(2))/2, (y_cen(1) + y_cen(2))/2];
81
82 centerline_slope = (floor(right_mid(2)) - ...
83     floor(left_mid(2)))/(floor(right_mid(1)) - left_mid(1));
84
85 centerline_x = floor(left_mid(1)):1:floor(right_mid(1));
86 centerline_y = centerline_slope.*centerline_x + left_mid(2);
87
88 hold on
89 plot(centerline_x, centerline_y, 'r')
90
91
92 edgeImage = edge(rgb2gray(croppedImage), 'Canny', threshold');
93 [edgeM, edgeN] = size(edgeImage);
94
95 region_mask_continue = "Y";
96
97 while region_mask_continue == "Y"
98     f2 = figure('Name', ...
99         'Mask false edges inside fuel grain. Double click inside closed
100         polygon to proceed. ');
101     mask = roipoly(edgeImage);
102     edgeImage = edgeImage.*~mask;
103     close(f2)
104
105

```



```

100     region_mask_continue = upper(input("Mask more regions? (Y/N): ", "s"));
101 end
102
103 top_surface = zeros(size(centerline_x));
104 bot_surface = zeros(size(centerline_x));
105 top_distance = zeros(size(centerline_x));
106 bot_distance = zeros(size(centerline_x));
107
108 for i = 1:length(centerline_x)
109     x_pos = centerline_x(i);
110     y_pos = centerline_y(i);
111
112     edge_points = find(edgeImage(:, i));
113     upper_values = find(edge_points > y_pos);
114     lower_values = find(edge_points < y_pos);
115     try
116         bot_surface(i) = edge_points(upper_values(1));
117     catch
118         bot_surface(i) = 0;
119     end
120     try
121         top_surface(i) = edge_points(lower_values(end));
122     catch
123         top_surface(i) = 0;
124     end
125
126     top_distance(i) = abs(top_surface(i) - y_pos) * cal_factor; % Distance in
        m
127     bot_distance(i) = abs(bot_surface(i) - y_pos) * cal_factor; % Distance in
        m
128 end

```

```

129
130 threshold = 1.2 * h_fl/2;
131 top_distance(top_distance > threshold) = NaN;
132 bot_distance(bot_distance > threshold) = NaN;
133 %%
134 x_distance = centerline_x.*cal_factor;
135 y_distance = centerline_y.*cal_factor;
136 %% Regression
137 % [x_original, y_original] = generate_grain_geometry(L_fl, L_cyl, h_fl, h_cyl
    , a_conv, ...
138 %     a_div, centerline_x, cal_factor);
139 %
140 % RegressTop = top_distance - y_original; % Total perpindicular regression at
    each x location top m
141 % RegressBot = bot_distance - y_original; % Total perpindicular regression at
    each x location bottom m
142 %
143 % AveRegressTop = RegressTop/Time; % Average perpindicular regression rate at
    each x location top m/s
144 % AveRegressBot = RegressBot/Time; % Average perpindicular regression rate at
    each x location bottom m/s
145
146 %% Plotting
147 % Plotting Original Surface
148 figure()
149 Original = [-25.4/2, -h_const*500; 25.4/2, -h_const*500; 25.4/2, h_const*500;
    -25.4/2, h_const*500; -25.4/2, -h_const*500];
150 plot(Original(:,1), Original(:,2), '— black')
151 hold on
152
153 % Plotting regressed surfaces in mm

```

```
154
155 counter = 0;
156 [row, col] = size(edgeImage);
157 for k = 1:row
158     for t = 1:col
159         if edgeImage(k,t) == 1
160             counter = counter + 1;
161             regressionplot(counter, 1) = k;
162             regressionplot(counter, 2) = t;
163         else
164             end
165     end
166 end
167 regressionplot = regressionplot*cal_factor*1000;
168 ytop = max(regressionplot(:,2));
169 ybot = min(regressionplot(:,2));
170 ymid = mean([ytop, ybot]);
171 xtop = max(regressionplot(:,1));
172 xbot = min(regressionplot(:,1));
173 xmid = mean([xbot, xtop]);
174
175 regressionplot(:,1) = regressionplot(:,1)-xmid;
176 regressionplot(:,2) = regressionplot(:,2)-ymid;
177
178 scatter(regressionplot(:,1), regressionplot(:,2), '. black')
179 % GG(1) = subplot(2,1,1, 'align');
180 % AA(1) = plot(x_original* 1000, y_original* 1000, "— Black");
181 % hold on
182 % AA(2) = plot(x_original* 1000, -y_original* 1000, "— Black");
183 % hold on
```

```

184 % AA(3) = plot((x_distance - x_distance(1))* 1000, top_distance* 1000, "Black
      ");
185 % hold on
186 % AA(4) = plot((x_distance - x_distance(1))* 1000, -bot_distance* 1000, "Black
      ");

187
188 counter = 0;
189 for k = 1:length(regressionplot)
190     if regressionplot(k,2) < (h_const*1000)/2 && regressionplot(k,2) > -(
        h_const*1000)/2
191         counter = counter + 1;
192         if regressionplot(k,1)>0
193             regressionwall(counter, 1) = regressionplot(k,1) -25.4/2;
194             regressionwall(counter, 2) = regressionplot(k,2);
195         else
196             regressionwall(counter, 1) = -regressionplot(k,1) -25.4/2;
197             regressionwall(counter, 2) = regressionplot(k,2);
198         end
199     else
200
201     end
202 end
203 counter = 0;
204
205 for k = 1:length(regressionplot)
206     if regressionplot(k,1) < 25.4/2 && regressionplot(k,1) > -25.4/2
207         counter = counter + 1;
208         if regressionplot(k,2)>0
209             regressiontop(counter, 1) = regressionplot(k,2)-(h_const*1000)/2;
210             regressiontop(counter, 2) = regressionplot(k,1);
211         else

```

```

212         regressiontop(counter, 1) = -regressionplot(k,2)-(h_const*1000)/2;
213         regressiontop(counter, 2) = regressionplot(k,1);
214     end
215 else
216
217     end
218 end
219
220 regressionwall(:,1) = regressionwall(:,1)./Time;
221 regressiontop(:,1) = regressiontop(:,1)./Time;
222 % figure()
223 % plot(regressionwall(:,2), regressionwall(:,1), '.black')
224 % ylim([0 0.5])
225 avgregwall = mean(regressionwall(:,1));
226 avgtop = mean(regressiontop(:,1));
227 avgconsarea = mean([regressionwall(:,1);regressiontop(:,1)]);
228 txt=sprintf('Avg Wall Regression = %f mm/s\n', avgregwall);
229 txt2 = sprintf('Avg Top/Bottom Regression = %f mm/s\n', avgtop);
230 txt3 = sprintf('Avg Const Area Regression = %f mm/s', avgconsarea);
231 AllText = [txt, txt2, txt3];
232 text(-25, -15, AllText, 'FontSize',18, 'FontName','Times New Roman')
233 axis equal
234 title(test_name)
235 ylim([-20 20])
236 xlim([-30 30])
237 set(gca, 'FontSize',18, 'FontName', 'Times New Roman')
238 Type{1} = plot(nan,nan, 'black —');
239 Type{2} = scatter(nan,nan, 'black .');
240 legend([Type{1:2}], {'Pre-Fire','Post-Fire'}, 'location','nw', 'box','off')
241
242 xlabel('Width, mm')

```

```

243 ylabel('Height , mm')
244 % GG(2) = subplot(2,1,2, 'align ');
245 % AA(7) = plot((x_original-x_distance(1))* 1000, AveRegressBot* 1000, "Blue");
246 % hold on
247 % AA(8) = plot((x_original-x_distance(1))* 1000, AveRegressTop* 1000, "Red");
248 % title(test_name + ' Regression Rate')
249 % ylim([0 5])
250 % xlim([-10 290])
251 % set(gca,'FontSize',18, 'FontName', 'Times New Roman')
252 % legend('Bottom','Top')
253 % xlabel('Axial combustor location , mm')
254 % ylabel('Average Regression Rate, mm/s')
255
256 function [x_fuel, y_fuel] = generate_grain_geometry(L_fl, L_cyl, h_fl, h_cyl,
    a_conv, a_div, x, factor)
257 y_fuel = zeros(size(x));
258
259 x_conv = L_fl + (h_fl/2 - h_cyl/2)/tan(a_conv);
260
261 for i = 1:length(x)
262     x_pos = x(i)*factor;
263     x_fuel(i) = x_pos;
264
265     if x_pos < L_fl
266         y_fuel(i) = h_fl / 2;
267     elseif x_pos >= L_fl && x_pos < x_conv
268         y_fuel(i) = ((x_pos - L_fl) * -tan(a_conv)) + h_fl/2;
269     elseif x_pos >= x_conv && x_pos < x_conv + L_cyl
270         y_fuel(i) = h_cyl / 2;
271     else
272         y_fuel(i) = ((x_pos - (x_conv + L_cyl))*tan(a_div)) + h_cyl/2;

```

```

273     end
274 end
275 end

```

B.2 Regression Rate Code for Optically Accessible SFSJ

```

1  %% Manual Regression OSFSJ fuel grains
2  %% Ethan J. Schlussel
3
4  % To use, have a video trimmed to be short (~0.5 seconds before/after
5  % ignition)
6
7  clc , clear
8  clear all
9  close all
10
11 [FileName,PathName] = uigetfile('C:\Users\ejsch\OneDrive\Graduate School\
    Masters Thesis\SFSJ\', ...
12 'Locate the video file. ');
13 file = strcat(PathName,FileName);
14
15 %%%%%%%%%%%%%%%%%%%%%%%%%%%%%%%%%%%%%%%%%%%%%%%%%%%%%%%%%%%%%%%%%%%%%%%%%%
16 %% Insert test information here
17 FuelGrainName = '14f';
18 day = 22;
19 month = 9;
20 year = 23;
21 test = 4;
22

```

```

23 firstframelight = 13; % Use imshow(vid('frame', file)), enter first frame
    with light here
24 regressionlocation = 80; % Distance from front of fuel grain enter here
25
26 % If you know the calibration info for that video, insert it here
27 % cal_factor = ;
28 % centerline_x = ;
29 % centerline_y = ;
30
31 % If you need to find the calibration info, use this function
32 [cal_factor, centerline_x, centerline_y] = calibrate(file);
33
34 %%%%%%%%%%%%%%%%%%%%%%%%%%%%%%%%%%%%%%%%%%%%%%%%%%%%%%%%%%%%%%%%%%%%%%%%%%
35 %% Setting zoom position
36 firstframe033 = firstframelight + 10; % First image shown for regression is
    1/3s after ignition
37 date = [num2str(month, '%02.f'), '_', num2str(day, '%02.f'), '_', num2str(year
    )];
38
39 % Zoom Position
40 regressionlocation = regressionlocation - 22.23;
41 f6 = figure('Name', 'Select zoom position of bottom');
42 imshow(vid(90, file));
43 hold on
44 plot(centerline_x, centerline_y, "r")
45 hold on
46 xline(regressionlocation/cal_factor/1000+centerline_x(1), "r")
47
48 f6.WindowState = 'maximized';
49 [TopZoomx, TopZoomy] = ginput(1);
50

```



```

51 base = (TopZoomy - centerline_y(1))*cal_factor*1000;
52 close all
53 %% Get Regression
54 counter = 0;
55 jump = 10;
56 for frame = firstframe033:jump:firstframe033+70
57     f2 = figure('Name', 'Select regression location top, then bottom. Right
        click to skip images before/after ignition');
58     imshow(vid(frame, file));
59     f2.WindowState = 'maximized';
60     hold on
61     plot(centerline_x, centerline_y, "r")
62     hold on
63     xline(regressionlocation/cal_factor/1000+centerline_x(1), "r")
64     if counter > 0
65         plot(topx(counter), topy(counter), 'r_')
66         plot(botx(counter), boty(counter), 'r_')
67     else
68     end
69     counter = counter + 1;
70
71     xlim([regressionlocation/cal_factor/1000+centerline_x(1) - 100,
        regressionlocation/cal_factor/1000+centerline_x(1) + 100])
72     ylim([centerline_y(1) - base/cal_factor/1000 - 0.015/cal_factor,
        centerline_y(1) - base/cal_factor/1000 + 0.015/cal_factor])
73
74     [topx(counter), topy(counter)] = ginput(1);
75
76     xlim([regressionlocation/cal_factor/1000+centerline_x(1) - 100,
        regressionlocation/cal_factor/1000+centerline_x(1) + 100])

```

```

77     ylim([centerline_y(1) + base/cal_factor/1000 - 0.015/cal_factor ,
           centerline_y(1) + base/cal_factor/1000 + 0.015/cal_factor])
78     [botx(counter), boty(counter)] = ginput(1);
79     sel = get(f2, 'SelectionType');
80     if strcmpi(sel, 'alt'); counter = counter - 1; end
81     close all
82 end
83
84 % Plotting Regression
85 figure(3)
86
87 regressedtop = (centerline_y(floor(regressionlocation))-topy)*cal_factor*1000;
88 regressedbot = (boty - centerline_y(floor(regressionlocation)))*cal_factor
           *1000;
89
90 Regtodeletet = regressedtop < base-7 | regressedtop > base+7;
91 regressedtop(Regtodeletet) = [];
92 Regtodeleteb = regressedbot < base-7 | regressedbot > base+7;
93 regressedbot(Regtodeleteb) = [];
94 clear("Time")
95 Time(1) = 1/3;
96 for q = 2:length(regressedtop)
97     Time(q) = Time(q-1)+1/3;
98 end
99
100 scatter(Time(1:end), regressedtop(1:length(Time)), 'ko')
101 hold on
102 scatter(Time(1:end), regressedbot(1:length(Time)), 'ks')
103 Name = [ 'FG', num2str(FuelGrainName), ' - ', num2str(month, '%02.f'), '/',
          num2str(day), '/', num2str(year), ', x = ', num2str(regressionlocation
          +22.23), 'mm' ];

```

```

104 title(Name);
105 xlabel('Time, s')
106 ylabel('Distance from Center Line, mm')
107 ptop = polyfit(Time(2:length(Time)-1), regressedtop(2:length(Time)-1), 1);
108 regressiontop = polyval(ptop,Time);
109 pbot = polyfit(Time(2:length(Time)-1), regressedbot(2:length(Time)-1), 1);
110 regressionbot = polyval(pbot,Time);
111 plot(Time, regressiontop, 'k-', 'LineWidth', 1)
112 plot(Time, regressionbot, 'k—', 'LineWidth', 1)
113 legend('Top Regression', 'Bottom Regression', 'Top Best Fit', 'Bottom Best Fit'
        , 'Location', 'northwest')
114 legend boxoff
115 pbaspect([1 1 1])
116 text(2, base, "$\dot{r}_{\text{top}} = $" + num2str(ptop(1)) + "$\frac{\text{mm}}{\text{s}}$", '
        Interpreter', 'latex', 'FontSize', 18, 'FontName', 'Times New Roman')
117 text(2, base+.25, "$\dot{r}_{\text{bot}} = $" + num2str(pbot(1)) + "$\frac{\text{mm}}{\text{s}}$", '
        Interpreter', 'latex', 'FontSize', 18, 'FontName', 'Times New Roman')
118 set(gca, 'FontSize', 18, 'FontName', 'Times New Roman')
119 xlim([0 4])
120
121 Top = regressedtop '
122 Bottom = regressedbot '
123
124 function video = vid(frame, file)
125
126 obj = VideoReader(file);
127 vid = read(obj);
128 for x = frame
129     video = (vid(:, :, :, x));
130 end
131

```

```

132 end
133
134 function [cal_factor, centerline_x, centerline_y] = calibrate(file)
135 % Calibration factor determination
136 cal_distance = 0.22225; % Distance between points selected in calibration
    image, m
137 f1 = figure('Name', 'Select calibration distance 22.225 cm (length of window
    holder opening)');
138 imshow(vid(90, file)*3)
139 f1.WindowState = 'maximized';
140 [x_cal, y_cal] = ginput(2);
141 cal_factor = cal_distance / (x_cal(2) - x_cal(1));
142 close all
143
144 % Main script
145 f4 = figure(1);
146 croppedImage = imshow(vid(90, file)*3);
147
148 set(f4, 'Name', ...
149     'Select four points to define centerline - clockwise from upper right')
150 f4.WindowState = 'maximized';
151 [x_cen, y_cen] = ginput(4);
152
153 left_mid = [(x_cen(3) + x_cen(4))/2, (y_cen(3) + y_cen(4))/2];
154 right_mid = [(x_cen(1) + x_cen(2))/2, (y_cen(1) + y_cen(2))/2];
155
156 centerline_slope = (floor(right_mid(2)) - ...
157     floor(left_mid(2)))/(floor(right_mid(1)) - left_mid(1));
158
159 centerline_x = floor(left_mid(1)):1:floor(right_mid(1));
160 centerline_y = centerline_slope.*centerline_x + left_mid(2);

```

```
161 close all
162 end
```